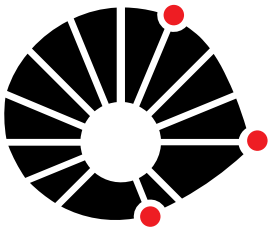

UNIVERSIDADE ESTADUAL DE CAMPINAS
Instituto de Física Gleb Wataghin

MARCOS VINICIUS DOS SANTOS

Effects of Quantum Decoherence in Supernova Neutrinos

Efeitos de Descoerência Quântica em Neutrinos de Supernovas

Campinas
2023

Marcos Vinicius dos Santos

Effects of Quantum Decoherence in Supernova Neutrinos

Efeitos de Descoerência Quântica em Neutrinos de Supernovas

Thesis presented to the Institute of Physics Gleb Wataghin of the University of Campinas in partial fulfillment of the requirements for the degree of Doctor in Sciences, in the area of Physics.

Tese apresentada ao Instituto de Física Gleb Wataghin da Universidade Estadual de Campinas como parte dos requisitos exigidos para a obtenção do título de Doutor em Ciências, na área de Física.

Supervisor: Pedro Cunha de Holanda

Este trabalho corresponde à versão final da Tese defendida pelo aluno Marcos Vinicius dos Santos e orientada pelo Prof. Dr. Pedro Cunha de Holanda.

Campinas

2023

Ficha catalográfica
Universidade Estadual de Campinas
Biblioteca do Instituto de Física Gleb Wataghin
Lucimeire de Oliveira Silva da Rocha - CRB 8/9174

Santos, Marcos Vinicius dos, 1990-
Sa59e Effects of quantum decoherence in supernova neutrinos / Marcos Vinicius dos Santos. – Campinas, SP : [s.n.], 2023.

Orientador: Pedro Cunha de Holanda.
Tese (doutorado) – Universidade Estadual de Campinas, Instituto de Física Gleb Wataghin.

1. Neutrinos. 2. Decoerência quântica. 3. Supernova (Estrela). I. Holanda, Pedro Cunha de, 1973-. II. Universidade Estadual de Campinas. Instituto de Física Gleb Wataghin. III. Título.

Informações Complementares

Título em outro idioma: Efeitos de descoerência quântica em neutrinos de supernovas
Palavras-chave em inglês:
Neutrinos
Quantum decoherence
Supernovae
Área de concentração: Física
Titulação: Doutor em Ciências
Banca examinadora:
Pedro Cunha de Holanda [Orientador]
Carola Dobrigkeit Chinellato
Fernando Gonçalves Gardim
Marcos César de Oliveira
Célio Adrega de Moura Junior
Data de defesa: 05-10-2023
Programa de Pós-Graduação: Física

Identificação e informações acadêmicas do(a) aluno(a)
- ORCID do autor: https://orcid.org/0000-0001-5247-744X
- Currículo Lattes do autor: http://lattes.cnpq.br/5161660188380421

MEMBROS DA COMISSÃO EXAMINADORA DA TESE DE DOUTORADO DO ALUNO MARCOS VINICIUS DOS SANTOS - RA 262758, APRESENTADA E APROVADA AO INSTITUTO DE FÍSICA GLEB WATAGHIN, DA UNIVERSIDADE ESTADUAL DE CAMPINAS, EM 05/10/2023.

COMISSÃO JULGADORA:

- Prof. Dr. Pedro Cunha de Holanda – Presidente e Orientador (IFGW/UNICAMP)

- Profa. Dra. Carola Dobrigkeit Chinellato (IFGW/UNICAMP)

- Prof. Dr. Fernando Gonçalves Gardim (Universidade Federal de Alfenas)

- Prof. Dr. Marcos Cesar de Oliveira (IFGW/UNICAMP)

- Prof. Dr. Célio Adrega de Moura Júnior (Universidade Federal do ABC, Centro de Ciências Naturais e Humanas)

OBS.: Ata da defesa com as respectivas assinaturas dos membros encontra-se no SIGA/Sistema de Fluxo de Dissertação/Tese e na Secretaria do Programa da Unidade.

CAMPINAS

2023

Este trabalho é dedicado em memória
do meu amigo Maxwell Marcos Pedro.

Acknowledgements

The accomplishment of this work is due in part, both in terms of academic contribution and personal evolution, direct or indirect to the friendship and efforts of several people during my doctoral period at Unicamp. Therefore, I dedicate these words to express a humble thank you to some of them.

I would like to express my gratitude first and foremost to my wife, Lais, for her unwavering support and extreme friendship. I also want to thank my parents, Rozili and Vicente, and my brother, Julio, who, in addition to being family, are my great friends.

I extend my thanks to my advisor, Pedro Holanda, who believed in this thesis work more than anyone else, boosting my confidence in this and future endeavors. I also appreciate the enjoyable and insightful working companionship over these past years.

Undoubtedly, I must thank Pedro Dedin (notice the number of Pedros in my acknowledgments), who was a very pleasant, precise, friendly, and calm working companion throughout my entire doctoral period, becoming a great friend, hopefully for life. I also extend my gratitude to his advisor, Professor Ernesto Kemp, for the camaraderie in work and the friendship that extended beyond borders.

I dedicate my sincere thanks to Professor Orlando Peres for making my stay at Unicamp as enriching as possible. Furthermore, I thank the Unicamp neutrino group, Gefan, and its members for making my doctoral work more achievable due to the intense interaction and exchange of experiences among the group's members.

My fellow graduate students, with whom I have cultivated an extremely deep and hopefully lasting friendship, and who I hold dear, are self-named as Copenhagers (although I suspect they should call themselves Many Worlders due to their interpretative preferences in quantum mechanics): Bianca, Bruno, Cleiton, João, Jonathan (and his family), Léo Leite, Leonardo, and Pedro Dedin again. From the supernova neutrino group, I thank Pedro Cintra for the enjoyable company in recent years. I also thank my former students in PED, Gabriel, and Ítalo, for their friendship. I extend my gratitude to the other graduate colleagues I haven't mentioned, with whom we've shared good times.

I would also like to express my appreciation to the couple Max and Cláudia for their friendship, support, and care over these past years. I extend my thanks to my family and friends whom I haven't mentioned here but who played an indispensable role in my journey.

This study was financed by the Coordenação de Aperfeiçoamento de Pessoal de Nível Superior – Brasil (CAPES) – Finance Code 001, as well as by CAPES proc. 88887.372426/2019-00.

"[...]when you have eliminated the impossible,
whatever remains, however improbable,
must be the truth[...]"
(Sherlock Holmes, The Sign of the Four, 1890)

Resumo

Nesta tese, discutimos aspectos mistura de neutrinos em supernovas passadas e futuras. Mostramos nossa análise de dados sobre a emissão e mistura de neutrinos da supernova SN1987A, rejeitando com limites superiores a 2σ a solução de hierarquia invertida de massas para conversão de sabor. Também fornecemos uma extensa descrição dos efeitos de descoerência quântica gerada por gravidade quântica ou outra física exótica equivalente em supernovas para diferentes modelos. Além disso, examinamos a possível dependência da energia pelos parâmetros de descoerência quântica ($\Gamma = \Gamma_0(E/E_0)^n$) com diferentes leis de potência ($n = 0, 2, 5/2$). Nossos resultados indicam que os detectores de geração futura (DUNE, Hyper-K e JUNO) podem restringir significativamente os parâmetros de descoerência quântica em diferentes cenários. Para uma supernova localizada a 10 kpc da Terra, DUNE poderia potencialmente estabelecer limites de 3σ para $\Gamma \leqslant 6,2 \times 10^{-14}$ eV no cenário de hierarquia de massa normal, enquanto Hyper-K poderia impor um limite de 2σ em $\Gamma \leqslant 3,6 \times 10^{-14}$ eV para a hierarquia de massa invertida com $n = 0$ — supondo que não haja troca de energia entre o subsistema de neutrinos e ambiente não padrão. Esses limites se tornam ainda mais restritivos para uma supernova mais próxima da Terra. Quando relaxamos a restrição de troca de energia, para uma supernova a 10 kpc, DUNE pode estabelecer um limite de 3σ de $\Gamma_8 \leqslant 4,2 \times 10^{-28}$ eV para hierarquia normal, enquanto Hyper-K poderia restringir $\Gamma_8 \leqslant 1,3 \times 10^{-27}$ eV para hierarquia invertida ($n = 0$) com 2σ, representando os limites mais restritivos reportados até o momento. Além disso, examinamos o impacto da perda de neutrinos durante a propagação em uma futura detecção de supernovas por efeitos de descoerência quântica, também estabelecendo limites estatísticos para esse fenômeno.

Palavras-chave: Neutrinos. Descoerência quântica. Supernovas.

Abstract

In this thesis, we discuss aspects of past and future supernova-neutrino mixing. We show our data analysis concerning SN1987A emission and mixing, rejecting with more than 2σ bounds on inverted hierarchy solution for flavor conversion. We also provided an extensive framework to understand quantum decoherence effects in supernovas engendered by quantum gravity or other equivalent exotic physics for different models. Additionally, we examine the potential energy dependence of quantum decoherence parameters ($\Gamma = \Gamma_0(E/E_0)^n$) with different power laws ($n = 0, 2, 5/2$). Our findings indicate that future-generation detectors (DUNE, Hyper-K, and JUNO) can significantly constrain quantum decoherence parameters under different scenarios. For a Supernova located 10 kpc away from Earth, DUNE could potentially establish 3σ bounds of $\Gamma \leqslant 6.2 \times 10^{-14}$ eV in the normal mass hierarchy scenario, while Hyper-K could impose a 2σ limit of $\Gamma \leqslant 3.6 \times 10^{-14}$ eV for the inverted mass hierarchy with $n = 0$ — assuming no energy exchange between the neutrino subsystem and non-standard environment. These limits become even more restrictive for a closer Supernova. When we relax the assumption of energy exchange, for a 10 kpc supernova, DUNE can establish a 3σ limit of $\Gamma_8 \leqslant 4.2 \times 10^{-28}$ eV for normal hierarchy, while Hyper-K could constrain $\Gamma_8 \leqslant 1.3 \times 10^{-27}$ eV for inverted hierarchy ($n = 0$) with 2σ, representing the most stringent bounds reported to date. Furthermore, we examine the impact of neutrino loss during propagation for future Supernova detection, also establishing statistical limits to this phenomenon.

Keywords: Neutrinos. Quantum decoherence. Supernovas.

List of Figures

List of Tables

Table of Contents

Introduction

In the last decades, the neutrino sector has revealed interesting and intriguing aspects of our growing knowledge of particle physics. Particularly, in flavor physics, the neutrino mixing models provide a framework where the flavor states do not have well-defined mass, as well as energy states do not interact through Standard Model, allowing our measurement of quantum effects in macroscopic scales, a discovery awarded with Nobel prize. Despite advances in neutrino physics and many years of an active community, some central questions are still to be answered, such as the origin of neutrino mass, CP violation in neutrinos, and details of neutrino mixing models, relevant to characterizing any neutrino flux across all sources.

Amongst the possible neutrino sources, with some of them briefly mentioned in Chapter 1, in this thesis, we devote our attention to supernovas. In this extreme event in astrophysics, neutrinos play a relevant role, carrying almost all gravitational binding energy of the dying star as well as changing the dynamics and thermodynamics of the explosion. This challenging neutrino environment is under intense research, and it is unique for a number of reasons. The most prominent is the only place in the current Universe with the existence of a dense neutrino gas, generating non-linear unsolved neutrino mixing effects nowadays. If this event occurs in our galaxy, the neutrino flux crossing Earth can be orders of magnitude higher than the solar neutrino flux. Finally, although we were able to measure extra-terrestrial neutrinos in the past, we have never detected such a well-characterized source, with high flux, and a large baseline as a galactic supernova. The baseline of thousands of light-years shows to be a notable feature to be explored and used in the investigation of many works such as neutrino decays [2], making supernovas natural laboratories of particle physics. In this thesis, it is not the single characteristic of a future galactic supernova detection we are interested in, but the distance from Earth makes our analysis unique. The specific phenomenon we prospect here is the spontaneous transition of pure neutrino states to mixed ones or quantum decoherence. This effect is expected in different candidate theories of quantum gravity by the so-called quantum foam [3, 4]. Although we inspire part of our analysis in works where quantum gravity is an extensive subject, we remain agnostic, limiting ourselves to phenomenologically modeling the neutrino propagation through open quantum systems formalism, which provides a

robust framework to understand quantum decoherence effects, and we attempt to bring this discussion to an eventual future supernova neutrino detection.

In spite of the fact that the main goal of this work is to provide a consistent and testable solution to the quantum decoherence problem in a future supernova neutrino detection, the path to cross in order to achieve this goal makes this thesis be divided into two main parts: in the first one, we show a very brief scenario of neutrino physics in Chapter 1. Then, we focus on the basics of neutrino mixing in vacuum and inside matter in Chapters 2 and 3. In Chapter 4, we start our discussion on supernova neutrinos and neutrino mixing in this environment, followed by an introduction to the supernova SN1987A physics and our analysis of this astrophysical event in Chapter 5. Afterward, in part two, we introduce the quantum decoherence formalism in addition to its effects on neutrino propagation in Chapter 6. In Chapter 7 we apply the concepts developed in other chapters to a possible future supernova detection, bounding quantum decoherence not only the first time in this neutrino source but also finding the most stringent statistical limits on quantum decoherence parameters up to date.

Chapter 1

Brief status of neutrino physics

Since its proposal in the 1930s, its discovery in the 1950s, evidence of mixing amongst flavors in the 1990s, and many other questions and answers made in this almost one century of intense research, we should recognize that neutrino physics became fairly huge. In this sense, this chapter has no intention at all to cover the entire neutrino physics, but just gives a very brief historical status of the current scenario in which (part of) this topic of particle physics is placed in the view of the author.

Firstly, it is worth mentioning that neutrinos are fermions with three different flavors: ν_e, ν_μ and ν_τ, partners to their corresponding charged leptons e^-, μ^- and τ^-, interacting, as far as we know, only through gravitational and weak interactions, and then, not electrically or strongly charged, making interaction rates (or cross sections) very low compared to other fundamental particles. We show some details on neutrino interaction with ordinary matter in Chapter 3. They are also incredibly light, compared to other massive particles of the Standard Model. However, probably, the most remarkable feature for the purposes of this thesis is the propagation basis is not the same as the interaction basis, and consequently, flavor state α can be written as a combination of energy states $\nu_\alpha = \sum_i U_{\alpha i}\nu_i$, with amplitudes $U_{\alpha i}$ being elements of the Pontecorvo-Maki-Nakagawa-Sakata (PMNS) matrix [5], parameterized with three mixing angles θ_{12}, θ_{13} and θ_{23} and a charge-parity (CP) phase $\delta_{\rm CP}$. For a more complete description of neutrino properties, we refer to [6]. We start the discussion about neutrino mixing in Chapter 2, and all other chapters, as well as our results, will be focused on this neutrino feature. In the following, we discuss three individual aspects of neutrino physics that are a focus of intense research and are also a starting point to discuss this particle: neutrino mass, neutrino mixing parameters, and some neutrino sources.

Neutrino mass: Currently, there is no concise, complete, and experimentally proven mechanism to explain neutrino mass existence or nature. As nature, we mean that nowadays we do not know if neutrinos are Dirac or Majorana particles. Consequently, the question

Table 1 – Current global fitted parameters [1], used in all calculations in this thesis. The normal neutrino mass hierarchy is considered in the fit of the parameters above.

Parameter	Best Fit (1σ)
$\theta_{12}(^o)$	$33.45^{+0.77}_{-0.75}$
$\theta_{13}(^o)$	$8.62^{+0.12}_{-0.12}$
$\theta_{23}(^o)$	$42.1^{+1.1}_{-0.9}$
$\Delta m^2_{21} \times (10^5\ \text{eV}^{-2})$	$7.42^{+0.21}_{-0.20}$
$\Delta m^2_{31} \times (10^3\ \text{eV}^{-2})$	$2.510^{+0.027}_{-0.027}$

of the neutrino as its antiparticle is still to be answered. Experimental efforts through neutrinoless double-beta decay ($0\nu\beta\beta$), a decay expected only for Majorana neutrinos, and then potentially define neutrino nature, are ongoing (see a review in [7]). From a theoretical point of view, suggestions for the neutrino-mass mechanism through the so-called seesaw models is a very active research subject and basically states that the most general Lagrangian for neutrino masses would allow the existence of a large Majorana mass compared to an also present Dirac mass term, making this unbalance in the diagonalized neutrino mass matrix provide a very tiny effective mass. A review of the topic can be seen in [8]. In the context of experimental ν-mass limits, the most promising limits are from tritium β-decay experiments, with the best limits coming from the KATRIN experiment, with $m_\nu < 0.9$ eV with 90% C.L [9]. Limits from cosmology are more stringent, however, extremely model-dependent.

Neutrino mixing parameters: It is clear that a precision era of neutrino mixing has arrived with recently decommissioned, in current operation, and future-generation detectors, such as KamLAND [10], Daya Bay [11], Super-Kamiokande [12], NOvA [13], T2K [14], Hyper-Kamiokande [15], DUNE [16], JUNO [17], and many others. We were able to measure with good precision the three neutrino mixing angles, as well as the two mass-squared differences Δm^2_{21} and Δm^2_{31} (the details of these quantities and their implications will be clear in Chapter 2), and improvements from future generation experiments, are expected. The same enhancement is valid for the δ_{CP} phase. However, it is a quantity still not precisely measured nowadays, and more data is crucial to determine a non-null CP phase. Table 1 shows the most recent global fitted mixing parameters, being the ones assumed to obtain our results further in this work.

Grand-unified neutrino flux: Neutrino detection from natural and human-made sources across a very large spectrum was a great achievement in the last decades. Neutrinos from our Sun correspond to the most abundant flux that crosses Earth, with an energy scale of few MeV. The solution to the solar neutrino problem was an extensive problem in neutrino physics with the solution provided by the resonant matter effect and we discuss it in Section 3.2 (see also [19] for a recent review). Neutrinos from nuclear reactors also gained importance with precise experiments such as Daya Bay and KamLAND, with the

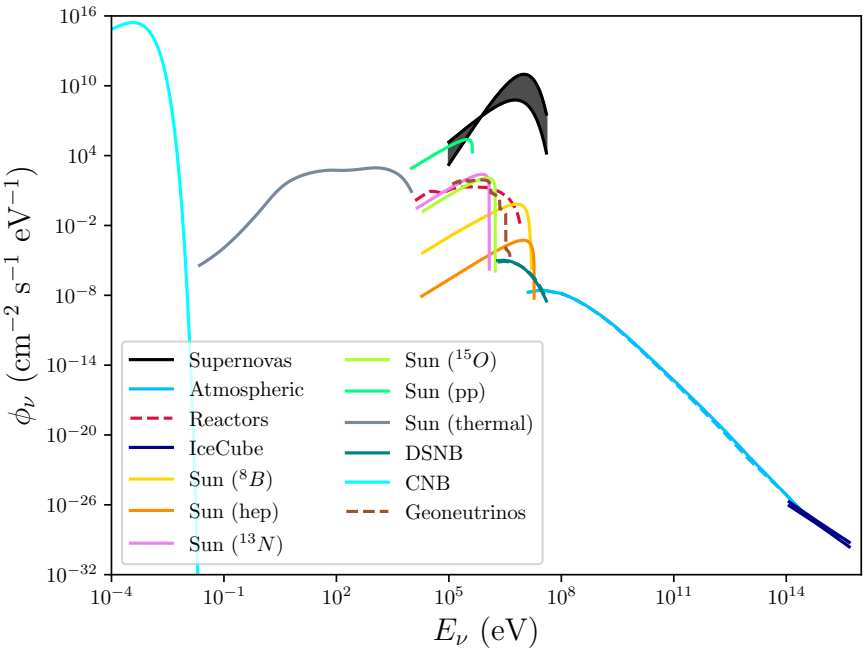

Figure 1 – Neutrino flux from many sources. Dashed lines correspond to antineutrinos and solid ones to neutrinos, with a possible fraction of antineutrinos for Supernovas, atmospheric, the thermal flux of the Sun, DSNB, CNB, and extragalactic neutrinos measured by IceCube. The bands represent the expected range of flux. Data taken from [18].

former also able to detect geoneutrinos or neutrinos coming from inside the Earth's crust and mantle [20, 21]. Cosmic rays interacting with the Earth's atmosphere also produce a non-negligible high energy neutrino flux, being a source of background to dedicated experiments [22]. One promising neutrino source is particle accelerators, with controlled initial flux, where future experiments such as DUNE claim precise measurement of δ_{CP}. Finally, ultra-high energy neutrinos could be detected through the IceCube experiment, with neutrino energies beyond the PeV scales, and more than that, from outside the Milky Way, which opened the extragalactic ultra-high energy neutrino astronomy era. Neutrinos from the Big Bang, which constitute the Cosmic Neutrino Background (CNB), are expected to be abundant, but with the lowest energy known. This is not a single diffuse neutrino flux, since exploding stars from different galaxies provide a Diffuse Supernova Neutrino Background (DSNB), expected to be detected in the near future. Galactic supernovas are also an important neutrino laboratory and will be the focus of this work. Figure 1 shows the neutrino spectrum across these sources. It is possible to see that supernovas have a high flux and accessible detection energy for contemporaneous experiments.

To understand supernova neutrinos in order to explore their particular features aligned with the purposes of this thesis, we need to describe the foundations of neutrino mixing in the next chapters, starting with neutrino mixing in vacuum in the density matrix

formalism in Chapter 2.

Chapter 2

Neutrino mixing in vacuum

The neutrino mixing is already a widely accepted framework to describe how ν mass degeneracy plays a role in neutrino flavor composition from many sources [6]. The idea behind neutrino mixing is that the generation and the propagation basis are fundamentally different: since neutrinos are created in a well-defined flavor basis in order to conserve leptonic numbers in a quantum field theory interaction, it should propagate in a well-defined mass basis, given the form of the equations of motion of quantum mechanics. In the neutrino flavor basis, we define the three known states as ν_e, ν_μ, and ν_τ, while for the charge current interaction, the charged partner lepton is part of the generation process. However, these states are a mixing of a number of mass states, or ν_1, ν_2, and ν_3. To understand the implications of this related basis on neutrino propagation, we devote this chapter to describing the most basic aspects of neutrino mixing. Firstly, we can define a neutrino density matrix as

$$\rho(t) = \sum_j w_j \left|\nu_j(t)\right\rangle\left\langle\nu_j(t)\right| \ , \tag{2.1}$$

where w_j is a statistical weight corresponding to a specific mass state and $|\nu_j(t)\rangle$ respects the Schrödinger equation (in Schrödinger picture). The trace of this operator is one at any time

$$\mathrm{Tr}[\rho(t)] = \sum_i \langle\nu_i|\, \rho(t)\, |\nu_i\rangle = \sum_i \sum_j w_j \langle\nu_j(t)|\nu_i\rangle\langle\nu_i|\nu_j(t)\rangle = 1 \ , \tag{2.2}$$

and also $\rho^2(t)$ has the trace

$$\mathrm{Tr}\big[\rho^2(t)\big] = \sum_j w_j^2 \ , \tag{2.3}$$

which is equal to unity if the neutrino ensemble is pure. Hence, a probability to measure a neutrino with state i after a time t is

$$P_{ij}(t) = \mathrm{Tr}[\rho_i(0)\rho_j(t)] = \langle\nu_i|\,\rho_j(t)\,|\nu_i\rangle\,. \tag{2.4}$$

In quantum mechanics, a way to calculate such probability is to evolve the density matrix in time through the Liouville-von Neumann equation (in natural units, i.e. $\hbar = 1$):

$$\frac{d}{dt}\rho(t) = -i[H, \rho(t)]. \tag{2.5}$$

Let us use the example of a two-neutrino system in order to follow flavor evolution after some propagation in vacuum.

2.1 Two-level system

Since in the mass basis the ν Hamiltonian is diagonal, we can write the two-level system as

$$H = \begin{pmatrix} E_1 & 0 \\ 0 & E_2 \end{pmatrix}\,, \tag{2.6}$$

with $E_i = \sqrt{p^2 + m_i^2}$, with $i = 1, 2$. For all purposes studied in this thesis, $m_j \ll p$ and the energy can be expanded in Taylor series with $m_i^2/p^2 \to 0$, with $p \to E$, thus

$$E_i \sim E + \frac{m_i^2}{2E}. \tag{2.7}$$

It is possible to expand the Hamiltonian into SU(2) generators, the Pauli matrices such that

$$H \approx \begin{pmatrix} E + \frac{m_1^2+m_2^2}{4E} & 0 \\ 0 & E + \frac{m_1^2+m_2^2}{4E} \end{pmatrix} + \begin{pmatrix} \frac{-\Delta m_{21}^2}{4E} & 0 \\ 0 & \frac{\Delta m_{21}^2}{4E} \end{pmatrix} = \left(E + \frac{m_1^2 + m_2^2}{4E}\right)\mathbb{1} - \frac{\Delta m_{21}^2}{4E}\sigma_3\,, \tag{2.8}$$

or

$$H = h_0\mathbb{1} + h_3\sigma_3\,,$$

then obtaining $h_0 = E + \frac{m_1^2+m_2^2}{4E}$ and $h_3 = -\frac{\Delta m_{21}^2}{4E}$, with $h_1 = h_2 = 0$.

Let us make the hypothesis that the neutrino is generated in the mass state ν_1 and we define

$$\rho(0) = \rho_1 = |\nu_1\rangle\langle\nu_1| = \begin{pmatrix} 1 & 0 \\ 0 & 0 \end{pmatrix}\,. \tag{2.9}$$

Let us also suppose that we are interested in finding the probability that, after some propagation, the neutrino arrives in a ν_1 state. Using eq. (2.4), it is possible to get $P_{11} = \mathrm{Tr}[\rho(0)\rho(t)] = \mathrm{Tr}[\rho_1\rho_1] = \mathrm{Tr}[\rho_1] = 1$. There would be no need for such analysis since the ν Hamiltonian in (2.6) is diagonal in the mass basis.

However, it is well known that neutrinos are created in defined flavor states and undefined mass states. In quantum mechanics, it implies that it is possible to write a flavor state as a superposition of mass states, or

$$|\nu_\alpha\rangle = \sum_i U_{\alpha i} |\nu_i\rangle \ , \tag{2.10}$$

with $\alpha = e, \mu, \tau$ and $i = 1, 2, 3$ for active known neutrinos and $U_{\alpha i}$ are elements of the rotation matrix

$$U = \begin{pmatrix} \cos\theta & \sin\theta \\ -\sin\theta & \cos\theta \ , \end{pmatrix} \tag{2.11}$$

that connects both bases. The same unitary transformation can be applied to the density matrix:

$$\rho_\alpha = U\rho U^\dagger \ , \tag{2.12}$$

where the subscript α denotes the flavor basis.

If the neutrino is created in a specific flavor state, e.g. ν_e, with an initial density matrix in the flavor basis

$$\rho_\alpha(0) = \rho_e = |\nu_e\rangle\langle\nu_e| = \begin{pmatrix} 1 & 0 \\ 0 & 0 \end{pmatrix} \ , \tag{2.13}$$

and using the initial condition

$$\rho(0) = U^\dagger \rho_\alpha(0) U = \begin{pmatrix} \cos^2\theta & \sin\theta\cos\theta \\ \sin\theta\cos\theta & \sin^2\theta \end{pmatrix} \ , \tag{2.14}$$

it is possible to use (2.5), after expanding in SU(2) generators in order to find the coefficients from an evolved density matrix such as

$$\rho(t) = \begin{pmatrix} \rho_0(t) + \rho_3(t) & \rho_1(t) - i\rho_2(t) \\ \rho_1(t) + i\rho_2(t) & \rho_0(t) - \rho_3(t) \end{pmatrix} \ , \tag{2.15}$$

to find the coefficients in (2.15)

$$\begin{aligned} \rho_0(t) &= \frac{1}{2} & \rho_2(t) &= \frac{\sin 2\theta}{2}\sin\omega t \\ \rho_1(t) &= \frac{\sin 2\theta}{2}\cos\omega t & \rho_3(t) &= \frac{\cos 2\theta}{2} \end{aligned} \quad , \tag{2.16}$$

and finally the density matrix

$$\rho(t) = \begin{pmatrix} \cos^2\theta & \frac{\sin 2\theta}{2}e^{-i\omega t} \\ \frac{\sin 2\theta}{2}e^{i\omega t} & \sin^2\theta \end{pmatrix} \ , \tag{2.17}$$

where we short-handed $\omega = \frac{\Delta m^2_{21}}{2E}$ and ω represents the oscillation frequency in vacuum. To get the time-evolution in the flavor basis, we need to use again (2.12) to find the electron neutrino survival probability

$$\begin{aligned} P_{ee} = \mathrm{Tr}\left[\rho_\alpha(0)\rho_\alpha(t)\right] &= \sin^4\theta + \cos^4\theta + \sin\theta\cos\theta\sin 2\theta\cos\omega t \\ &= 1 - \sin^2 2\theta \sin^2\left(\frac{\omega t}{2}\right) \end{aligned} \quad , \tag{2.18}$$

where we used the identities

$$\begin{aligned} \sin x\cos x &= \frac{1}{2}\sin 2x \\ \sin^4 x + \cos^4 x &= \cos^2 2x + 2\sin^2 x\cos^2 x \\ \cos 2x &= 1 - 2\sin^2 x \end{aligned} \ . \tag{2.19}$$

2.2 Three-level system

In a more realistic analysis, with the complete set of three active neutrinos, the procedure is similar, despite the expansion of operators in SU(3)

$$\rho = \rho^\mu \lambda_\mu \qquad H = h^\mu \lambda_\mu \ , \tag{2.20}$$

where λ_μ are the generators of SU(3), the Gell-Mann matrices. As in a two-neutrino system, in the mass basis the neutrino Hamiltonian is diagonal, but now it contains two oscillation frequencies, given the two squared mass differences:

$$H = \frac{1}{2E}\begin{pmatrix} 0 & 0 & 0 \\ 0 & \Delta m^2_{21} & 0 \\ 0 & 0 & \Delta m^2_{31} \end{pmatrix} \ , \tag{2.21}$$

and when applied in equation (2.5), no mass state evolve to any other. However, let us again use the hypothesis of a created flavor state ν_e evolving in time. The initial density matrix on the flavor basis would be

$$\rho_\alpha(0) = \begin{pmatrix} 1 & 0 & 0 \\ 0 & 0 & 0 \\ 0 & 0 & 0 \end{pmatrix} , \tag{2.22}$$

that we rotated to the mass basis to a version of (2.11) for three neutrino families, but now with three mixing angles and a phase [5]

$$U = \begin{pmatrix} c_{12}c_{13} & s_{12}c_{13} & s_{13}e^{-i\delta_{CP}} \\ -s_{12}c_{23} - c_{12}s_{13}s_{23}e^{i\delta_{CP}} & c_{12}c_{23} - s_{12}s_{13}s_{23}e^{i\delta_{CP}} & c_{13}s_{23} \\ s_{12}s_{23} - c_{12}s_{13}c_{23}e^{i\delta_{CP}} & -c_{12}s_{23} - s_{12}s_{13}c_{23}e^{i\delta_{CP}} & c_{13}c_{23} \end{pmatrix} , \tag{2.23}$$

with $c_{ij} = \cos\theta_{ij}$ that historically is referred as PMNS matrix [5]. Instead of the mixing angles, for a more clear notation, we will generally refer to the elements of this matrix as $U_{\alpha i}$ for $\alpha = e, \mu, \tau$ representing the rows and $i = 1, 2, 3$ the columns, then (2.23) becomes

$$\rho(0) = \begin{pmatrix} |U_{e1}|^2 & U_{e2}U_{e1}^\star & U_{e3}U_{e1}^\star \\ U_{e1}U_{e2}^\star & |U_{e2}|^2 & U_{e3}U_{e2}^\star \\ U_{e1}U_{e3}^\star & U_{e2}U_{e3}^\star & |U_{e3}|^2 \end{pmatrix} . \tag{2.24}$$

To get the coefficients in (2.20), it is possible to solve the system of linear equations resulting from the SU(3) expansion

$$A = \begin{pmatrix} a_0 + a_3 + \frac{\sqrt{3}a_8}{3} & a_1 - ia_2 & a_4 - ia_5 \\ a_1 + ia_2 & a_0 - a_3 + \frac{\sqrt{3}a_8}{3} & a_6 - ia_7 \\ a_4 + ia_5 & a_6 + ia_7 & a_0 - \frac{2\sqrt{3}a_8}{3} \end{pmatrix} , \tag{2.25}$$

where A stands for ρ and H. However, we also can use the trace properties

$$\mathrm{Tr}[A\lambda_\mu] = \mathrm{Tr}\left[\sum_\nu a_\nu \lambda_\nu \lambda_\mu\right] = k\sum_\nu a_\nu \delta_{\nu\mu} = k a_\mu , \tag{2.26}$$

to get

$$a_\mu = \frac{1}{k}\,\mathrm{Tr}[A\lambda_\mu] \tag{2.27}$$

where μ, ν runs from 0 to 8, k is 2 for $\mu \neq 0$ and 3 otherwise. With (2.27), it is straightforward to see that $h_1 = h_2 = h_4 = h_5 = h_6 = h_7 = 0$ and

$$
\begin{aligned}
h_0 &= \frac{1}{6}\left(\frac{\Delta m^2_{21}}{2E} - \frac{\Delta m^2_{31}}{2E}\right) \\
h_3 &= -\frac{1}{4}\frac{\Delta m^2_{21}}{2E} \\
h_8 &= \frac{1}{4\sqrt{3}}\left(\frac{\Delta m^2_{21}}{2E} - 2\frac{\Delta m^2_{31}}{2E}\right)
\end{aligned}
\quad , \tag{2.28}
$$

for the mass basis Hamiltonian. On the other hand, using the same method, the density matrix coefficients will be

$$
\begin{aligned}
\rho_0 &= \frac{|U_{e1}|^2}{3} + \frac{|U_{e2}|^2}{3} + \frac{|U_{e3}|^2}{3} \\
\rho_1 &= \frac{U_{e1}U^\star_{e2}}{2} + \frac{U_{e2}U^\star_{e1}}{2} \\
\rho_2 &= -\frac{iU_{e1}U^\star_{e2}}{2} + \frac{iU_{e2}U^\star_{e1}}{2} \\
\rho_3 &= \frac{|U_{e1}|^2}{2} - \frac{|U_{e2}|^2}{2} \\
\rho_4 &= \frac{U_{e1}U^\star_{e3}}{2} + \frac{U_{e3}U^\star_{e1}}{2}
\end{aligned}
\qquad
\begin{aligned}
\rho_5 &= -\frac{iU_{e1}U^\star_{e3}}{2} + \frac{iU_{e3}U^\star_{e1}}{2} \\
\rho_6 &= \frac{U_{e2}U^\star_{e3}}{2} + \frac{U_{e3}U^\star_{e2}}{2} \\
\rho_7 &= -\frac{iU_{e2}U^\star_{e3}}{2} + \frac{iU_{e3}U^\star_{e2}}{2} \\
\rho_8 &= \frac{\sqrt{3}|U_{e1}|^2}{6} + \frac{\sqrt{3}|U_{e2}|^2}{6} - \frac{\sqrt{3}|U_{e3}|^2}{3}
\end{aligned}
\quad . \tag{2.29}
$$

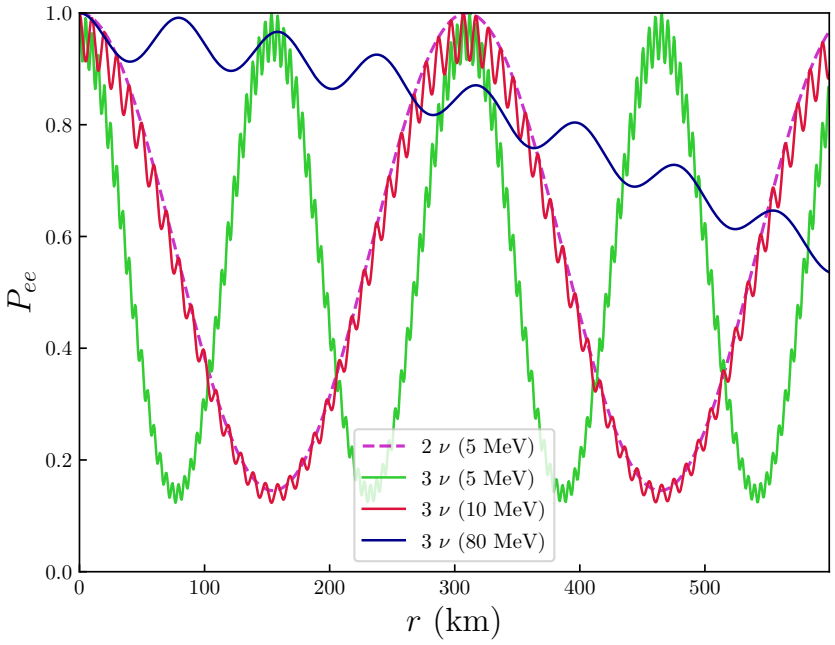

Figure 2 – Survival probability for electron neutrinos in vacuum as a function of a propagated distance r for two and three flavors for various neutrino energies.

Of course, looking at (2.5), it is possible to deduce that h_0 and ρ_0 in the SU(3) expansion do not play any role in the propagation since they are proportional to the identity and such terms vanish in the commutator. The solution for $\rho(t)$ becomes

$$\rho(t) = \begin{pmatrix} |U_{e1}|^2 & U_{e2}U_{e1}^{\star}e^{i\omega_{21}t} & U_{e3}U_{e1}^{\star}e^{i\omega_{31}t} \\ U_{e1}U_{e2}^{\star}e^{-i\omega_{21}t} & |U_{e2}|^2 & U_{e3}U_{e2}^{\star}e^{-i(\omega_{21}-\omega_{31})t} \\ U_{e1}U_{e3}^{\star}e^{-i\omega_{31}t} & U_{e2}U_{e3}^{\star}e^{i(\omega_{21}-\omega_{31})t} & |U_{e3}|^2 \end{pmatrix}, \tag{2.30}$$

where we placed the oscillation frequency in vacuum as $\omega_{kl} = \Delta m_{kl}^2/2E$, which can be transformed back to the flavor basis with (2.12) to use (2.4) in order to calculate the survival probability of electron neutrinos:

$$\begin{aligned} P_{ee}(t) =& |U_{e1}|^4 + |U_{e2}|^4 + |U_{e3}|^4 + 2|U_{e1}|^2|U_{e2}|^2\cos\omega_{21}t + 2|U_{e1}|^2|U_{e3}|^2\cos\omega_{31}t + \\ & |U_{e2}|^2|U_{e3}|^2\left[e^{-i(\omega_{21}+\omega_{31})t} + e^{i(\omega_{21}-\omega_{31})t}\right] \end{aligned}. \tag{2.31}$$

The solutions of (2.18) and (2.31) are shown in Figure 2 for a propagation length r, where natural units were used, then $c = 1$ and $x \sim t$ for ultrarelativistic neutrinos (i.e. neutrino speed is approximately c).

Chapter 3

Neutrino mixing in matter

Neutrinos and antineutrinos only interact by the weak force through the bosons Z^0 and $W^{\pm}$ with charged current interaction to charged leptons and neutral current with all fermions of the standard model:

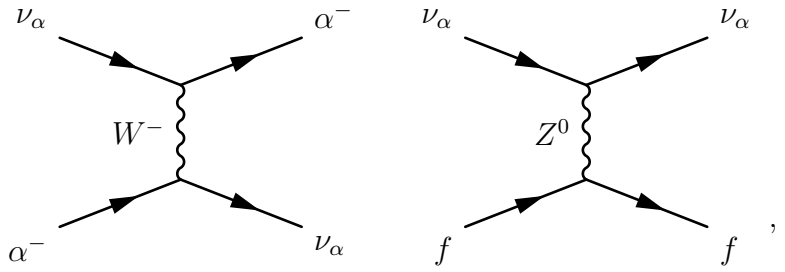

Figure 3 – Feynman diagrams for charged (left) and neutral (right) current neutrino interactions to charged leptons (α^-) and fermions (f) respectively. Similar diagrams could be placed for antineutrinos $\bar{\nu}_\alpha$, switching the signal of charged particles in the charged current diagram (and consequently, the direction of arrows).

implying a very suppressed (anti)neutrino cross-section. One situation where we should care about these interactions and their exact strength is in experimental detection, where many problems in neutrino physics need precise measurements, as shown in the history of neutrino detection, with much effort spent on the subject.

However, in this chapter, we focus our attention on these interactions with matter, with a higher length of propagation (astrophysical objects, such as Earth or stars) to see the implications of neutrino mixing introduced in Chapter 2.

3.1 Effective potential in matter

If a photon is emitted at the Sun's core, it could spend thousands of years to get out until vacuum, eventually reaching Earth, given its relatively high electromagnetic cross-section. On the other hand, neutrinos, with weaker interactions, exit the Sun seconds after being generated, which does not prevent neutrinos from interacting with the dense stellar medium.

In the Sun, most stars, supernovas, and Earth, despite the essentially different composition of these objects, basically are fulfilled with electrons, protons, and neutrons (with residual species of other fundamental or composite particles, such as muons, in a supernova environment). All neutrino species can interact with matter through neutral current interactions, as represented in the Feynman diagram of Figure 4. This interaction does not affect flavor transition and an eventual phase difference of energy eigenstates could be eliminated by a phase shift.

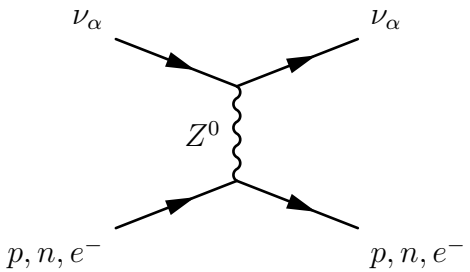

Figure 4 – Feynman diagrams for neutral current with nucleons.

In addition, low-energy astrophysical neutrinos (up to $\sim$ 100 MeV), generated in the Sun (and other stars) and Supernovas, can also interact through charged current to electrons, with Feynman diagrams shown in Figure 5.

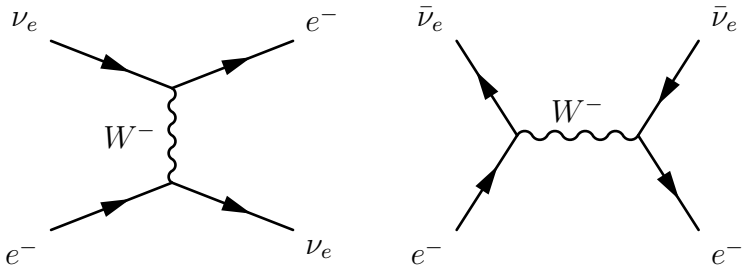

Figure 5 – Feynman diagrams for charged current of ν_e and $\bar{\nu}_e$ with electrons in matter.

Notice that all neutrino flavors are capable of interacting with matter through neutral current, but only electron (anti)neutrinos can interact in the charged current channel[1].

[1] Note that other interactions of neutrinos to protons and neutrons are possible, such as the inverse

This unbalance of (anti)electron neutrinos with more interaction channels than other flavors leads to a modification in the framework described in Section 2, resulting in an effect in neutrino mixing, first realized in mid of the 1970's and 1980s named Mikheyev–Smirnov–Wolfenstein (MSW).

To incorporate matter effects in neutrino propagation, a natural path would be to find the corresponding effective potential in matter given by the diagrams in Figures 4 and 5 and include it into the ν Hamiltonian as an interaction part summed to the vacuum Hamiltonian

$$H_f = H_f^{\text{vac}} + H_I \ , \tag{3.1}$$

where the subscript f means flavor basis, and

$$H_I \left|\nu_\alpha\right\rangle = V \left|\nu_\alpha\right\rangle \tag{3.2}$$

with contributions of neutral and charged currents, or $V = V_Z + V_W$. However, as seen in Section 3, neutrino mixing is an interference phenomenon, and only differences amongst flavor states can be measured. Consequently, an effective interaction for the neutral current does not affect the ν mixing since an interaction Hamiltonian would be proportional to the identity in the flavor basis, but the same is not true for the charged current.

To calculate the effective contribution of the latter interaction, we need some field theory using the diagrams in Figure 5, and the target value is

$$V_W(x) = \left\langle \nu_e(p_1, s_1), e(p_2, s_2)\right| H_W \left|\nu_e(p_1, s_1), e(p_2, s_2)\right\rangle . \tag{3.3}$$

Considering electron neutrinos, if the propagation occurs in isotropic, non-magnetic matter, the corresponding four-current is

$$j^\mu = \bar{\nu}_e(x)\gamma^\mu(1-\gamma^5)e(x) \ , \tag{3.4}$$

leading to a Hamiltonian density

$$\mathcal{H}_W(x) = \frac{G_F}{\sqrt{2}}\ j_\mu j^{\mu\dagger}. \tag{3.5}$$

To proceed, we needed to consider the electron density distribution in the medium as well as to average over their spins, or

$$\mathcal{H}_W(x) = \frac{G_F}{2\sqrt{2}}\ \int f(E_e, T) \sum_{s_2} j_\mu j^{\mu\dagger} d\mathbf{p}_2 \ , \tag{3.6}$$

beta decay, but let us neglect these interactions by now to focus on matter effects in neutrino mixing.

where $f(E_e, T)$ is the normalized Fermi-Dirac distribution and the subscript 2 refers to the electron, as shown in eq. (3.3). To achieve (3.3), we can first use the second quantized field definition

$$\begin{aligned} e(x) &= \sum_{s_2,\mathbf{p}_2} \frac{1}{\sqrt{2V\omega_{\mathbf{p}_2}}} \left[a_{s_2}(\mathbf{p}_2)u_{s_2}(\mathbf{p}_2)e^{-ipx} + b^\dagger_{s_2}(\mathbf{p}_2)v_{s_2}(\mathbf{p}_2)e^{ipx}\right] \\ \bar{e}(x) &= \sum_{s_2,\mathbf{p}_2} \frac{1}{\sqrt{2V\omega_{\mathbf{p}_2}}} \left[a^\dagger_{s_2}(\mathbf{p}_2)\bar{u}_{s_2}(\mathbf{p}_2)e^{ipx} + b_{s_2}(\mathbf{p}_2)\bar{v}_{s_2}(\mathbf{p}_2)e^{-ipx}\right] \end{aligned} \tag{3.7}$$

and

$$\begin{aligned} \nu_e(x) &= \sum_{s_1,\mathbf{p}_1} \frac{1}{\sqrt{2V\omega_{\mathbf{p}_1}}} \left[a_{s_1}(\mathbf{p}_1)u_{s_1}(\mathbf{p}_1)e^{-ipx} + b^\dagger_{s_1}(\mathbf{p}_1)v_{s_1}(\mathbf{p}_1)e^{ipx}\right] \\ \bar{\nu}_e(x) &= \sum_{s_1,\mathbf{p}_1} \frac{1}{\sqrt{2V\omega_{\mathbf{p}_1}}} \left[a^\dagger_{s_1}(\mathbf{p}_1)\bar{u}_{s_1}(\mathbf{p}_1)e^{ipx} + b_{s_1}(\mathbf{p}_1)\bar{v}_{s_1}(\mathbf{p}_1)e^{-ipx}\right] \end{aligned}, \tag{3.8}$$

to check that

$$\begin{aligned} b^\dagger_{s_i}(\mathbf{p}_i)\left|\nu_e(p_1,s_1), e(p_2,s_2)\right\rangle &= 0 \\ \left\langle\nu_e(p_1,s_1), e(p_2,s_2)\right| b_{s_i}(\mathbf{p}_i) &= 0 \end{aligned} \tag{3.9}$$

in order to conserve the lepton number, since we do not expect any considerable fraction of positrons in matter and we are treating only electron neutrinos in this problem (at the end of the derivation it is shown how the antineutrino interaction leads to a similar result), remaining only the first terms on the right-hand side in (3.7). We can insert the bracket from (3.3) in the currents of (3.6) and also make the Fierz transformation to get

$$\begin{aligned} &\left\langle\nu_e(p_1,s_1), e(p_2,s_2)\right| j_\mu j^{\mu\dagger}\left|\nu_e(p_1,s_1), e(p_2,s_2)\right\rangle = \\ &\left\langle\nu_e(p_1,s_1), e(p_2,s_2)\right|\left[\bar{e}(x)\gamma^\mu(1-\gamma^5)\nu_e(x)\right]\left[\bar{\nu}_e(x)\gamma_\mu(1-\gamma_5)e(x)\right]\left|\nu_e(p_1,s_1), e(p_2,s_2)\right\rangle \\ &\left\langle\nu_e(p_1,s_1), e(p_2,s_2)\right|\left[\bar{\nu}_e(x)\gamma^\mu(1-\gamma^5)\nu_e(x)\right]\left[\bar{e}(x)\gamma_\mu(1-\gamma_5)e(x)\right]\left|\nu_e(p_1,s_1), e(p_2,s_2)\right\rangle \end{aligned} \tag{3.10}$$

and use the fields as defined in (3.7) and (3.8) in (3.10), obtaining

$$\frac{1}{4V^2E_{\nu_e}(\mathbf{p}_1)E_e(\mathbf{p}_2)}\langle\nu_e(p_1,s_1),e(p_2,s_2)|\sum_{s_1}\left[a^\dagger_{s_1}(\mathbf{p}_1)\bar{u}_{s_1}(\mathbf{p}_1)e^{ipx}\gamma^\mu(1-\gamma^5)a_{s_1}(\mathbf{p}_1)u_{s_1}(\mathbf{p}_1)e^{-ipx}\right]\times$$
$$\sum_{s_2}\left[a^\dagger_{s_2}(\mathbf{p}_2)\bar{u}_{s_2}(\mathbf{p}_2)e^{ipx}\gamma_\mu(1-\gamma_5)a_{s_2}(\mathbf{p}_2)u_{s_2}(\mathbf{p}_2)e^{-ipx}\right]|\nu_e(p_1,s_1),e(p_2,s_2)\rangle =$$
$$\frac{1}{4V^2E_{\nu_e}(\mathbf{p}_1)E_e(\mathbf{p}_2)}\langle\nu_e(p_1,s_1),e(p_2,s_2)|\sum_{s_1}a^\dagger_{s_1}(\mathbf{p}_1)a_{s_1}(\mathbf{p}_1)\left[\bar{u}_{s_1}(\mathbf{p}_1)\gamma^\mu(1-\gamma^5)u_{s_1}(\mathbf{p}_1)\right]\times$$
$$\sum_{s_2}a^\dagger_{s_2}(\mathbf{p}_2)a_{s_2}(\mathbf{p}_2)\left[\bar{u}_{s_2}(\mathbf{p}_2)\gamma_\mu(1-\gamma_5)u_{s_2}(\mathbf{p}_2)\right]|\nu_e(p_1,s_1),e(p_2,s_2)\rangle \quad , \tag{3.11}$$

where $a^\dagger_{s_i}(\mathbf{p}_i)a_{s_i}(\mathbf{p}_i)$ is the number operator $N_{s_i}(\mathbf{p}_i)$, and we defined $\omega_{\mathbf{p}_i}$ in (3.7) as the energies $E(\mathbf{p}_i)$. We identify that

$$n_e(\mathbf{p}_2)=\frac{N_{s_2}(\mathbf{p}_2)}{V} \tag{3.12}$$

is the electron number density in the medium and $N_{s_1}(\mathbf{p}_1)=1$. We use Casimir's trick in order to obtain

$$\sum_{s_i}[\bar{u}_{s_i}(p_i)\gamma_\mu(1-\gamma_5)u_{s_i}(p_i)]=\mathrm{Tr}[(\not{p}_i+m_e)\gamma^\mu(1-\gamma^5)]=p_{i\alpha}\mathrm{Tr}[\gamma^\alpha\gamma^\mu(1-\gamma^5)]=4p_i^\mu \ , \tag{3.13}$$

that we can use for $i=2$ (and further for $i=1$, as we will see in the derivation). We showed here the form of this procedure opening all quantum fields in terms of creation-annihilation operators and spinors, which is not so common in the literature, but provides a reference for a future interested reader. However, in order to simplify the calculations, let us recover the neutrino quantum fields in the $\nu_e(x)$ and $\bar{\nu}_e(x)$ as in equation (3.10), leading to

$$\langle\nu_e(p_1,s_1),e(p_2,s_2)|\frac{2n_e(\mathbf{p}_2)p_2^\mu}{E_e(\mathbf{p}_2)}\left[\bar{\nu}_e(x)\gamma_\mu(1-\gamma^5)\nu_e(x)\right]|\nu_e(p_1,s_1),e(p_2,s_2)\rangle \tag{3.14}$$

that, when replaced in (3.6) becomes

$$\begin{aligned}\mathcal{H}_W(x)=&\frac{G_F}{\sqrt{2}}\langle\nu_e(p_1,s_1),e(p_2,s_2)|\int f(E_e,T)\frac{n_e(\mathbf{p}_2)p_2^\mu}{E_e(\mathbf{p}_2)}d\mathbf{p}_2\\&\left[\bar{\nu}_e(x)\gamma_\mu(1-\gamma^5)\nu_e(x)\right]|\nu_e(p_1,s_1),e(p_2,s_2)\rangle \ .\end{aligned} \tag{3.15}$$

This result can be simplified over the isotropic assumption of $\int f(E_e,T)\mathbf{p}_2d\mathbf{p}_2=0$, changing $p_2^\mu\to p_2^0=E_e(\mathbf{p}_2)$ and $\gamma_\mu\to\gamma_0$, and also using $\int f(E_e,T)n_e(\mathbf{p}_2)d\mathbf{p}_2=n_e$, we obtain

$$\mathcal{H}_W(x)=\frac{n_eG_F}{\sqrt{2}}\langle\nu_e(p_1,s_1),e(p_2,s_2)|\left[\bar{\nu}_e(x)\gamma_0(1-\gamma^5)\nu_e(x)\right]|\nu_e(p_1,s_1),e(p_2,s_2)\rangle \ , \tag{3.16}$$

and we can use eq.(3.13) again, resulting in

$$\mathcal{H}_W(x) = \frac{2n_e G_F}{E_{\nu_e}(\mathbf{p}_1)\sqrt{2}V} p_1^0 \langle \nu_e(p_1,s_1), e(p_2,s_2) | \nu_e(p_1,s_1), e(p_2,s_2) \rangle \ , \tag{3.17}$$

where we consider normalized states as

$$\langle \nu_e(p_1,s_1), e(p_2,s_2) | \nu_e(p_1,s_1), e(p_2,s_2) \rangle = 1 \ . \tag{3.18}$$

Finally, the effective potential can be calculated using (3.3), (3.17), and the fact that $H_W = \int_V \mathcal{H}_W(\mathbf{x}) d\mathbf{x}$ to obtain

$$V_W = \frac{\sqrt{2}G_F n_e}{V} \int d\mathbf{x} \ , \tag{3.19}$$

that leads to

$$V_W = \sqrt{2}G_F n_e \ . \tag{3.20}$$

Such potential and implications were first derived from [23, 24, 25] and can be seen in less detail, but in a more complete picture in [26] and [27]. For electron antineutrinos, the single difference from (3.19) concerns a minus signal in the result as

$$V_W^{\bar{e}} = -\sqrt{2}G_F n_e. \tag{3.21}$$

The implications of the potential in (3.19) in the neutrino Hamiltonian are as strong as higher the matter density and ν energy can be. However, we will see that the smoothness of the density profile plays an important role in the final ν state, given the equation of motion of quantum mechanics.

As shown in the last section, under a matter potential, the ν Hamiltonian in the flavor basis becomes

$$H_f = \frac{\mathcal{M}}{2E} + V_W(t) \ , \tag{3.22}$$

where $\mathcal{M} = 2EUHU^\dagger = 2EH_f^{\text{vac}}$, and H is the Hamiltonian in the mass basis in (2.6) (for a two-level system). Note that $V_W(t)$ in matrix form is written as

$$V_W(t) = \begin{pmatrix} \sqrt{2}G_F n_e(t) & 0 \\ 0 & 0 \end{pmatrix} \ , \tag{3.23}$$

with only the first line-column term non-null since this potential only affects ν_e in a two-level system of $\nu_f^T = (\nu_e, \nu_\alpha)$, where α takes the place of any active non-electron neutrino flavor.

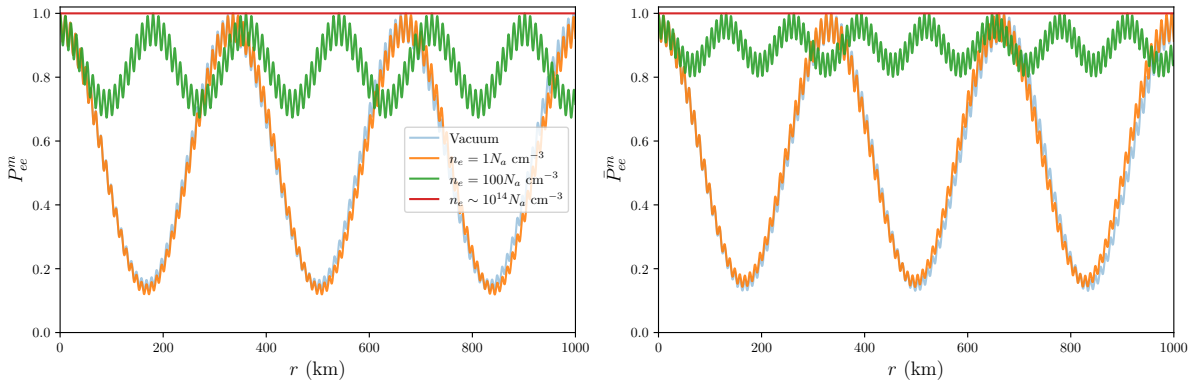

Figure 6 – Survival probability for electron neutrinos (left) and antineutrinos (right) in constant matter densities with $E_\nu = 10$ MeV. N_a is the Avogadro number and n_e is the electron number density (per volume) shown in the last section. The densities 100 N_a cm^{-3} and $\sim 10^{14} N_a$ cm^{-3} are typical of the Sun and Supernova cores, although the density in these environments is variable.

In order to understand the effect of the potential in neutrino mixing, let us simplify the effective potential to a constant one, or $V_W(t) \to V_W = \sqrt{2} G_F n_e$ and see the effect of the additional constant matter potential in the neutrino propagation using the equation of motion discussed in Chapter 2, which leads to Figure 6. It is possible to see that for a very high matter density, no oscillation is expected for ν_e (red curve in Figure 6), i.e. the matter potential suppresses the neutrino coherence, making the flavor Hamiltonian approximately diagonal when high values of electron number density are achieved.

However, a constant matter density is an idealization since in realistic astrophysical environments (stars, Earth, Supernovae), the electron number density is variable along their layers, or $H_f \to H_f(t)$. Let us use our Sun as a study case to understand how this fact changes the neutrino flux composition in compact astrophysical objects.

3.2 Neutrino mixing in our Sun

The solar neutrino problem is a long-term scientific endeavor related to the ν_e flux disappearance in Earth detection, solved by the MSW hypothesis, i.e. using the framework designed in this section. Solar models provide a consistent description of the interior of the Sun, and a density profile such as given by Figure 7 is a robust prediction. As we can see, the solar matter density is far from constant, and the neutrino Hamiltonian in the flavor basis from generation to propagation until the Sun's surface is not constant. Our intention is still to solve the Liouville-von Neumann equation to determine the neutrino's final state.

In this case, a solution for $\rho_\alpha(t)$ and consequently, $P_{\alpha\beta}(t)$ can be obtained from the proper time evolution operator defined as a time-ordered exponential as

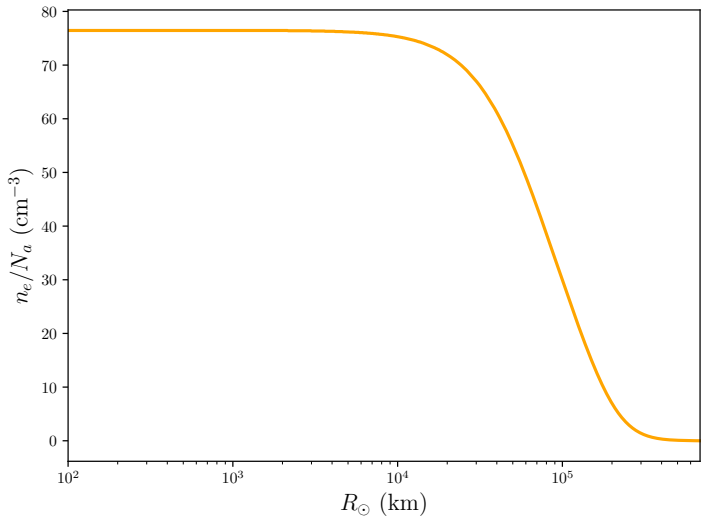

Figure 7 – Electron number density profile of Sun from the BS2005OP solar model taken from [28].

$$\mathcal{U}(t_0,t) = \mathcal{T}\left\{e^{-i\int_{t_0}^{t} dt' H(t')}\right\} = 1 + (-i)\int_{t_0}^{t} dt_1 H(t_1) + (-i)^2 \int_{t_0}^{t} dt_1 \int_{t_0}^{t_1} dt_2 H(t_1)H(t_2) + \cdots \tag{3.24}$$

Instead of solving this Dyson series analytically, it is possible to divide the density profile into small fragments with $\Delta t \to 0$ in which the Hamiltonian is about constant in each step of the propagation, and the time evolution operator becomes

$$\mathcal{U}_i(t_0,t) = e^{-iH_{f_i}(t_i)\Delta t_i} \ , \tag{3.25}$$

where the index i corresponds to the fragment Δt_i, with H_{f_i} being the instantaneous Hamiltonian in the flavor basis at time t_i (edge of Δt_i). Such matrix exponential can be easily solved by diagonalizing the Hamiltonian, taking the exponential of the eigenvalues, and using the proper transformation matrix U_m as

$$\mathcal{U}_i(t_{i-1},t_i) = U_m e^{-iH_m \Delta t_i} U_m^\dagger \tag{3.26}$$

with

$$H_m = \begin{pmatrix} \lambda_1 & 0 \\ 0 & \lambda_2 \end{pmatrix} \ , \tag{3.27}$$

and U_m is a matrix composed of the eigenvectors of the diagonalization. This basis with diagonalized flavor Hamiltonian is denoted as *mass basis in matter*, or effective mass basis. Using this procedure and the recursive application of such operators as

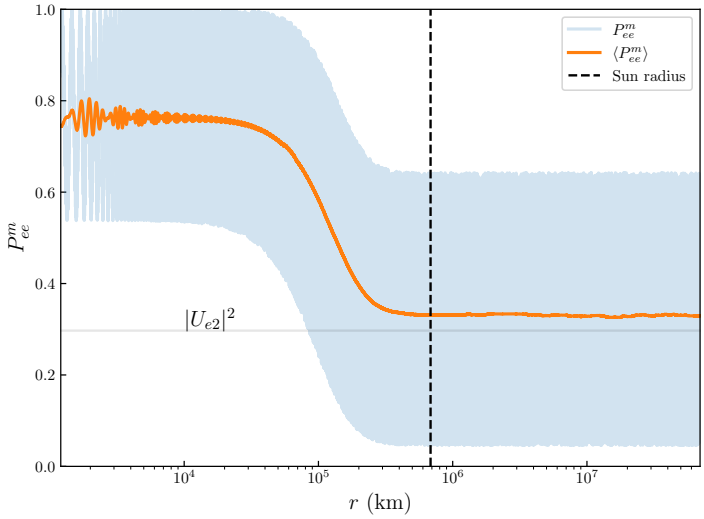

Figure 8 – Survival probability in matter of ν_e along the Sun radius for $E_\nu = 10$ MeV, obtained using the solar profile from Figure 7. The orange curve represents the moving average of P_{ee}^m. Asymptotically, $P_{ee}^m \approx |U_{e2}|^2$, but it does not reach this value, which is a signal that, for the energy used, the ν closely but not completely incoherent.

$$\rho_\alpha(t_{i-1}, t_i) = \mathcal{U}(t_{i-1}, t_i)\rho_\alpha(t_{i-1})\mathcal{U}^\dagger(t_{i-1}, t_i) \tag{3.28}$$

it is possible to solve problems with variable matter density. We will denote this method as the *slab approach* from now on.

An important conceptual remark concerning the neutrino propagation in variable matter density is that the adiabatic theorem, firstly formulated by Landau [29] and Zener [30], could affect neutrino propagation [23, 31, 25]. In summary, it suggests that if an energy state crosses the closest region of two eigenvalues from different eigenstates, a crossing between states is possible if the changes in eigenvalues are fast enough. We introduce a useful condition for the adiabaticity of the system [32]:

$$\gamma = \left| \frac{\dot{\theta}_m}{\lambda_2 - \lambda_1} \right| \ll 1 \ , \tag{3.29}$$

where θ_m is the mixing angle in matter, λ_1 and λ_2 are the eigenvalues of a two-level system, and gamma is commonly denoted as adiabaticity parameter. The mixing angle in matter can be associated with the diagonalization matrix U_m, where its entries are $\cos\theta_m$ and $\sin\theta_m$. The condition in (3.29) (where we refer the derivation in [32] to the interested reader) means that if $\gamma \ll 1$, the system evolves adiabatically, or, more than that, if the mixing angle in matter, and consequently, the matter density, changes slowly, transitions of the kind $\nu_{im} \to \nu_{jm}$ will be suppressed.

Now we have most of the tools in order to handle the solar neutrino problem, and we will use the solar density profile shown in Figure 7, obtained from the solar model

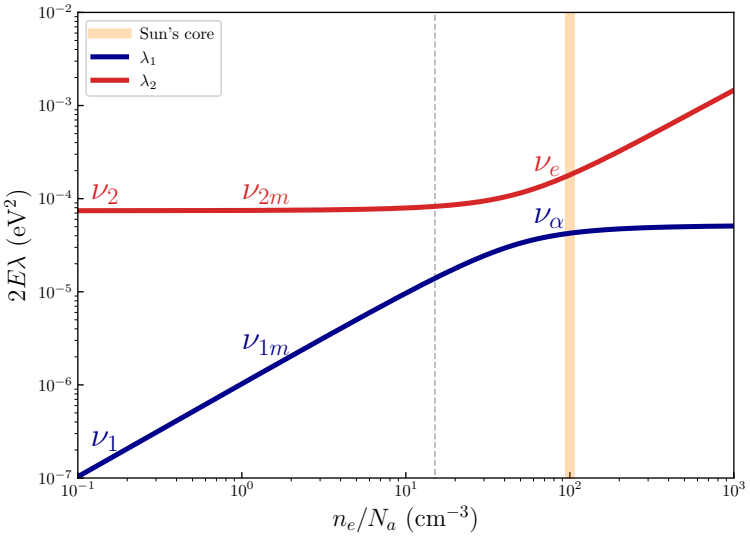

Figure 9 – Eigenvalues of the ν mass basis in matter. The dashed vertical line is the median of the resonance region, with the highest conversion probability of mass states in matter. However nowadays it is well established that this resonance region is adiabatic in the Sun.

presented in [28]. We make the evolution of the density matrix as described previously to get the survival probability of ν_e, or P_{ee} and $\langle P_{ee} \rangle$ (average probability) along the Sun radius. The results are shown in Figure 8. It is possible to see that $\langle P_{ee} \rangle \to |U_{e2}|^2$ when neutrinos approach vacuum. Let us describe the dynamics of neutrino propagation: only ν_e is created since there is not enough energy density to generate ν_μ and ν_τ in the Sun's core; then $P_{e2} \approx 1$, or the electron neutrino is created as almost only neutrino in mass state 2 in matter, i.e. $\nu_e \approx \nu_{2m}$; the neutrino conversion along the Sun is adiabatic, meaning that $P^m_{ij} = 0$ for i, j from 1 to 3, or no conversions amongst mass states in matter are expected, then $P^m_{22} \approx 1$; finally, when the neutrino is going out of matter layers, it crosses a resonance region (inflection point of the sigmoid part oof the orange curve in Figure 8), reaches a mean value of $P_{2e} \approx |U_{e2}|^2$. Summarizing these statements, we get $P_{ee} = P^m_{e2} P^m_{22} P_{2e}$, which is a simple but important method used for the results of this thesis.

Another way to view this phenomenon is by looking at the instantaneous eigenvalues of H_m along propagation in the Sun in Figure 9. The center of the resonance region is highlighted, and we conclude that the resonant conversion in matter happens closer to the outer layers of the Sun, and higher energy neutrinos (in the Sun's spectrum, i.e. $\gtrsim 5$ MeV) are almost incoherent since the probability is averaged out.

Since the electron number density is smooth in the Sun, conversions of the type $\nu_{im} \to \nu_{jm}$ are not relevant; however, for astrophysical neutrinos crossing the Earth before being detected, a density profile from very different matter layers is expected, and we will discuss this possibility in the next section.

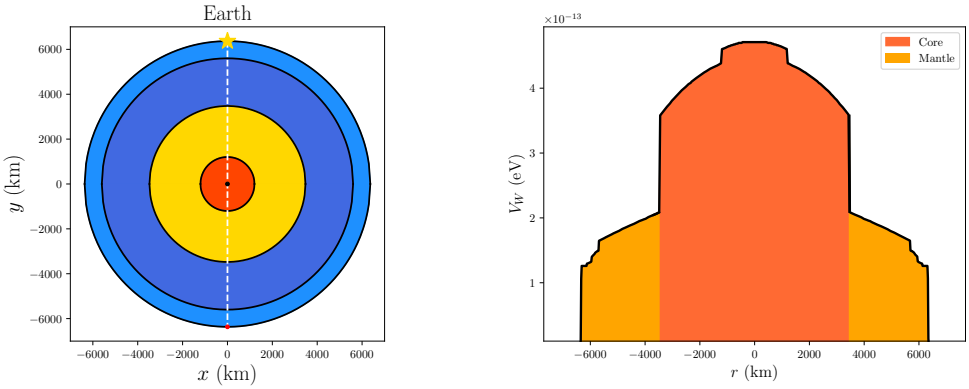

Figure 10 – Pictorial view of a neutrino entering Earth (small red dot), propagating (white dashed) and going out (star) along the entire Earth diameter (left), and charged current potential felt by the same neutrino (right), both as functions of Earth radius. The (0,0) km point means the Earth's center. It was obtained from the density profile from the PREM model [33].

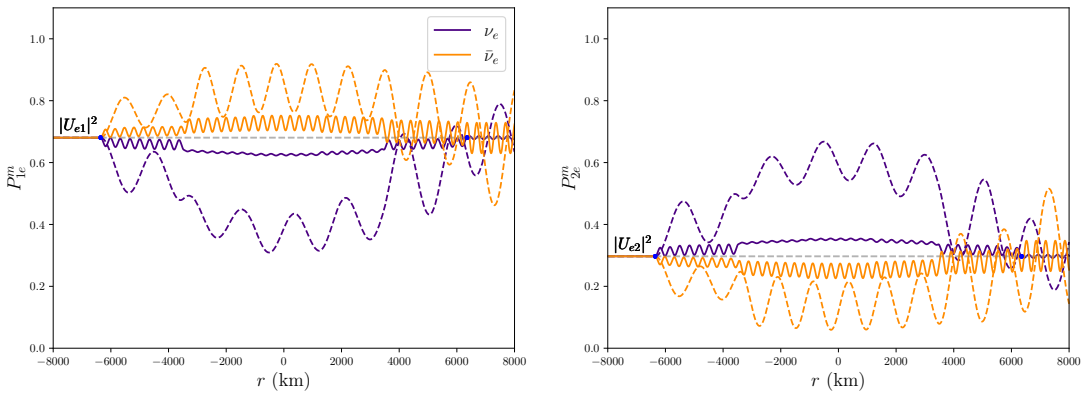

Figure 11 – Probabilities of a neutrino ν_1 (left) and ν_2 (right) arriving at the Earth's surface (left blue dots), passing through the Earth, going out (right blue dots), and being detected as ν_e or $\bar{\nu}_e$ after crossing the entire Earth's diameter. The solid (dashed) line is for a neutrino of 10 (50) MeV.

3.3 Neutrino mixing inside Earth: regeneration effect

The Earth's matter can be divided into three main layers: crust, mantle, and core, with more detailed geological models including sub-layers. To show the effects of neutrino mixing inside the Earth, we use the so-called PREM (Preliminary Reference Earth Model) [33], in order to have a density profile from Earth. In Figure 10, we show the profile of Earth's matter in terms of the charged current potential V_W for neutrinos. We see the high difference in the potential in the interface of mantle and core, differing from the smoothness found in the Sun. Consequently, a neutrino crossing these rough interfaces would suffer non-adiabatic effects in the propagation. Using the same procedure of Section 3.2, we can make some predictions concerning the neutrino mixing after crossing Earth. To take a

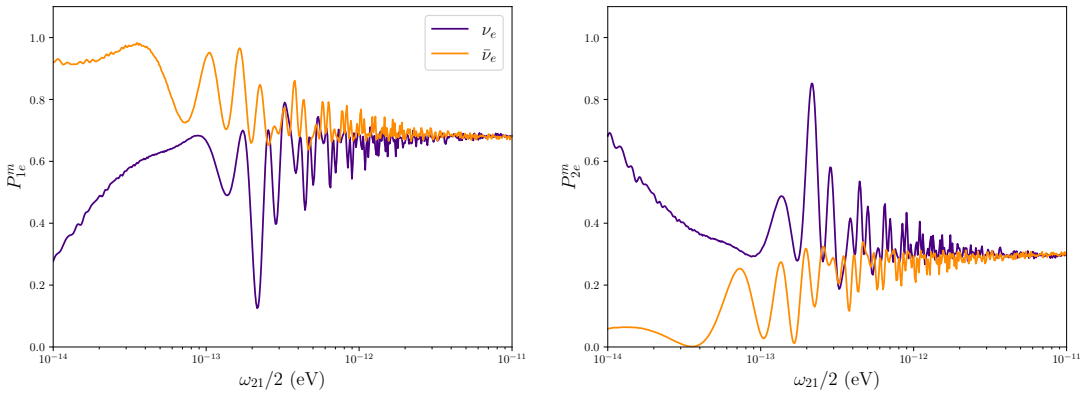

Figure 12 – Probabilities of a neutrino ν_1 (left) and ν_2 (right) crossing the entire Earth diameter and being detected as ν_e at the exit point as a function of $\omega_{21}/2 = \Delta m^2_{21}/4E$.

convenient situation for the purposes of this thesis, we will let an incoherent (pure) neutrino propagation state ν_i arrive at Earth from space and cross the entire Earth's diameter. Note that the convenience of this scenario comes from the fact that such states fit well with solar and supernova neutrinos. Figure 11 shows the corresponding probability of this particular case for ν_e and $\bar{\nu}_e$. It is possible to see that P_{ie} is constant before the neutrino crosses through Earth's matter, and this quantity has an oscillation pattern after passing Earth's surface, or the incoherent neutrino gains some coherence given fast changes in the electron number density. This gain of coherence can be explained by the fact that when the neutrino crosses different Earth layers, an amount of initial ν_i state is converted to ν_j, creating some coherence. It is worth mentioning that the neutrino energy plays an important role in Earth matter effects, as we can see in Figure 11, once for 10 MeV negligible effects are expected, whereas for 50 MeV and beyond, the neutrino composition could be highly affected. To compute this dependency, we can calculate the same probabilities as a function of energy, but now fixing the detection point to the final Earth surface, which is a realistic point of view. Figure 12 shows this dependency as a function of ω_{21}. Recall that $\omega_{21} = \omega_{21}(E)$, and the range of values of this parameter shown in Figure 12 corresponds to $E_\nu \sim 1.9$ MeV ($\omega_{21} = 10^{-11}$ eV) and $E_\nu \sim 1.9$ GeV ($\omega_{21} = 10^{-14}$ eV), showing that only for significantly higher neutrino energies ($E_\nu \gtrsim 40$ MeV) Earth matter effects would start to be more relevant in the overall propagation.

By the end, if some detector is capable of measuring neutrinos that cross the Earth, a common coordinate used to analyze the direction of the entrance is the zenith angle, in which the values of $\theta_z = 0^o$ correspond to a neutrino that comes to a detector from the sky in a perpendicular direction to Earth's surface in the detector point (ν does not cross Earth matter), $\theta_z = 90^o$ is the horizon direction (ν also does not cross Earth matter), and $\theta_z = 180^o$ the neutrino arrives at a detector after crossing the entire Earth diameter. Figures 11 and 12 correspond to $\theta_z = 180^o$. We also could be interested in

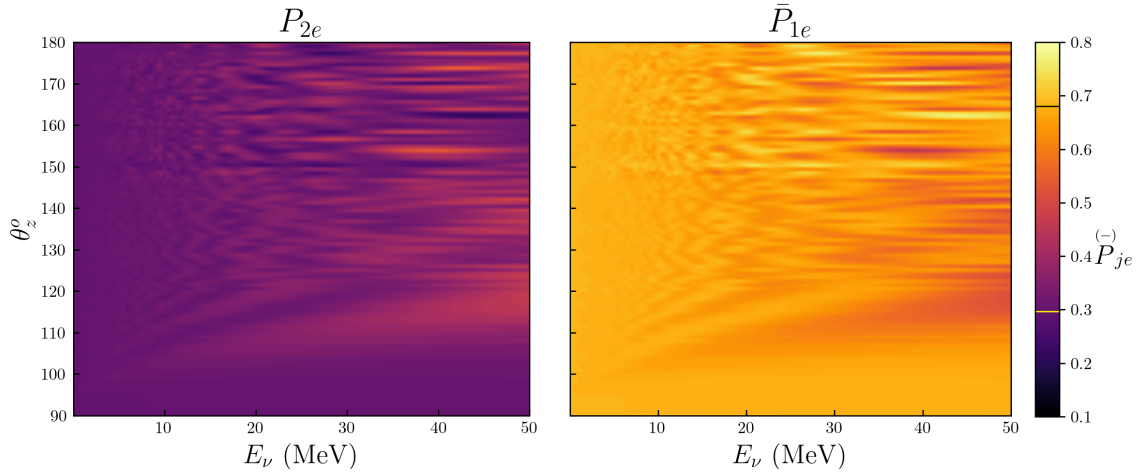

Figure 13 – Probabilities of a neutrino ν_1 (left) and ν_2 (right) crossing the Earth in different zenith angles for a range of neutrino energies. Lines in color scale represent $|U_{e1}|^2$ (black) and $|U_{e2}|^2$ (yellow).

checking the dependency of P_{ie}^m on the zenith angle. Figure 13 shows these probabilities as a function of neutrino energy and zenith angle in the energy scale of the Sun and supernovas. For the further achievements in this work, the remarkable result taken from Figure 12 and Figure 13 is that with neutrino energies of $\lesssim 20$ MeV, regeneration effects are approximately negligible.

Chapter 4

Supernova neutrinos: an inevitable galactic messenger

Stars with $m \gtrsim 10\ M_\odot$ undergo different stages of nuclear fusion. The formation of an iron core with $\sim 1\ M_\odot$ and external shells in an onion structure composed of elements with lighter atomic masses are characteristic of the final stage of such stars. However, iron is a very stable element, that consumes instead of producing energy in a fusion process (iron peak). The result is a fast decrease of the pressure of degenerated electrons in the stellar plasma and the balance of gravitational force and internal pressure reaches a turning point to a collapse of external layers to the core. This event is denoted as a Core-Collapse Supernova (SN) and its consequence is a massive explosion, with no parallel to other events in astrophysics. Of course, large amounts of stellar matter and radiation are expelled and heavier elements are produced in the process, but a remarkable result that we can highlight is the production of neutrinos, with $\sim 99\%$ of the gravitational binding energy of the progenitor star emitted as ν's, or $\sim 10^{53}$ erg, with the flux decreasing proportionally to the distance L as L^{-2}. In the Milky Way, the rate of core-collapse SNs is ~ 1 per century [34], and the next galactic SN is a promising event to test neutrino physics, stellar evolution, and dynamics. The complete process involved in a core-collapse Supernova is out of the scope of this thesis since it would require dedicated work on the subject.

However, we provide a timeline that summarizes the processes emphasizing the neutrino emission [35]:

$\lesssim$ 0 s Before the collapse, the central density and temperature of the progenitor star are $\sim 10^{10}$ g cm^{-3} and 1 MeV. Because of the iron peak, nuclear fuel ends, and the core contracts, then the temperature increases causing the following photo-dissociation

$$\gamma + {}^{56}\mathrm{Fe} \rightarrow 13\alpha + 4n\ , \tag{4.1}$$

in which is a reaction that absorbs 124 MeV, reducing the degenerate electron pressure. Electron Fermi energy is high, favoring the captures

$$e^- + N \rightarrow N^* + \nu_e \ , \tag{4.2}$$

and

$$, e^- + p \rightarrow n + \nu_e \tag{4.3}$$

of nuclei (N) and free protons (p). The reactions decrease the pressure, lowering the Chandrasekhar mass to smaller values. At this point, electron pressure cannot sustain the gravitational force and the star starts to collapse to its core. In the initial phase of electron capture, ν_e propagates freely, until the core density reaches $\sim 3 \times 10^{11}$ g cm^{-3}, becoming opaque to neutrinos;

0 s After $\sim$ 1 s of spatial instability of the star, density reaches $\sim 10^{14}$ g cm^{-3} (which is the approximate nuclear density) stopping the collapse in the core region given by the pressure of the degenerated non-relativistic nucleons, producing a rebound followed by a supersonic shock wave, that is weakened by the energy dissipated in photo-dissociation of nuclei into nucleons. It leads to the production of a large number of electron neutrinos in the process (4.3). This starting point is denoted as *bounce*;

25 ms The shock wave reaches the density of $\sim 10^{11}$ g cm^{-3} a few milliseconds after the bounce, becoming transparent to neutrinos, releasing a large amount of trapped ν_e (and a lower amount of $\bar{\nu}_e$, ν_μ, ν_τ, $\bar{\nu}_\mu$, and $\bar{\nu}_\tau$) with a luminosity of $\gtrsim 10^{51}$ erg s^{-1}. This phase is known in the literature as *neutronization burst* and it is a robust prediction in core-collapse SN;

$\sim$ 0.5 s The neutrino energy deposition behind the weakened shock wave can lead to its revival when matter keeps accreting to the core. This phase is known as *accretion* and occurs in the $\sim$ 0.5 s after the bounce, followed by the supernova explosion with outer layers expelled and the release of $\sim$ 20% of ν's in energy. In the innermost region of the SN core, neutrino density increases rapidly to very high values, with $\nu - \nu$ potential overcoming the neutrino-matter potential, and a non-isotropic neutrino gas is formed in a region denoted as neutrinosphere. Neutrino propagation is treated as a fluid in this region, until reaching a decoupling region where it propagates freely (still interacting with matter in outer layers);

$\sim$ 10 s A formation of a proto-neutron star is induced and cools down emitting $\sim$ 80% of ν's (all flavors) in energy with a thermal flux. This phase is known as *cooling*. The neutrinosphere is still active in this phase.

Historically, we were capable of detecting neutrinos only once from a supernova. The SN1987A was an important event in neutrino physics and it is discussed in Chapter 5, but first, let us understand the standard supernova ν mixing in more detail since it is related to the main topic of this thesis.

4.1 Neutrino-matter effects in supernovas

In Section 3, we discussed the MSW effect in the context of solar neutrinos, where a 2-level system was enough to describe a solution of the solar flavor composition. As we will see, in the supernova framework, we need the 3-ν system to describe supernova matter effects. We can rewrite (3.22), the flavor Hamiltonian for neutrinos propagating in matter for a 3-level system as

$$H_f(x) = \frac{1}{2E}\begin{pmatrix} m^2_{ee} + 2EV_W(x) & m^2_{e\mu} & m^2_{e\tau} \\ m^2_{\mu e} & m^2_{\mu\mu} & m^2_{\mu\tau} \\ m^2_{\tau e} & m^2_{\tau\mu} & m^2_{\tau\tau} \end{pmatrix}, \tag{4.4}$$

where $m^2_{\alpha\beta}$ short-handed elements from $\mathcal{M}$ as $m^2_{\alpha\beta} = m^2_{\beta\alpha}$. If we provide a proper rotation that diagonalizes the sector $\mu\tau$ as

$$H_f(x) = \frac{1}{2E}\begin{pmatrix} m^2_{ee} + 2EV_W(x) & m^2_{e\mu'} & m^2_{e\tau'} \\ m^2_{\mu' e} & m^2_{\mu'\mu'} & 0 \\ m^2_{\tau' e} & 0 & m^2_{\tau'\tau'} \end{pmatrix}, \tag{4.5}$$

the physics remains unchanged [36], and the Hamiltonian becomes approximately diagonal, or $H_f \approx \frac{1}{2E}(2EV_W(x), m^2_{\mu'\mu'}, m^2_{\tau'\tau'})$. It means that, in this picture, neutrinos are created in incoherent states inside the supernovas, given the high matter density in the creation region. It is worth mentioning that ν_μ, ν_τ, $\bar{\nu}_\mu$, and $\bar{\nu}_\tau$ are indistinguishable in the detection since the only possible detection channel for these flavors is the elastic scattering, in which the flavor can not be determined. For this reason and the fact that their initial fluxes from the SN are approximately equal, we set any non-electron neutrinos as ν_x (as widely used in the literature).

As in Section 3, we again resort to diagonalizing H_f to get eigenvalues and eigenvectors from a proper unitary transformation in order to understand MSW effects inside the SN. Figure 14 shows the eigenvalues of the flavor Hamiltonian. It is possible to see that when we consider a 3-ν system, a new resonance region arises for higher densities (an electron number density of $\sim 10^3\ n_e/N_a\ \text{cm}^{-3}$ for a ~ 10 MeV neutrino energy), allowing transitions of the kind $\nu_{2m} \leftrightarrow \nu_{3m}$. This density is not achievable in the Sun, but it is easily realizable in a typical supernova. For this reason, this resonance is commonly denoted as H (High-density resonance), whereas the "solar" resonance, inducing transitions of

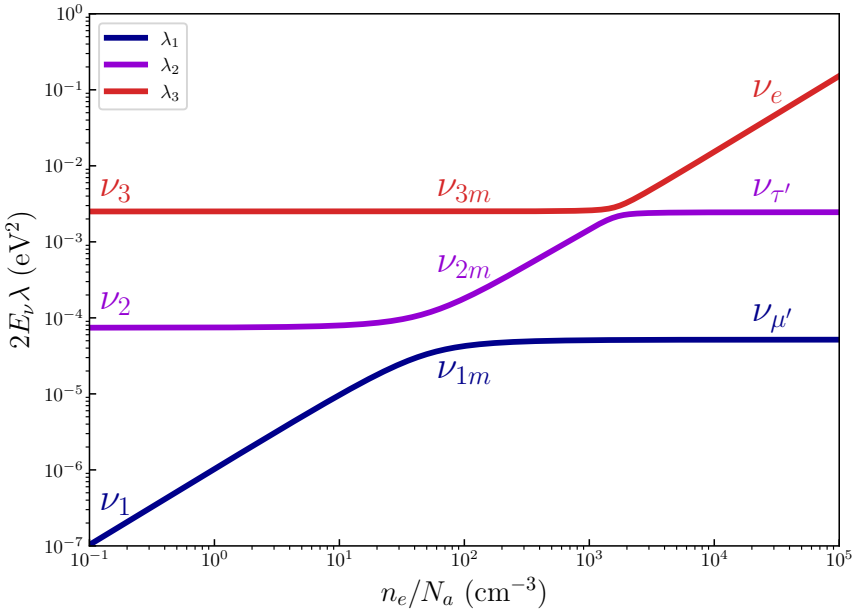

Figure 14 – Eigenvalues of H_f as a function of the electron number density n_e for normal mass hierarchy (NH). The neutrino energy E_ν is taken to be 10 MeV in $2E_\nu\lambda$.

$\nu_{1m} \leftrightarrow \nu_{2m}$ in densities about $\sim 50\ n_e/N_a$ cm^{-3} is denoted as L (Low-density). Note that the non-electron neutrinos are labeled as $\nu_{\mu'}$ and $\nu_{\tau'}$, highlighting that these are not the conventional flavor states ν_μ and ν_τ, but a rotated basis where these two flavors coincide to mass states in matter. It is not the case for ν_μ and ν_τ, since they are created as a combination of ν_{1m} and ν_{2m} instead. It is also important to mention that Figure 14 corresponds to NH (least to most energetic state is $\nu_{1m} \to \nu_{2m} \to \nu_{3m}$), and a different scenario is expected to IH ($\nu_{3m} \to \nu_{1m} \to \nu_{2m}$). In NH, the most energetic state in matter is ν_{3m}, then, it is associated with ν_e given the increase of effective energy of this flavor by the charge current potential $V_W(x)$. As we can note, in IH ν_e coincides to ν_{2m}. The flavor states in both hierarchies are generated in the following instantaneous energy states in matter:

$$\begin{array}{cc} \text{NH} & \text{IH} \\ \nu_e = \nu_{3m} \quad \nu_{\tau'} = \nu_{2m} \quad \nu_{\mu'} = \nu_{1m} & \nu_e = \nu_{2m} \quad \nu_{\mu'} = \nu_{1m} \quad \nu_{\tau'} = \nu_{3m}\ , \\ \bar{\nu}_{\tau'} = \bar{\nu}_{3m} \quad \bar{\nu}_{\mu'} = \bar{\nu}_{2m} \quad \bar{\nu}_e = \bar{\nu}_{1m} & \bar{\nu}_{\mu'} = \bar{\nu}_{2m} \quad \bar{\nu}_{\tau'} = \bar{\nu}_{1m} \quad \bar{\nu}_e = \bar{\nu}_{3m} \end{array} \tag{4.6}$$

where equal signs could be taken with a grain of salt, since a residual superposition of energy states does exist, but for all purposes of neutrino mixing, they are completely negligible.

As discussed in Chapter 3, in the MSW effect, the conversion of mass states in matter ν_{im} is possible in the resonance regions (minimum distances in energy from eigenvalues of

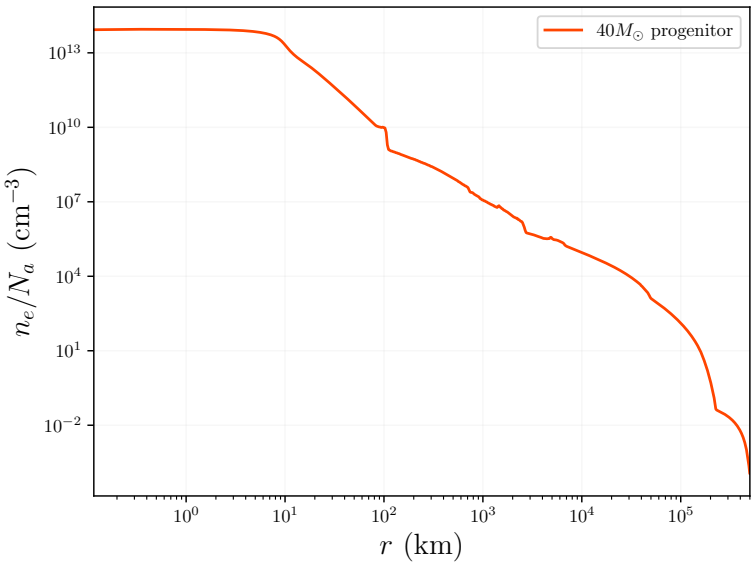

Figure 15 – Snapshot (at 27 ms after the core bounce) of simulated SN electron density profile from a progenitor mass of 40 $M_\odot$ [40].

Figure 14). This probability (sometimes referred to as flipping or crossing) in a simplified format is given by [37, 38]

$$P_{\mathrm{H,L}} = e^{-\frac{\pi\gamma}{2}} \tag{4.7}$$

that decreases with the adiabaticity parameter γ, defined in eq.(3.29), and we explicitly write as [30, 31]:

$$\gamma = \frac{{\Delta m_{ij}}^2 \sin\theta_{ij}}{2E\cos 2\theta_{ij}(1/n_e)dn_e/dr} \quad . \tag{4.8}$$

Note that γ depends on flavor conversion parameters, neutrino energy as well as the density profile of the medium. More specifically, large variations in the electron number density increase the probability of changing between energy levels. As it is widely discussed in the literature, the L resonance is adiabatic, which makes $P_{\mathrm{L}} \sim 0$ from now on [39]. The H resonance could be non-adiabatic in accretion or cooling when the shock wave propagates along the resonance region, but for the neutronization burst, the complete neutrino propagation is adiabatic.

Using Figure 14, we can calculate the probabilities of ν mass states at the surface of the SN when the generated neutrino is ν_e. The electron neutrino in NH is created as ν_{3m}, then the probability of generation in this mass state in matter is $P^m_{e3} = 1$. The probability of keeping the state ν_{3m} in propagation is a measure of how unlikely the transition $\nu_{3m} \to \nu_{2m}$ would occur, which is $1 - P_{\mathrm{H}}$ (since P_{H} is the flip probability related to this transition in NH). Then the probability of obtaining the state ν_3 becomes $P_{e3} = P^m_{e3}P^m_{33} = 1 - P_{\mathrm{H}}$. For ν_{2m} and ν_{1m} we get $P_{e2} = P^m_{e3}P^m_{32} = P_{\mathrm{H}}$ and $P_{e1} = P^m_{e3}P^m_{31} = P_{\mathrm{H}}P_{\mathrm{L}}$. Note that the L

resonance is adiabatic, then $P_{e1} \sim 0$. Now it becomes easy to include a detection of ν_e at Earth, writing the survival probability as

$$P_{ee} = P_{e1}P_{1e} + P_{e2}P_{2e} + P_{e3}P_{3e} = P_{\rm H}P_{2e} + (1 - P_{\rm H})P_{3e} \ , \tag{4.9}$$

where $P_{2e} = |U_{e2}|^2$ and $P_{3e} = |U_{e3}|^2$. Following the same procedure for $\bar{\nu}_e$ we obtain

$$\bar{P}_{ee} = P_{1e} \tag{4.10}$$

in NH. We also can work out the probabilities for IH, that differ from the above ones, since each flavor is generated in other mass states in matter:

$$\begin{aligned} P_{ee} &= P_{2e} \\ \bar{P}_{ee} &= \bar{P}_{\rm H}P_{1e} + (1 - \bar{P}_{\rm H})P_{3e} \end{aligned} \ . \tag{4.11}$$

For an adiabatic propagation $P_{\rm H} = P_{\rm L} = 0$ and the above probabilities become

$$\begin{array}{ll} \text{NH} & \text{IH} \\ P_{ee} = |U_{e3}|^2 & P_{ee} = |U_{e2}|^2 \\ \bar{P}_{ee} = |U_{e1}|^2 & \bar{P}_{ee} = |U_{e3}|^2 \end{array} \ . \tag{4.12}$$

Of course, the same numerical calculation of P_{ee} shown in Chapter 3 in the context of solar neutrinos could be performed for SNs. Our knowledge of the solar density profile is much more accurate than that of a typical SN; however, advanced supernova simulations could in principle provide matter density profiles varying along the time of the explosion, as shown in Figure 22 of [39]. Different working groups generate supernova simulations with such information. In Figure 15, we show the electron number density of simulated SN with a progenitor mass of 40 $M_\odot$ at 27 ms after core bounce, provided by the Garching group [40, 41]. Using this simulated profile and the procedure described in Chapter 3, the slab approach, it is possible to calculate P_{ee} and $\bar{P}_{ee}$. These probabilities are shown in Figure 16 for both neutrino hierarchies. Note that the conversion for this specific matter density profile is adiabatic since asymptotically the probabilities go to $|U_{ei}|^2$ values.

These two probabilities are special because they can completely parameterize the neutrino flux at Earth. To show it, we can use the initial ($\phi^0_{\nu_\alpha}$) and final (ϕ_{ν_α}) neutrino fluxes from a SN, where $\alpha = e, x$, in addition to the corresponding antineutrinos. Note that we set again non-electron neutrino flavors as x. If the requirement of flux conservation is achieved, the flux at Earth can be written as follows [36]:

$$\begin{aligned} \phi_{\nu_e} &= \phi^0_{\nu_e}P_{ee} + \phi^0_{\nu_x}(1 - P_{ee}) \\ \phi_{\bar{\nu}_e} &= \phi^0_{\bar{\nu}_e}\bar{P}_{ee} + \phi^0_{\nu_x}(1 - \bar{P}_{ee}) \\ \phi_{\nu_x} &= \phi^0_{\nu_e}(1 - P_{ee}) + \phi^0_{\nu_x}(2 + P_{ee} + \bar{P}_{ee}) + \phi^0_{\bar{\nu}_e}(1 - \bar{P}_{ee}) \end{aligned} \ . \tag{4.13}$$

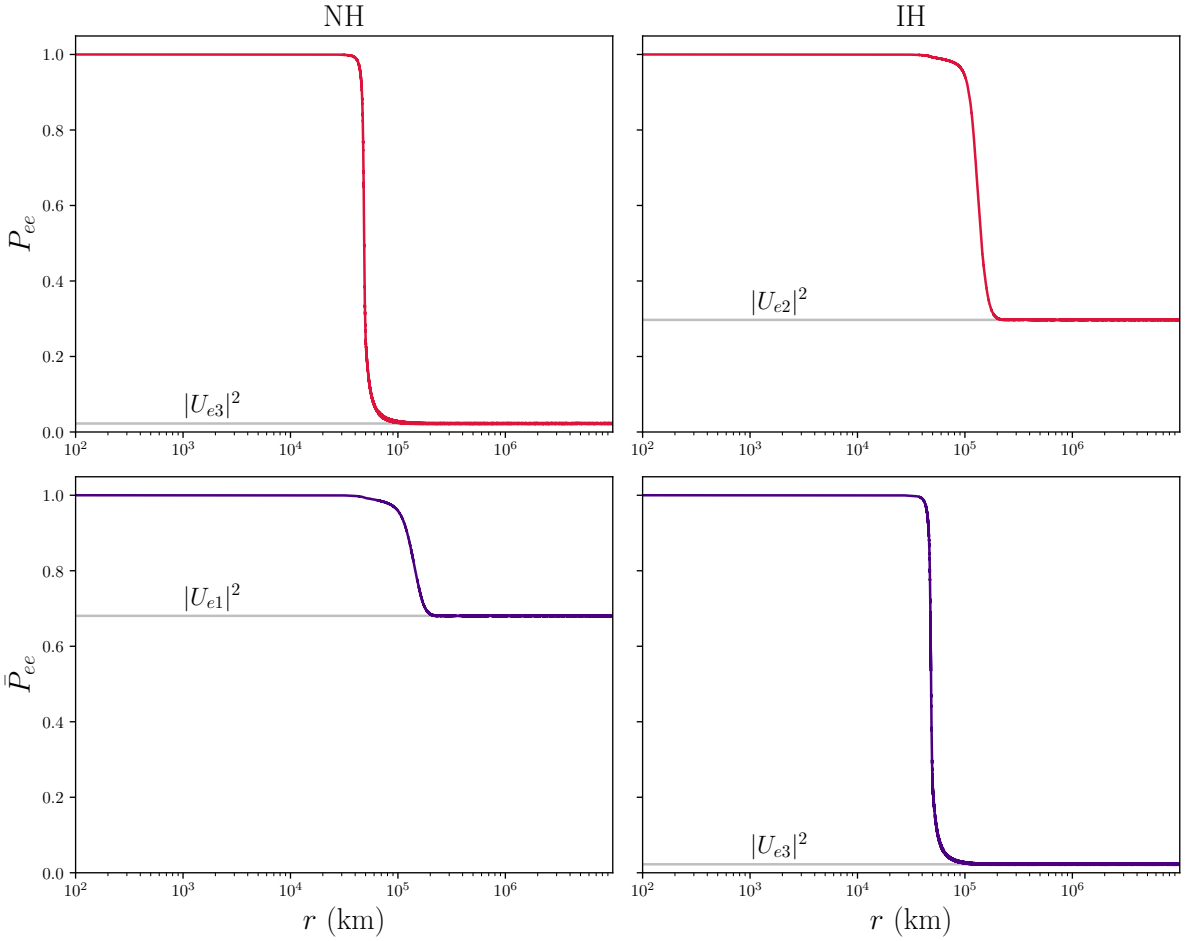

Figure 16 – Numerically solved survival probabilities of ν_e and $\bar{\nu}_e$ inside a supernova. The density profile simulation used is shown in Figure 15. The left column corresponds to NH and the right one the IH scenario.

In Figure 17, a snapshot of different flavors is shown in the instant of time $t \sim 27$ ms (end of neutronization burst), using initial fluxes $\phi^0_{\nu_\beta}$ from the simulated SN explosion with progenitor mass of 40 $M_\odot$ used to calculate the survival probabilities above. It is possible to see that both hierarchy scenarios provide a large difference from initial fluxes, and more than this, with a precise measurement of ν_e, a future SN detection would potentially determine the neutrino mass hierarchy. We will discuss more about these modern simulations in Chapter 7.

This flavor conversion scheme establishes the current standard picture of supernova neutrinos, and we will recall this construction when we start to discuss possible quantum decoherence effects in supernova neutrinos in Chapter 7. Detailed studies beyond the presented scenarios in this section have been carried out [42, 43], but they are dependent on more precise SN simulations and further improvements in the knowledge of SN formation.

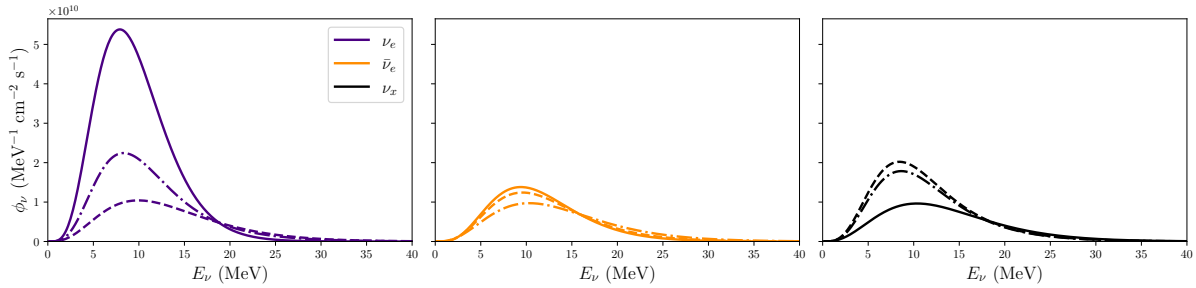

Figure 17 – Initial neutrino flux (solid), and neutrino flux after conversion for NH (dashed) and IH (dash-dot) at 30 ms for a simulation of a progenitor star with 40 $M_\odot$ provided by the Garching group [40]. We take the assumption of adiabatic conversion in the calculation.

4.2 Challenges in supernova neutrino mixing

Although the mechanism beyond the MSW effect is very well known, as shown in Section 4.1, a complete solution for the supernova neutrino-mixing is far from being accomplished nowadays. It is given by a number of distinct factors we briefly describe in a random order of importance:

- **Supernovae simulations**: a number of research groups have been extensively generating sophisticated simulations of supernova explosions. We refer here to recent works such as [39, 44]. Despite the great advances in the topic, there is much to be done in order to get a realistic scenario of a supernova explosion, such as the inclusion of flavor conversion in neutrino evolution of the simulated neutrino path;

- **Non-adiabatic MSW effect**: considering this resonant effect led by neutrino interaction to matter (discussed in Section 4.1), in accretion and cooling emission phases, there is a possible non-adiabatic transition along Supernova layers, induced by the ν-crossing of the shock-wave or turbulent regions [42]. Detailed simulations should be needed to precisely understand how MSW effects would affect flavor conversion in this regime. It is worth mentioning that in the neutronization burst phase, the propagation is completely adiabatic;

- **Collective effects**: the large ν-luminosity induces a dense neutrino gas in the supernova core, being one of the only places in the Universe with such an environment. In addition to the conventional matter interactions, a non-isotropic neutrino potential is induced in a very inner region denoted as neutrinosphere, and flavor conversion could be highly affected by the presence of $\nu - \nu$ potential in the equation of motion, leading to a so-called collective effect, with the origin of the name given by the fact that incoherent neutrinos start to oscillate collectively in equal frequency, given by effects of forward neutrino scattering with other neutrinos [39, 45, 46]. The difficulty

in solving the equation of motion is given by the non-linear nature of the $\nu - \nu$ potential, leading to a non-linear partial differential Boltzmann-like equation of motion:

$$\partial_t \varrho_{\mathbf{p},\mathbf{x},t} + \mathbf{v}_\mathbf{p} \cdot \nabla_\mathbf{x} \varrho_{\mathbf{p},\mathbf{x},t} = -i[\Omega_{\mathbf{p},\mathbf{x},t}, \varrho_{\mathbf{p},\mathbf{x},t}] + \mathcal{C}(\varrho_{\mathbf{p},\mathbf{x},t}) \ , \tag{4.14}$$

where $\varrho_{\mathbf{p},\mathbf{x},t}$ is the matrix of densities[1], $\mathbf{v}_\mathbf{p}$ is the neutrino velocity, $\mathcal{C}(\varrho_{\mathbf{p},\mathbf{x},t})$ is a collision term, and

$$\Omega_\mathbf{p} = \Omega_{\text{vac}} + \Omega_{\text{MSW}} + \Omega_{\nu\nu} \ , \tag{4.15}$$

with Ω_{vac} and Ω_{MSW} corresponding to the vacuum and matter Hamiltonian respectively, already discussed in previous chapters. The $\Omega_{\nu\nu}$ term regards the $\nu - \nu$ potential and is given by

$$\Omega_{\nu\nu} = \sqrt{2} G_F \int \frac{d^3\mathbf{q}}{(2\pi)^3} (\varrho_\mathbf{q} - \bar{\varrho}_\mathbf{q})(1 - \mathbf{v}_\mathbf{p} \cdot \mathbf{v}_\mathbf{q}) \ . \tag{4.16}$$

Solving the equation above for approximate neutrino backgrounds leads to slow flavor oscillation effects, where the neutrino can be converted in a timescale of vacuum oscillation frequency $\omega = \Delta m^2/2E \cong 6.1 \text{ km}^{-1}/E$ (MeV). In more realistic scenarios in terms of neutrinos generated in a SN, also the so-called fast oscillations, engendered by different decoupling regions of flavors in the neutrinosphere could make the neutrino flavor composition even harder to be calculated since transitions could be induced in timescales orders of magnitude lower than slow oscillations, and instabilities of solutions of the equation of motion are expected [45]. The problem becomes even more difficult when we take into account that it affects the supernova simulations, and it is also dependent on the output of the simulations, making it a recursive problem still unsolved at the time this thesis is been written. Due to the high uncertainties surrounding the results for a realistic scenario involving collective effects in SN emission, *we will not address this issue here in any of our analyses*. It is also important to mention that we do not expect the neutronization burst to be affected by collective effects, but it could completely change flavor conversion in the accretion and cooling phases;

- **Neutrino mass hierarchy**: despite our precise measurements of the square difference of neutrino masses Δm^2_{21} and Δm^2_{31} from flavor conversion experiments, we still do not know if $m_3 > m_2 > m_1$ (normal hierarchy, or NH) or $m_2 > m_1 > m_3$ (inverted hierarchy, or IH). It is known in the literature as neutrino mass hierarchy (or ordering). As we saw in Section 4.1, the solution to the resonant matter effect is highly dependent on the ν-hierarchy scenario.

Although the community has made efforts to be experimentally and theoretically prepared for the next galactic SN, we were able to detect neutrinos from a neighboring

[1] Field theory correspondent to quantum mechanical density matrix, defined as $\varrho_{\mathbf{p},\mathbf{x},t} = \langle \mathbf{a}^\dagger_\mathbf{p}(t) \mathbf{a}_{\mathbf{p}'}(t) \rangle$.

galaxy in the past, the SN1987A, which provided valuable information from the dynamics of a supernova neutrino emission, and we will discuss this important event in neutrino physics and astrophysics along the next chapter.

Chapter 5

SN1987A

In 1987, in the Large Magellanic Cloud, the progenitor star Sanduleak-69 202 with $M \sim 20\ M_\odot$ became a supernova. At 50 kpc from Earth (outside the Milky Way), it was the first detection of neutrinos created outside our solar system, inaugurating the era of experimental neutrino astronomy.

Since it was outside our galaxy, the ν flux was limited at Earth, but even though, three detectors were capable of observing a neutrino signal: Kamiokande II [47, 48], IMB [49, 50] and Baksan [51]. Figure 18 shows the time and energy of the detected events.

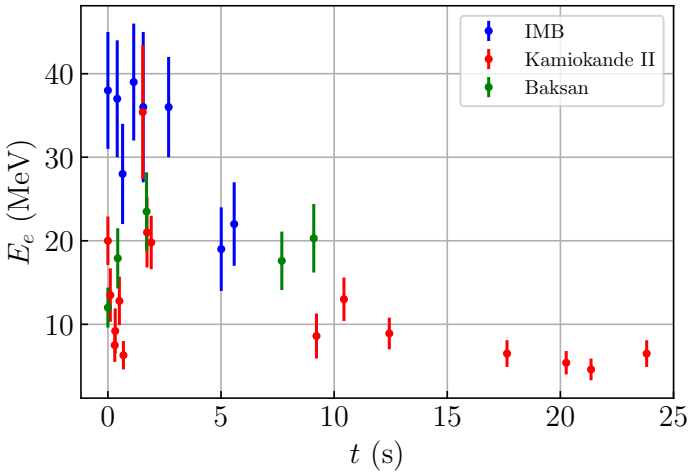

Figure 18 – SN1987A events. E_e refers to the positron energy detected.

To clarify the ideas concerning the data analysis of such important astrophysical phenomena, in the next section, we show results from our publication in [52]. In the sequence, in Section 5.2, we also discuss possible limits in neutrino flavor conversion using SN1987A data in our publication in [53].

5.1 Understanding and visualizing the statistical analysis of SN1987A neutrino data

As shown in Figure 18, the statistics of SN1987A measurements is very limited. To extract any physics from a data analysis using those events requires more than a binned statistical method, such as least squares. Therefore, as proposed in [52], we will describe the maximum likelihood estimation using this data, fitting a simplified neutrino emission model for that SN.

5.1.1 Modelling SN1987A event-by-event likelihood

Frequently, the likelihood treatment in particle physics involves the usage of the Poisson distribution $P(\mu, n)$, which fits well to phenomena that have a small probability of occurring, but a large number of tries. Given a measured variable set $\vec{x}$, the Poisson likelihood is given by:

$$\mathcal{L} = \prod_{i=1}^{N_{bins}} \frac{\mu(x_i)^{n_i}}{n_i!} e^{\mu(x_i)} \ , \tag{5.1}$$

where n_i can be a particular number of events that occurs in a $x_i + \delta x_i$ interval of our variable, in a number N of intervals, or bins, and $\mu(x_i)$ is the expected value in the same interval. It is convenient to write $\mu(x_i)$ as a distribution function on the variable x_i, or $\mu(x_i) = R(x_i)\delta x_i$, with a given event rate $R(x_i) = \frac{dN}{dx_i}$ in an equally spaced bin of variable δx_i and a number of counts n_i. Including it in equation (5.1), we obtain:

$$\begin{aligned} \mathcal{L} &= \prod_{i=1}^{N_{bins}} \frac{[R(x_i)\delta x]^{n_i}}{n_i!} e^{-R(x_i)\delta x} \\ &= e^{-\sum_{j=1}^{N_{bins}} R(x_j)\delta x} \prod_{i=1}^{N_{bins}} \frac{[R(x_i)\delta x]^{n_i}}{n_i!} \ . \end{aligned} \tag{5.2}$$

However, binning the data to use a single expected value of a set of points requires assuming a given statistical distribution of such a bin, that generally is considered to be Gaussian for a higher number of entries. If the low statistics scenario does not allow this assumption, then it is possible to model the likelihood (5.2) to account for each event apart. This can be made by taking the bin to an infinitesimal width $\delta x \to dx$ and number of counts $n_i \to 1$, so we consider only infinitesimal bins with one event and drop the others, then (5.2) becomes

$$\mathcal{L} \propto e^{-\int R(x)dx} \prod_{i=1}^{N_{obs}} R(x_i) \ , \tag{5.3}$$

that also has the change from the total number of bins N_{bins} to the total number of observed events N_{obs} and the index i accounts for each individual event. The idea behind maximum likelihood is to maximize the quantity in (5.3), or given the correspondence $\mathcal{L} = e^{-\chi^2/2}$, minimize the $\chi^2(\vec{x}) = -2\log\mathcal{L}(\vec{x})$ with respect to a free set of parameters $\vec{x}$. If we have a single event at $x = \bar{x}$, this expressions reduces to $e^{-\int R(x)dx}R(\bar{x})$. For different models with a normalized expected event rate $\int R(x)dx$, the likelihood is maximized for the model with the highest value of $R(x_i)$. Letting the normalization run freely, it is maximized for $\int R(x)dx = 1$. It is straightforward to note that if we consider more than one single event, this maximum occurs on the total number of events.

In a supernova detection, such as SN1987A, the variables x are the neutrino energy, the detection time, and events scattering angle, i.e. $R = R(E, t, \cos\theta)$ [54]:

$$R(E, t, \cos\theta) = n_p \frac{d\sigma(E_\nu, \cos\theta)}{d\cos\theta} \frac{d^2\phi_{\bar{\nu}_e}(E_\nu, t)}{dE_\nu dt} \xi(\cos\theta)\eta(E_e)\frac{dE_\nu}{dE_e} \ , \tag{5.4}$$

with n_p being the number of free protons of each detector, $\sigma(E_\nu, \cos\theta)$ is the inverse beta decay cross section [55], $\phi_{\bar{\nu}_e}(E_\nu, t)$ represents the electron antineutrino flux at Earth, $\xi(\cos\theta)$ is an angular bias of IMB detector and $\eta(E_e)$ is an efficiency function taken from [51] that fits the reported efficiency points from each collaboration.

Then eq. (5.3) becomes:

$$\mathcal{L} = e^{-\int R(E,t,\cos\theta)\, dE\, dt\, d\cos\theta} \prod_{i=1}^{N_{obs}} R(E_i, t_i, \cos\theta_i)\, dE\, dt\, d\cos\theta \ , \tag{5.5}$$

where R is a triple differential equation, $R = \frac{d^3N}{dE\, dt\, d\cos\theta}$ and N is the expected number of events at the detector. A complete analysis, including other details such as background and energy resolution, can be seen in [54, 56, 57, 58, 59, 60].

5.1.2 Single event distribution

The main ingredient to construct the likelihood is the theoretical triply differential expected rate. However, since there is no way to convert the theoretical predictions into some quantity to be compared with individual events, we can instead modify the events to match the theoretical probability distribution. For instance, all SN1987A events are published with uncertainty in energy, so the true information we can take from each event is a probability distribution around some most probable results. Assuming such distribution to be Gaussian, a specific event with measured energy $\bar{E}_\nu \pm \sigma_E$, where σ_E is the energy uncertainty, measured on time $\bar{t} \pm \sigma_t$, with σ_t being the uncertainty in time, is

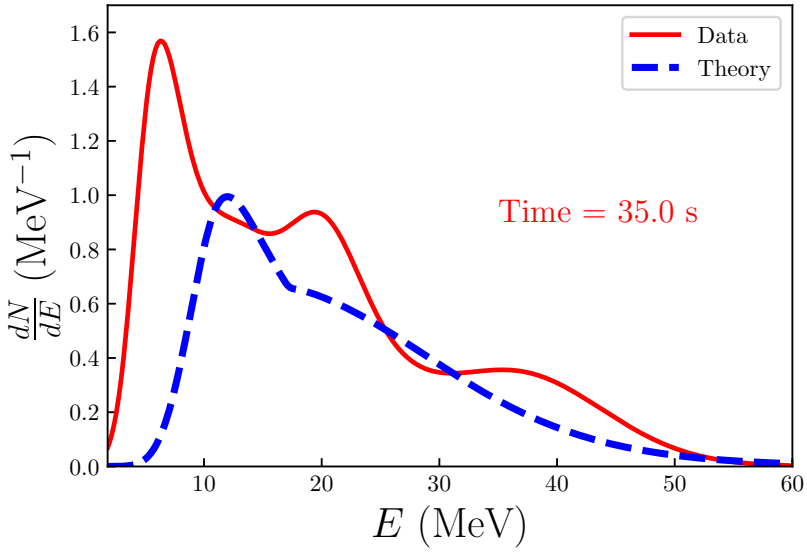

Figure 19 – Theoretical cumulative event rate integrated over time (eq. 5.7) (blue) and normally distributed data as proposed in (5.8) (red) changing along the relative detection time since the first measured neutrino from SN1987A. The time scale runs logarithmically in the first second and linearly afterward to better show the data structure for early time events (see the animation here).

related to the following probability distribution:

$$\begin{aligned}\frac{d^2P(E_\nu,t)}{dE_\nu\,dt} =& \frac{1}{\sigma_E\sqrt{2\pi}}\exp\left[\left(-\frac{1}{2}\frac{(E_\nu-\bar{E}_\nu)^2}{\sigma_E^2}\right)\right] \\ &\times \frac{1}{\sigma_t\sqrt{2\pi}}\exp\left[\left(-\frac{1}{2}\frac{(t-\bar{t})^2}{\sigma_t^2}\right)\right]\end{aligned}\ , \tag{5.6}$$

where $P(E_\nu,t)$ is the probability that the event had true energy between E_ν and $E_\nu+dE_\nu$, and was measured in the true time between t and $t+dt$.

This result can be compared with the theoretical probability of inducing an event on the detector:

$$\frac{d^2N}{dE_\nu\,dt} = A\,\frac{d^2\phi(E_\nu,t)}{dE_\nu\,dt}\,\sigma(E_\nu)\ , \tag{5.7}$$

where A is a normalization constant that takes into account the number of targets in the detector and its efficiency. The neutrino interaction cross section is given by $\sigma(E_\nu)$, and $\phi(E_\nu,t)$ is the neutrino flux. The specific parameterization of these two last functions will be presented in the sequence. To properly visualize the data points being collected, we can create an animation with the detected event probability integrated on time[1]. Since the uncertainty on time is very small, the distribution converges to a δ-function, and such

[1] The reader is invited to check the animations of this section in order to follow the discussion. The links are in the description of each Figure.

animation would advance in steps while the data gets collected:

$$\sum_i \frac{dP_i(E_\nu,t)}{dE_\nu} = \int_{t_0}^{t} dt \sum_i \frac{d^2P_i(E_\nu,t)}{dE_\nu\, dt} = \sum_i \frac{1}{\sigma_{E_i}\sqrt{2\pi}} \exp\left[\left(-\frac{1}{2}\frac{(E_\nu - \bar{E}_{\nu i})^2}{\sigma_{E_i}^2}\right)\right]\theta(t-t_i) \quad . \tag{5.8}$$

Such animation is presented in Figure 19 (red curve). Since what is presented is the cumulative result after integrating on time, the final moment of this animation, when integrated also on energy, provides all the 29 events detected by the three experiments. The comparison with theoretical predictions can be made visually if we produce a similar animation for the expected number of events, integrating eq. (5.7) on time, also presented in Figure 19 (dashed curve). This method of a model-independent curve representing the spectrum has already been fully discussed in [61, 62, 63], where references [62, 63] also bring a comparative analysis to neutrino emission models[2].

The parameterization of the electron antineutrino[3] flux $\phi(E_\nu, t)$ in eq. (5.7) follows the model of reference [54] and consists of a two-component emission (accretion + cooling) with nine free parameters that come from the proposed flux $\phi = \phi(t, E, \cos\theta, \vec{y})$, with $\vec{y} = (T_c, R_c, \tau_c, T_a, M_a, \tau_a)$, where T_c (T_a) is the initial antineutrino (positron) temperature from the cooling (accretion) phase, R_c is the radius of the neutrinosphere, τ_c (τ_a) is the characteristic time from the cooling (accretion) phase and M_a is the initial accreting mass. In the following, we state the emission models used in this section with the initial accretion and cooling fluxes:

- Accretion flux: physically, a flux of positrons in static neutron targets generating neutrinos reasonably mimics the expected $\bar{\nu}_e$ generation process when the star mass accretes to its core; then this situation can be given by:

$$\phi^0_{a,\bar{\nu}_e}(E_\nu, t) = \frac{8\pi c}{(hc)^3}\left[N_n(t)\sigma_{e^+n}(E_\nu)g_{e^+}(E_{e+}, T_a)\right] \ , \tag{5.9}$$

$$N_n(t) = \frac{Y_n}{m_n} \times M_a \times \frac{j_k(t)}{1 + t/0.5s} \ ,$$
$$g_{e^+}(E_{e+}, T_a) = \frac{E_{e+}^2}{1 + \exp\left[E_{e+}/T_a\right]} \ , \tag{5.10}$$

where $N_n(t)$ is the neutron distribution as a function of the emission time, $\sigma_{e^+n}(E_\nu)$ is the positron-neutron cross-section, and $g_{e^+}(E_{e+}, T_a)$ is the thermal distribution of

[2] While reference [62] compares the data curve to a Fermi-Dirac spectrum, [63] uses a neutrino fluence $\propto E^2/T^4 e^{-E/T}$, where E and T are energy and temperature of the electron antineutrino.

[3] Since the detectors in 1987 were capable of measuring a single channel, the inverse beta decay ($\bar{\nu}_e + p \to e^+ + n$), only electron antineutrinos could be detected.

positrons with energy E_{e+} in a temperature T_a. The number of neutrons is given by the initial accreting mass M_a with a fraction of neutrons Y_n, and its time behavior is given by the factor $j_k(t) = \exp\left[-(t/\tau_a)^k\right]$, with τ_a being the characteristic time of the accretion phase and the parameter $k = 2$ following the parameterization in [54];

- Cooling flux: this flux can be modeled by a black body emission of the recently created proto-neutron star:

$$\phi^0_{c,\bar{\nu}_\alpha}(E_\nu, t) = \frac{\pi c}{(hc)^3} 4\pi R_c^2 \frac{E_\nu^2}{1 + \exp[E_\nu/T_c(t)]} \ , \tag{5.11}$$

with the cooling temperature being a function of time

$$T_c(t) = T_{c,\bar{\nu}_\alpha} \exp\left[-t/\left(4\tau_c\right)\right] . \tag{5.12}$$

The parameters of the model above are estimated from an event-by-event maximum likelihood, and the best-fit values of our analysis, used in Figure 19, are:

$$T_c = 5.1\,\mathrm{MeV},\ R_c = 12\,\mathrm{km},\ \tau_c = 4.3\,\mathrm{s}, \tag{5.13}$$

$$T_a = 1.7\,\mathrm{MeV},\ M_a = 1.2\,M_\odot,\ \tau_a = 0.7\,\mathrm{s}\ . \tag{5.14}$$

As described before, the maximization of the likelihood depends on two terms. The term in the exponential factor is related to the number of events and drives the theoretical parameters to those who provide the right expected number of events, i.e., the area under the curves at the end of the animation in Figure 19. It is quite easy to grasp if the theoretical model fits well the data in this aspect.

The second term assesses how close the theoretical curve is to the experimental one at the data central points, both in energy and in time. Since the uncertainty in time is negligible, we can visually compare the curves at the moment new data is collected, providing a visual tool for this second ingredient of the statistical analysis. By performing these two analyses in Figure 19, we can expect that, although not perfect, the theoretical prediction would provide a reasonably good fit to the data.

It is useful now to analyze a set of theoretical parameters that do not fit well the data. This is done in Figure 20, where we chose two sets of parameters that are excluded at 90% C.L. according to our analysis. These parameters were chosen in a way not to change the total number of predicted events, so we can focus on the energy spectrum information. It is clear, again using a visual comparison, that this new set of parameters produces a worse fit to the data, a fact that is confirmed by a full statistical analysis.

As was pointed out earlier, the two main neutrino observables that we are taking into consideration are the neutrino energy and the time of detection. After discussing the first in the above analysis, we will now focus on the second. The best way to do this is to determine the limits in neutrino mass that can be achieved using this statistical method.

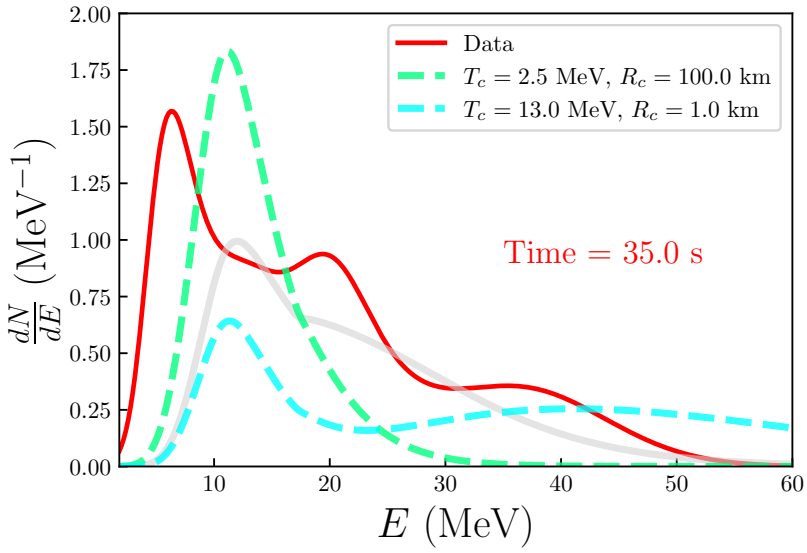

Figure 20 – To visualize the effect of spectral distortion impact on event rate, we used two sets of parameters for T_a and M_a (in green and in cyan) that are excluded at 90% C.L. according to our analysis. The green curve produces a distortion for low-energy events, while the cyan produces a distortion that favors high-energy events. Also on light grey we present the best-fit point of our analyses, shown in Figure 18 (see the animation here).

5.1.3 Neutrino mass limits

An important remark is that the neutrino detection spread in time is an important source of physical information, allowing us to probe both Supernova explosion mechanisms and neutrino properties. One important neutrino property with effects seen in the time spread of the distribution of events is its mass.

The first difficulty in this kind of analysis is that the data itself does not allow us to correlate the time of arrival of the neutrino burst at the detectors with the unknown time at which the neutrinos left the Supernova. The solution is to use the data itself to establish, through statistical analysis, the match between the theoretically predicted neutrino flux and the data, taking the time of arrival of the first neutrino event in each detector as a marker. The time of the following events, t_i are taken as relative ones to the time of arrival of the first event, t_1:

$$\delta_i = t_i - t_1$$

and t_1 is left to vary freely to best match the theoretical prediction in a previously established time scale.

This simple picture arises when we assume massless neutrinos. In this case, the relative time between events is identical to the relative time between the emission of these detected neutrinos on the production site since the time delay due to the travel between

the supernova and the detectors does not depend on the neutrino properties. In Figure 19 a vanishing neutrino mass is assumed, and the time shown in the animation corresponds to the time since the supernova offset.

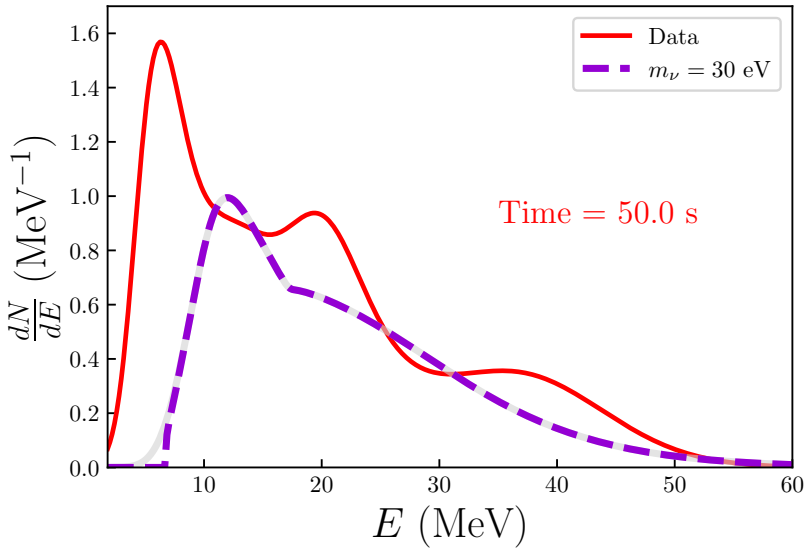

Figure 21 – Effect of neutrino mass delay on the SN1987A detected burst compared to the standard flux for a 3σ excluded neutrino mass. The gray line corresponds to the fitted theory in Figure 19 (see the animation here).

However, since the neutrinos have mass, neutrinos with different energies have different velocities, which changes the described scenario. More energetic neutrinos travel faster than less energetic neutrinos, meaning that the relative times between events do not correspond to the relative times of the neutrino emission. The correction is done by a simple kinematic analysis:

$$t_{i.d} = t_{i,p} + \frac{L}{v_i} = t_{i,p} + \frac{L}{c}\sqrt{1 - \frac{m^2}{p_i^2}} \sim t_{i,p} + \frac{L}{c}\left(1 - \frac{m^2}{2E_i^2}\right)$$

where L is the distance to the supernova, and m and E are the neutrino mass and event energy. The sub-index p (d) refers to the time at production (detection). The emission time of each event is then calculated from the relative times δ_i, and the kinematic corrections:

$$\begin{aligned} t_{i,d} &= t_{1,d} + \delta_i \\ t_{i,p} &= \delta_i + \left(t_{i,p} - \frac{L}{c}\frac{m^2}{2E_1^2}\right) + \frac{L}{c}\frac{m^2}{2E_i^2} \ . \end{aligned} \tag{5.15}$$

For more details see [64, 65].

Instead of making the correction on the time of the production, presented here to give proper credit to the authors that proposed and performed this analysis, we prefer to correct the theoretical predictions by a continuous spread in time on the neutrino flux

spectrum at the detector. So, instead of converting the time of the detected events to the supernova emission, we adjust the theoretical prediction to the detector site. Clearly, both choices are equivalent, but with this second procedure we can use the same data animation presented in Figure 19, and adjust the theoretical curve by making the replacement:

$$t \to t - \frac{L}{c}\frac{m^2}{2E^2}$$

in eq. (5.7).

An animation evidencing this model-independent limit is shown in Figure 21, where we chose an exceeding neutrino mass of 30 eV, highly beyond astrophysical limits of ~ 5 eV [64, 65] in order to effectively visualize the delay caused by mass, with the same astrophysical parameters used to produce Figure 19, and then with the same neutrino flux at the source. However, due to the different time lags of neutrinos traveling to Earth with different energies, the time history of the expected number of events changes significantly, allowing us to place a limit on neutrino data analysis using proper statistical techniques.

The pedagogical view of the particular SN1987A data analysis in this section provided a first step further to face possible problems to be investigated with SN1987A detection. In the next section, we perform a very similar analysis to potentially impose limits on neutrino mixing in this supernova.

5.2 SN1987A neutrino burst: limits on flavor conversion

In the context of the SN1987A analysis elucidated in the last section, we could be interested not only in how the data translate the SN-ν properties through emission parameters but also in understanding if this data would possibly provide some limits over expected ranges of parameters. It enables us to provide more accurate reporting of our expectations and prevents outcomes based on simple statistical fluctuations that best-fit values are susceptible to. In summary, every measurement should be aggregated into more detailed studies of their uncertainties. Using the same maximum likelihood estimation described in Section 5.1, in addition to a more sophisticated treatment of detector efficiencies shown in detail in [53], we perform this uncertainty estimation in Figure 22, which describes the allowed regions considering the cooling parameters R_c (neutrinosphere radius) and T_c (initial cooling temperature) for 68% and 90% C.L. We also compare our analysis to previous ones in the literature. The differences in the results are related to updated oscillation parameters and different approaches to detector efficiencies as well as in the statistical method.

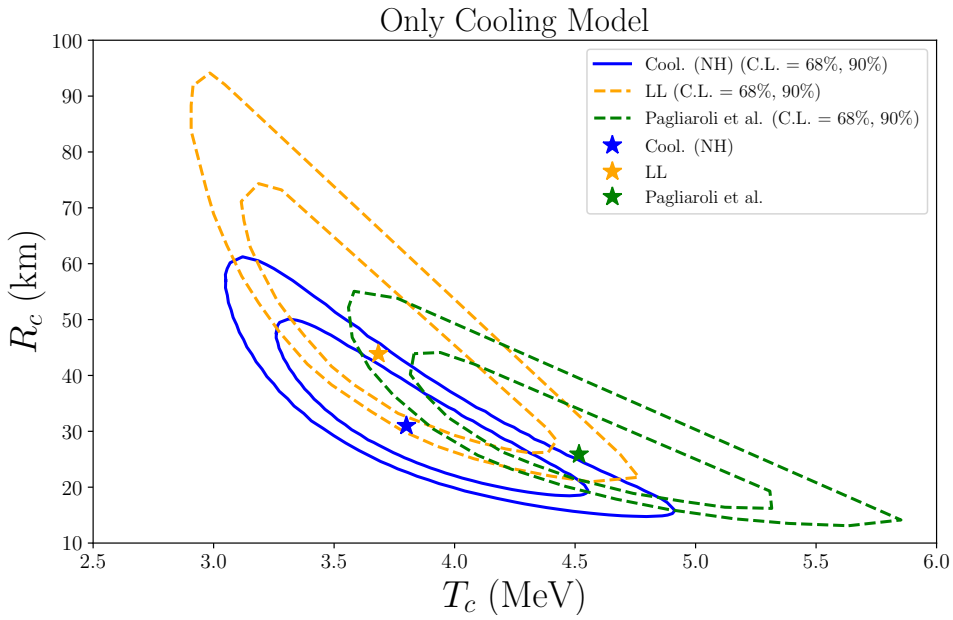

Figure 22 – Allowed regions for cooling temperature (T_c) and neutrinosphere radius (R_c) with 68% and 90% C.L (blue). LL shorthand Loredo and Lamb from [64] (orange) and Pagliaroli et. al refers to [54] (green).

The above discussion shows the possibility of bound SN-ν emission models, and one could ask if limits on the neutrino flavor conversion could also be achieved using SN1987A data. Any analysis should deal with scenarios that we better understand in neutrino mixing, such as the resonant matter effect, or MSW (explained in Chapter 4). Of course, amongst the possible flavor conversion scenarios, the MSW is the most robust prediction, taken as the standard neutrino mixing scheme in SN-ν in most of the prospective works in the literature. As already explained, this effect describes ν_e and $\bar{\nu}_e$ creation in incoherent propagation states ν_{im}. At the resonance regions in supernova layers, the conversion of mass states in matter of the type $\nu_{im} \rightarrow \nu_{jm}$ could occur. In any case, these flavor states are converted to ν_x in an amount proportional to the module square of entries of the PMNS matrix, even in the adiabatic regime. Note that for adiabatic propagation, the survival probabilities P_{ee} and $\bar{P}_{ee}$ are simply constants (see eq. 4.12). Using the statistical analysis of the last section, an idea that appears is: could we treat $\bar{P}_{ee}$ as a free parameter and also marginalize it to check if SN1987A data would prefer some region of parameter space? The answer to this question is yes if we consider the MSW as the single conversion effect, with the assumption of adiabatic propagation.

Using the same emission model described in Section 5.1 and performing the maximum likelihood estimation, marginalizing over $\bar{P}_{ee}$, we can impose limits on this survival probability. Figure 23 shows this marginalization. The remarkable feature of this result is that adiabatic MSW in IH is rejected with more than 2σ of significance, favoring the NH scenario as the correct solution of neutrino mass hierarchy. Note that different fixed initial

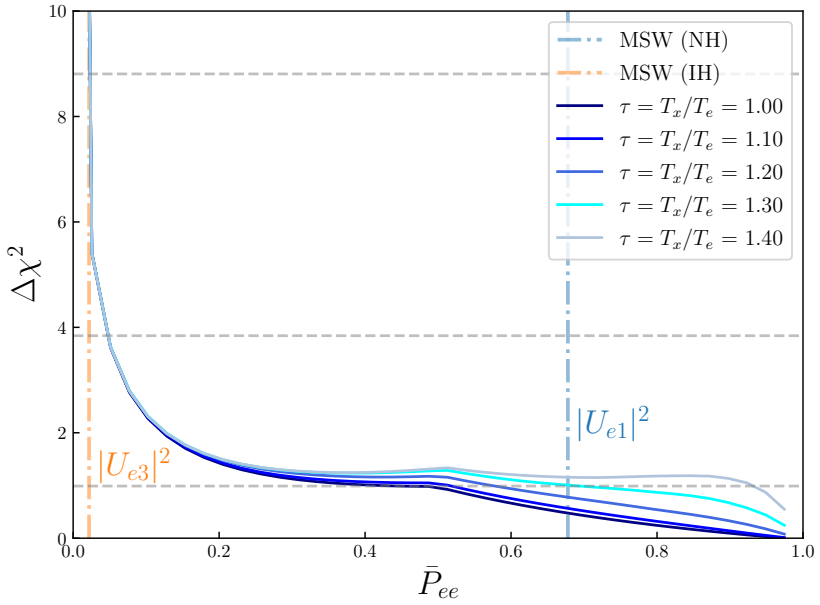

Figure 23 – $\Delta\chi^2$ for $\bar{P}_{ee}$ using SN1987A data, considering the cooling + accretion model for various initial temperature ratios (τ) of nu_x and $\bar{\nu}_e$. The horizontal dashed lines correspond to 1, 2 and 3σ of C.L. Vertical lines show the MSW adiabatic solution for normal and inverted hierarchies.

temperature ratios $\tau = T_x/T_e$ were tested, with minor impacts on the results. More details of this analysis are in reference [53].

Chapter 6

On the issue of pure to mixed quantum states

In the 1970s, Hawking established the so-called black hole thermodynamics and stated the possibility of particle creation in black hole event horizons in his seminal papers [66, 67]. Surprisingly, analyzing the implications of such effect, he shows, through an analysis of the final stage of black hole evaporation, and based on expected fluctuations of the space-time metric in candidate theories of quantum gravity, that pure quantum states could be induced to mixed ones [68, 3]. Many authors discussed the subject over the next decades [69, 70, 71, 72, 73, 74, 75], but the quantum gravity problem and its stochastic nature remain unsolved nowadays.

One argument that prevailed in the community is the possible open nature of quantum systems, immersed in this stochastic "foamy" quantum gravitational environment (even in vacuum), and proposals to evolution equations concerning an extension of quantum mechanics were done in mid-1984 [70, 69]. Curiously, years before such derivation, in 1976, proposals for a generalized equation of motion for open quantum systems were rigorously detailed in the simultaneous works of Gorini, Kossakowski, Sudarshan [76] and Lindblad [77], resulting in the known Gorini-Kossakowski-Sudarshan-Lindblad (GKSL) master equation.

In order to test open quantum systems in particle physics, detailed analyses using neutral kaon oscillation and neutron interferometry were performed [69, 78, 79], and the first hints in the use of the macroscopic quantum oscillation length of neutrinos came along in 2000 with the works of Lisi, Marrone and Montanino [80] and Benatti and Floreanini [81], with also almost simultaneous works. Since then, many authors carried out phenomenological discussions on the subject using neutrino mixing. An important remark in our terminology here is that we will denote such effects as *quantum decoherence* (QD) from now on, since it is a term mostly spread by the neutrino community, despite,

as we will see, decoherence, or the damping in the neutrino oscillation probability, is not the single effect of quantum decoherence.

It is worth emphasizing that in this thesis, we limit ourselves to phenomenological discussions of the implications related to the subject of pure neutrino states being induced into mixed ones. This is motivated by the fact that the microscopic details of quantum gravity in quantum fields or quantum mechanics are simply not fully understood. Even though, we will try to elucidate that a phenomenological approach to investigate open quantum systems in neutrinos is a powerful tool to test, indirectly, if neutrinos could be affected by this (or any other) exotic physics that extends quantum mechanics to be open in nature.

6.1 Open quantum systems and the evolution equation

In Chapter 2, we introduced the neutrino oscillation in vacuum through the Liouville-von Neumann evolution equation for the neutrino density matrix ρ. If the quantum system is considered open, (2.5) no longer provides a reasonable formulation of the evolution and additional statements should be formulated in order to accomplish a more general equation of motion, which is the GKSL equation [76, 77]. The first one is that we model the neutrino as in contact with a larger system, which is commonly associated with a thermal bath, with an infinite number of degrees of freedom, we denote this larger system as an environment. In this case, the total density matrix can be written as the product $\rho = \rho_S \otimes \rho_E$, with the fundamental assumption of no correlations in the initial time in the propagation, where ρ_S is the density matrix of the neutrino subsystem and ρ_E a reference state of the environment. To get $\rho_S(t)$, we need to trace out the total system over the environment:

$$\rho_S(t) = \mathrm{Tr}_E[\Lambda(t)\rho] = \mathrm{Tr}_E[U(t)\rho_S \otimes \rho_E U^\dagger(t)] \ , \tag{6.1}$$

with the derivation of an equation of motion for ρ_S is all about finding a family of time-evolution operators $\{\Lambda(t)\}$ that enable to have $\rho_S(t) = \Lambda(t)\rho_S$. This "super-operator" (in the sense of operating in ordinary operators) is denoted as a dynamical map and $\{\Lambda(t)\}$ is a quantum dynamical semi-group with generator $\mathcal{L}$, sometimes regarded as generalized Liouville super-operator [82]. Using these concepts and removing the S index of the neutrino density matrix, i.e. $\rho_S \to \rho$ for simplicity of notation (still having in mind that the neutrino concerns a subsystem), we can derive the GKSL equation for a N-level quantum subsystem as [77]

$$\frac{d\rho}{dt} = -i[H,\rho] + \sum_{p=1}^{N^2-1}\left(V_p\rho V_p^\dagger - \frac{1}{2}\{V_p^\dagger V_p,\rho\}\right) \ , \tag{6.2}$$

where it is possible to see a Hamiltonian term, corresponding to the conventional evolution in quantum mechanics and an additional term, with a new quantity V_p that we denote as jump operators, with the non-Hamiltonian term (second term in the r.h.s) commonly called dissipation part of the evolution. Writing (6.2) in a more compact way:

$$\frac{d\rho}{dt} = -i[H, \rho] + \mathcal{D}(\rho) \ , \tag{6.3}$$

with

$$\mathcal{D}(\rho) = \sum_{p=1}^{N^2-1} \left(V_p \rho V_p^\dagger - \frac{1}{2}\{V_p^\dagger V_p, \rho\} \right) = \frac{1}{2} \sum_{p=1}^{N^2-1} ([V_p, \rho V_p^\dagger] + [V_p \rho, V_p^\dagger]) \ . \tag{6.4}$$

A more complete derivation of this equation of motion can be found in Appendix A.

It is worth mentioning that we require an additional physical assumption for (6.4), which is the increase of von Neumann entropy $S(\rho) = -\operatorname{Tr}(\rho \ln \rho)$ at all times. It can be fulfilled by making $V_p = V_p^\dagger$ and the derivation of this property can be found in [83]. Applying this assumption, eq. (6.4) is simplified to

$$\mathcal{D}(\rho) = \frac{1}{2} \sum_{p=1}^{N^2-1} [[V_p, \rho], V_p] \ . \tag{6.5}$$

Another important remark concerning the equation of motion arises from the question: if the quantum system is modeled from a subsystem in contact with the corresponding thermal bath, is some exchange of energy between both allowed in the propagation? The answer is yes if the neutrino Hamiltonian does not commute with the jump operator, i.e. $[H, V_p] \neq 0$ [70, 71].

There are a number of approaches to solving the equation (6.3). We adopt a simple one, which is the expansion of all operators in the generators of SU(N), with N as the number of levels of the system, i.e. for two neutrinos, $N = 2$. We devote the rest of this chapter to solving the equation of motion in (6.3) for two and three neutrino systems in vacuum and see the implications of considering a dissipation effect in quantum mechanics. In the next chapter, we can include in this framework the ν-matter interaction in order to apply these achievements in the supernova environment.

6.2 Two-level system in vacuum

Our goal in this section is to solve the evolution equation for a 2-ν system, considering a particular case of ν_e created and detected in vacuum. The quantity we are interested in is the survival probability P_{ee} as in previous chapters. Firstly, we can expand the operators

in the neutrino mass basis with Pauli matrices as

$$\begin{aligned} H &= h_\mu \sigma_\mu = h_0 + \sum_{i=1}^{3} h_i \sigma_i \\ \rho &= \rho_\mu \sigma_\mu = \rho_0 + \sum_{j=1}^{3} \rho_j \sigma_j \\ V_p &= v_{p\mu} \sigma_\mu = v_{p0} + \sum_{k=1}^{3} v_{pk} \sigma_k \end{aligned} \quad , \tag{6.6}$$

and make the substitution in eq. (6.2),

$$\begin{aligned} \frac{d}{dt}\rho_\mu \sigma_\mu &= -i \sum_{i,j=1}^{3} h_i \rho_j [\sigma_i, \sigma_j] + \frac{1}{2} \sum_{p,i,j,k=1}^{3} v_{pi} \rho_j v_{pk} [[\sigma_i, \sigma_j], \sigma_k] \\ \frac{d}{dt}\rho_\mu \sigma_\mu &= 2 \sum_{i,j,k} \epsilon_{ijk} h_i \rho_j \sigma_k - 2 \sum_{p,i,j} (v_{pi}^2 \rho_j \sigma_j - v_{pi} v_{pj} \rho_j \sigma_i) \end{aligned} \quad , \tag{6.7}$$

where μ ranges from 0 to 3 and i, j from 1 to 3. It is straightforward to note that equation (6.7) is a set of coupled equations with expanded coefficients of initial operators. If we perform the above sum, we have

$$\begin{aligned} \frac{d}{dt}\rho_\mu \sigma_\mu = 2 &\left[(h_2\rho_3 - h_3\rho_2)\sigma_1 + (h_3\rho_1 - h_1\rho_3)\sigma_2 + (h_1\rho_2 - h_2\rho_1)\sigma_3 \right] \\ -2\big[&(\mathbf{v}_2^2\rho_1 + \mathbf{v}_3^2\rho_1 - \mathbf{v}_1\mathbf{v}_2\rho_2 - \mathbf{v}_1\mathbf{v}_3\rho_3)\sigma_1 \\ &+ (\mathbf{v}_1^2\rho_2 + \mathbf{v}_3^2\rho_2 - \mathbf{v}_1\mathbf{v}_2\rho_1 - \mathbf{v}_2\mathbf{v}_3\rho_3)\sigma_2 \\ &+ (\mathbf{v}_1^2\rho_3 + \mathbf{v}_2^2\rho_3 - \mathbf{v}_1\mathbf{v}_3\rho_1 - \mathbf{v}_2\mathbf{v}_3\rho_2)\sigma_3 \big] \end{aligned} \quad , \tag{6.8}$$

where we simplified the sum over the p index as $\mathbf{v}_\mu = \sum_{p=1}^{3} v_{p_\mu}$ with no loss of generality. It is convenient to rewrite eq. (6.8) to use the coefficients of the density matrix in a vector form $(\boldsymbol{\rho})^T = (\rho_0, \rho_1, \rho_2, \rho_3)$, changing eq. (6.8) to

$$\dot{\boldsymbol{\rho}} = -2\mathcal{L}\boldsymbol{\rho} \ , \tag{6.9}$$

with

$$\mathcal{L} = H_{\mu\nu} + D_{\mu\nu} \tag{6.10}$$

being the Liouville super-operator. This vectorized form of the density matrix in the equation of motion is referred to as Liouville space in the literature [84, 85]. Recall that in the SU(2) expansion one simply could make $\mathcal{D}(\rho) = \mathcal{D}(\rho)_\mu \sigma^\mu = D_{\mu\nu}\rho^\nu \sigma^\mu$, to get the dissipation part $D_{\mu\nu}$, that in matrix form is given by

$$D_{\mu\nu} = \begin{pmatrix} 0 & 0 & 0 & 0 \\ 0 & \mathbf{v}_2^2 + \mathbf{v}_3^2 & -\mathbf{v}_1\mathbf{v}_2 & -\mathbf{v}_1\mathbf{v}_3 \\ 0 & -\mathbf{v}_1\mathbf{v}_2 & \mathbf{v}_1^2 + \mathbf{v}_3^2 & -\mathbf{v}_2\mathbf{v}_3 \\ 0 & -\mathbf{v}_1\mathbf{v}_3 & -\mathbf{v}_2\mathbf{v}_3 & \mathbf{v}_1^2 + \mathbf{v}_2^2 \end{pmatrix} , \tag{6.11}$$

as well as the Hamiltonian term is written as

$$H_{\mu\nu} = \begin{pmatrix} 0 & 0 & 0 & 0 \\ 0 & 0 & h_3 & -h_2 \\ 0 & -h_3 & 0 & h_1 \\ 0 & h_2 & -h_1 & 0 \end{pmatrix} . \tag{6.12}$$

Note that (6.11) is a symmetric matrix whereas (6.12) is antisymmetric and both are hermitian. Equation (6.11) can be parameterized as

$$D_{\mu\nu} = \begin{pmatrix} 0 & 0 & 0 & 0 \\ 0 & a & b & c \\ 0 & b & \alpha & \beta \\ 0 & c & \beta & \gamma \end{pmatrix} , \tag{6.13}$$

with

$$\begin{aligned} a &= v_2^2 + v_3^2 \qquad & \alpha &= v_1^2 + v_3^2 \\ b &= -v_1 v_2 \qquad & \beta &= -v_2 v_3 \\ c &= -v_1 v_3 \qquad & \gamma &= v_1^2 + v_2^2 \end{aligned} , \tag{6.14}$$

and in order to preserve a strong requirement of open quantum systems formalism, the *complete positivity* of the density matrix, these parameters should respect the inequalities [81]

$$\begin{aligned} 2R &\equiv \alpha + \gamma - a \geqslant 0 \\ 2S &\equiv a + \gamma - \alpha \geqslant 0 \\ 2T &\equiv a + \alpha - \gamma \geqslant 0 \end{aligned} \qquad \begin{aligned} &RS - b^2 \geqslant 0 \\ &RT - c^2 \geqslant 0 \\ &ST - \beta^2 \geqslant 0 \\ &RST - 2bc\beta - R\beta^2 - Sc^2 - Tb^2 \geqslant 0 \end{aligned} , \tag{6.15}$$

in order to make the evolution to positive density matrices at all times. A remark about (6.13) is that we do not know its form from the first principles.

To understand the impact of the dissipation term in the neutrino evolution and avoid managing with the nine additional parameters, we will solve the special case of the following diagonal dissipation matrix

$$D_{\mu\nu} = \begin{pmatrix} 0 & 0 & 0 & 0 \\ 0 & \gamma & 0 & 0 \\ 0 & 0 & \gamma & 0 \\ 0 & 0 & 0 & \gamma \end{pmatrix} . \tag{6.16}$$

The mass basis Hamiltonian in Liouville space is given by

$$H_{\mu\nu} = \begin{pmatrix} 0 & 0 & 0 & 0 \\ 0 & 0 & \frac{\omega}{2} & 0 \\ 0 & -\frac{\omega}{2} & 0 & 0 \\ 0 & 0 & 0 & 0 \end{pmatrix} , \tag{6.17}$$

where we can recall that $\omega = \frac{\Delta m^2_{21}}{2E}$. The resulting set of coupled equations becomes

$$\begin{aligned} \dot{\rho}_0(t) &= 0 \\ \dot{\rho}_1(t) &= -2\gamma\rho_1(t) - \omega\rho_2(t) \\ \dot{\rho}_2(t) &= \omega\rho_1(t) - 2\gamma\rho_2(t) \\ \dot{\rho}_3(t) &= -2\gamma\rho_3(t) \end{aligned} , \tag{6.18}$$

with the solution given by

$$\begin{aligned} \rho_0(t) &= \rho_0 \\ \rho_1(t) &= e^{-2\gamma t}\left[\rho_1 \cos\omega t - \rho_2 \sin\omega t\right] \\ \rho_2(t) &= e^{-2\gamma t}\left[\rho_2 \cos\omega t + \rho_1 \sin\omega t\right] \\ \rho_3(t) &= \rho_3 e^{-2\gamma t} \end{aligned} . \tag{6.19}$$

To find the survival probability of a ν_e generated and detected in vacuum, we use the initial density matrix in flavor basis $\rho_\alpha(0) = \mathrm{diag}(1, 0)$, and also recall the initial condition found in (2.14)

$$\rho(0) = U^\dagger \rho_\alpha(0) U = \begin{pmatrix} \cos^2\theta & \frac{\sin 2\theta}{2} \\ \frac{\sin 2\theta}{2} & \sin^2\theta \end{pmatrix} ,$$

where the density matrix on the mass basis becomes:

$$\rho(t) = \begin{pmatrix} \frac{1}{2} + \frac{e^{-2\gamma t}\cos 2\theta}{2} & \frac{e^{-2\gamma t}}{2}\sin 2\theta e^{-i\omega t} \\ \frac{e^{-2\gamma t}}{2}\sin 2\theta e^{i\omega t} & \frac{1}{2} - \frac{e^{-2\gamma t}\cos 2\theta}{2} \end{pmatrix} , \tag{6.20}$$

and, consequently, the density matrix in the flavor basis with the transformation $\rho_\alpha(t) = U\rho(t)U^\dagger$, to finally find the survival probability through $P_{ee} = \mathrm{Tr}\left[\rho_\alpha(0)\rho_\alpha(t)\right]$:

$$P_{ee}(t) = \frac{1}{2} + e^{-2\gamma t}\left[\frac{1}{2} - \sin^2 2\theta \sin^2\left(\frac{\omega t}{2}\right)\right] . \tag{6.21}$$

Equation (6.21) is consistent with our result for the expectation of the conventional quantum mechanical ν_e oscillation, since when $\gamma \to 0$, we recover the P_{ee} from (2.18). Note that in (6.21), we have an exponential term multiplying a constant as well as the oscillation term. So it is possible to infer that two effects are expected: one related to damping in the oscillation pattern where a system initially created coherently would lose

coherence along the propagation, and another one translating the average probability to a specific value, and surprisingly it is not any value but the fraction of one over the number of levels of the system, that is 1/2 for eq. (6.21). The latter is independent of the coherence in the creation: it potentially affects even systems with diagonal Hamiltonians. It is important to note that the relaxation effect appears only when we choose a $D_{\mu\nu}$ in which $[H, V_p] \neq 0$, i.e. some exchange of energy between the neutrino and environment is allowed, otherwise only decoherence effects would be possible. Different works [86, 87] provided a detailed description of such decoupled effects as decoherence and relaxation for the damping and the equipartition of states (or maximal mixing) respectively. The former effect will be important when we discuss the possible implications of this formalism in supernova neutrinos.

Note that we used the neutrino mass basis as the starting point of the equation of motion, and the literature also assumes the same procedure (see [81]). However, one could ask why the dissipation term can not be defined on flavor basis. It is not a discussed subject in the literature and we do not worry about this concept in this thesis for some reasons: the statement of neutrino dissipating energy or losing coherence in a basis with well-defined mass is a reasonable assumption; if we transform V_p operators to flavor basis, the dissipation matrix $D_{\mu\nu}$ would be affected by mixing angles, but the essential behavior provided by dissipative effects would be similar. Despite these assertions, we admit that it is a question to be better addressed in the literature in the future.

6.3 Three-level system in vacuum

For a three-neutrino system, we do a similar procedure of Section 6.2, but now we expand the operators in SU(3) using the Gell-Mann matrices λ_μ. After imposing the increase of von-Neumann entropy, the resulting dissipation matrix becomes

$$D_{\mu\nu} = -\begin{pmatrix} 0 & 0 & 0 & 0 & 0 & 0 & 0 & 0 & 0 \\ 0 & -\gamma_1 & \beta_{12} & \beta_{13} & \beta_{14} & \beta_{15} & \beta_{16} & \beta_{17} & \beta_{18} \\ 0 & \beta_{12} & -\gamma_2 & \beta_{23} & \beta_{24} & \beta_{25} & \beta_{26} & \beta_{27} & \beta_{28} \\ 0 & \beta_{13} & \beta_{23} & -\gamma_3 & \beta_{34} & \beta_{35} & \beta_{36} & \beta_{37} & \beta_{38} \\ 0 & \beta_{14} & \beta_{24} & \beta_{34} & -\gamma_4 & \beta_{45} & \beta_{46} & \beta_{47} & \beta_{48} \\ 0 & \beta_{15} & \beta_{25} & \beta_{35} & \beta_{45} & -\gamma_5 & \beta_{56} & \beta_{57} & \beta_{58} \\ 0 & \beta_{16} & \beta_{26} & \beta_{36} & \beta_{46} & \beta_{56} & -\gamma_6 & \beta_{67} & \beta_{68} \\ 0 & \beta_{17} & \beta_{27} & \beta_{37} & \beta_{47} & \beta_{57} & \beta_{67} & -\gamma_7 & \beta_{78} \\ 0 & \beta_{18} & \beta_{28} & \beta_{38} & \beta_{48} & \beta_{58} & \beta_{68} & \beta_{78} & -\gamma_8 \end{pmatrix}, \tag{6.22}$$

where we show in Appendix B each parameter in terms of V_p expansion coefficients.

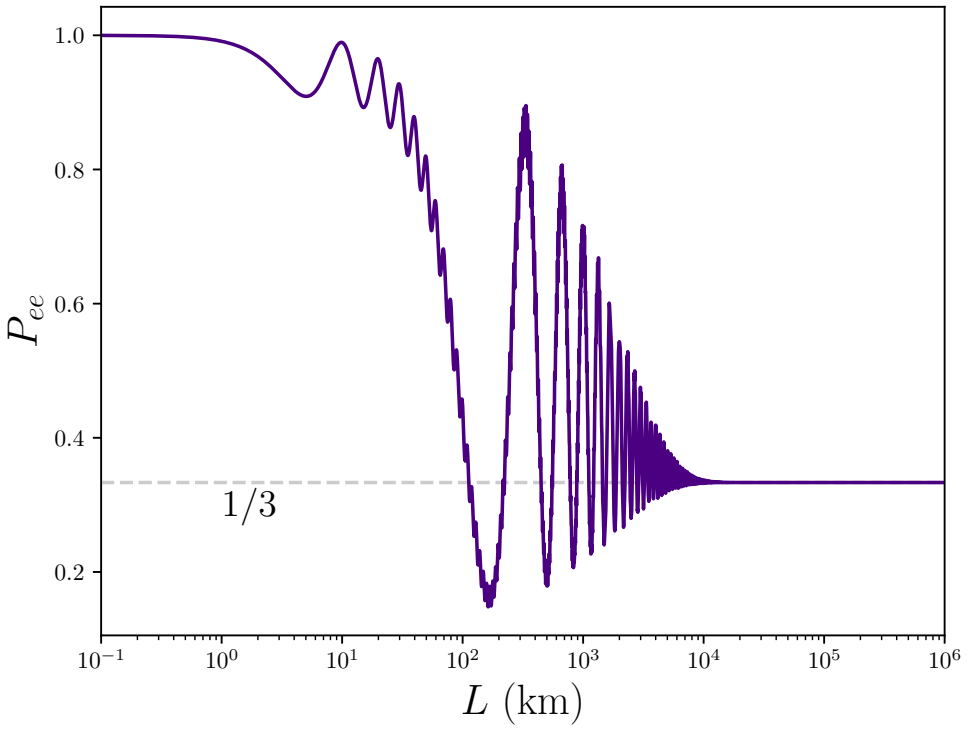

Figure 24 – Survival probability for ν_e propagating in vacuum in a distance L with quantum decoherence effects. The energy assumed was $E_\nu = 10$ MeV and we took $\Gamma = 10^{-13}$ eV. The neutrino is assumed to be ultra-relativistic, i.e. $v_\nu \approx c$.

As we can see, the equation of motion has 64 parameters when the dissipation part is considered. These parameters are also related to each other in order to guarantee the complete positivity of the evolution, with inequalities found in [88]. Considering all the above parameters is unmanageable and we also assume some simplification in order to check the possible effects in the neutrino evolution. Then, we take (6.22) to be diagonal, then $\beta_{\mu\nu} = 0$ for all μ, ν. We also let $\gamma_\mu = \Gamma$ for all μ, resulting in $D_{\mu\nu} = \text{diag}(0, \Gamma, \Gamma, \Gamma, \Gamma, \Gamma, \Gamma, \Gamma, \Gamma)$.

We can write the Hamiltonian in Liouville space on mass basis for three neutrinos as

$$H_{\mu\nu} = \begin{pmatrix} 0 & 0 & 0 & 0 & 0 & 0 & 0 & 0 & 0 \\ 0 & 0 & -\frac{\omega_{21}}{2} & 0 & 0 & 0 & 0 & 0 & 0 \\ 0 & \frac{\omega_{21}}{2} & 0 & 0 & 0 & 0 & 0 & 0 & 0 \\ 0 & 0 & 0 & 0 & 0 & 0 & 0 & 0 & 0 \\ 0 & 0 & 0 & 0 & 0 & -\frac{\omega_{31}}{2} & 0 & 0 & 0 \\ 0 & 0 & 0 & 0 & \frac{\omega_{31}}{2} & 0 & 0 & 0 & 0 \\ 0 & 0 & 0 & 0 & 0 & 0 & 0 & \frac{\omega_{21}}{2} - \frac{\omega_{31}}{2} & 0 \\ 0 & 0 & 0 & 0 & 0 & 0 & -\frac{\omega_{21}}{2} + \frac{\omega_{31}}{2} & 0 & 0 \\ 0 & 0 & 0 & 0 & 0 & 0 & 0 & 0 & 0 \end{pmatrix}, \tag{6.23}$$

with $\omega_{ij} = \Delta m_{ij}/2E$. Recall that we are interested in solving the evolution equation in (6.9), and $\mathcal{L} = H_{\mu\nu} + D_{\mu\nu}$. Using similar procedures as in the last section we can find the ν_e survival probability:

$$P_{ee} = \frac{1}{3} + Be^{-\Gamma t} + e^{-\Gamma t}[C\cos(\omega_{21}t - \omega_{31}t) + F\cos\omega_{21}t + G\cos\omega_{31}t] \ , \tag{6.24}$$

with

$$\begin{aligned} B &= \frac{2}{3}(c_{12}^4c_{13}^4 - c_{12}^2c_{13}^4s_{12}^2 - c_{12}^2c_{13}^2s_{13}^2 + c_{13}^4s_{12}^2 - c_{13}^2s_{12}^2s_{13}^2 + s_{13}^4) \\ C &= 2c_{13}^2s_{12}^2s_{13}^2 \\ F &= 2c_{12}^2c_{13}^4s_{12}^2 \\ G &= 2c_{12}^2c_{13}^2s_{13}^2 \end{aligned} \ ,$$

where c_{ij} and s_{ij} concern $\cos\theta_{ij}$ and $\sin\theta_{ij}$ respectively. As in the SU(2) solution, we can note that the exponential term $e^{-\Gamma t}$ multiplies the oscillation factors of (6.24), where we expect a damping in the oscillation probability, and in our terminology it is an effect of decoherence. The exponential multiplying the B constant is responsible for a relaxation of the system to the maximal mixing expectation for three neutrinos, i.e. 1/3. In Figure 24 we show the survival probability for ν_e considering the solution in (6.24). We see the combination of the damping in the oscillation (the amplitude decreases for larger distances), as well as the asymptotic value of P_{ee} asymmetrically goes to 1/3, given relaxation effects. We used a value of $\Gamma = 10^{-13}$ eV. It is worth mentioning that we could use neutrino experiments to test the behavior found in Figure 24. Actually, it is an effort already done for many neutrino sources, experiments, and works and the resulting bounds lead to excluding such a scenario with a certain confidence level (for this particular value of Γ and in the scale of energy used in Figure 24). In the next chapter, we will apply this formalism to the particular case of supernova neutrino emission and see its implications in a future neutrino detection as well as address how a future SN would potentially restrict these effects.

6.4 Three-level incoherent system

As discussed in Chapter 3 and Chapter 4, the neutrino coherence does not hold when the medium of propagation is high-density matter, since the neutrino Hamiltonian becomes approximately diagonal in this regime. In this section, we briefly show that even in this situation, quantum decoherence could affect neutrino mixing. To evaluate this effect, instead of using a matter potential to provide loss of coherence, we simply adopt

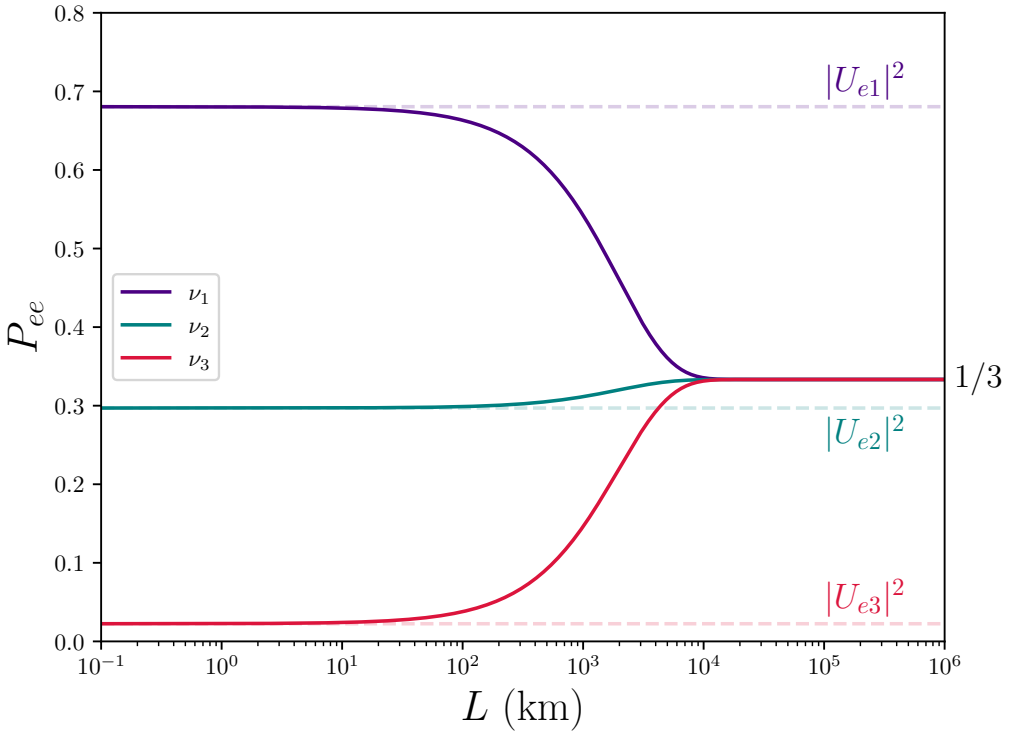

Figure 25 – Survival probability for ν_e propagating in vacuum in a distance L for an incoherent $\nu_e = \nu_i$, with $i = 1, 2, 3$. Each initial state is highlighted in the legend. The energy assumed was $E_\nu = 10$ MeV and we took $\Gamma = 10^{-13}$ eV.

the starting state to be incoherent in vacuum, i.e. $\nu_\alpha \approx \nu_i$. Let us take the example of an initial electron neutrino created as any mass state. Let us also use the same format of the dissipation matrix taken in the previous section, $D_{\mu\nu} = \text{diag}(0, \Gamma, \Gamma, \Gamma, \Gamma, \Gamma, \Gamma, \Gamma, \Gamma)$. The neutrino Hamiltonian in the mass state is also eq. (6.23). Solving the equation of motion (6.3), we get

$$\begin{aligned} P_{ee} &= \frac{1}{3} + e^{-\Gamma t}\left(c_{12}^2 c_{13}^2 - \frac{1}{3}\right) && \nu_e(0) = \nu_1 \\ P_{ee} &= \frac{1}{3} + e^{-\Gamma t}\left(s_{12}^2 c_{13}^2 - \frac{1}{3}\right) && \nu_e(0) = \nu_2 \ , \\ P_{ee} &= \frac{1}{3} + e^{-\Gamma t}\left(s_{13}^2 - \frac{1}{3}\right) && \nu_e(0) = \nu_3 \end{aligned} \tag{6.25}$$

where $\nu_e(0)$ means electron neutrino state in initial time $t_0 = 0$, i.e. $\rho_e(t = 0) = |\nu_i\rangle\langle\nu_i|$ for $i = 1, 2, 3$. It is worth mentioning that no interference term is present, but even for this incoherent initial neutrino state, quantum decoherence could impact neutrino mixing with relaxation. We note that for $\Gamma \to 0$ the $|U_{ei}|^2$ solution is recovered, which is the expected solution for P_{ee} considering an incoherent initial state. We also see that if $\Gamma \to \infty$, the maximal mixing 1/3 is reached. Figure 25 shows these probabilities as a function of propagated distance where an ultra-relativistic limit is taken, or $v_\nu \sim ct$. Note that the

same probability could be obtained using the factorization $P_{ee} = \sum_j P_{ei}P_{ij}P_{je}$, which will be crucial to the discussion in the next chapter. It is important to mention that QD effects are not expected in incoherent neutrinos when $[H, V_p] = 0$, since in this regime, relaxation effects are suppressed, and only decoherence would possibly occur[1].

Note that despite the fanciful scenario explored in this section, it fits very well with the situation of a neutrino created in a compact object with high-density matter and is emitted to vacuum, which is the exact supernova scenario and approximately what happens in stars, and it is an important issue that we address in SN context in Chapter 7.

[1] The additional assumption $[H, V_p] = 0$ would mean $D_{33} = D_{88} = 0$ in addition to rescaling other parameters.

Chapter 7

Quantum decoherence in supernova neutrinos

A large number of phenomenological studies designed to test if quantum decoherence could affect neutrino measurements were performed in the past, and no results indicate a strong signal of such an effect. However, neutrino detection data was able to impose strong bounds on this phenomenon, with analyzes performed in atmospheric [80, 89], accelerator [90, 91, 92, 93, 94, 88, 95, 96, 97], reactor [98, 97], solar [89, 99, 100], and ultra-high energy extra-terrestrial [101] neutrinos with different approaches, for past, operating, and future neutrino experiments. In this chapter, we include a new possible source to test quantum decoherence effects as well as eventually bound this phenomenon: **supernovas**. Although we do not claim the first worldwide work on the subject, since in 2010 the pre-print [102] suggests some analysis of the topic, we provide here the first analysis as complete as possible[1] in supernova neutrinos, and most of our results can be found in [103].

In the next section, we show the convenient models to be discussed here, making some choices concerning the already mentioned dissipation $D_{\mu\nu}$ matrix. Although we do not go into quantum gravity phenomenology, we guide our analysis through some definitions presented in the literature, particularly, the terminology and interesting ideas that connect possible quantum gravitational effects to open quantum systems formalism for neutrinos shown in [104].

7.1 Selected Models

We devote this section to connecting possible quantum decoherence models to different physical situations in a future SN detection. We decided to take only diagonal versions of (6.22) for simplicity, then $\beta_{\mu\omega} = 0$ for all μ and ω.

[1] As discussed in Chapter 4, many challenges are involved in a complete framework of SN-ν mixing.

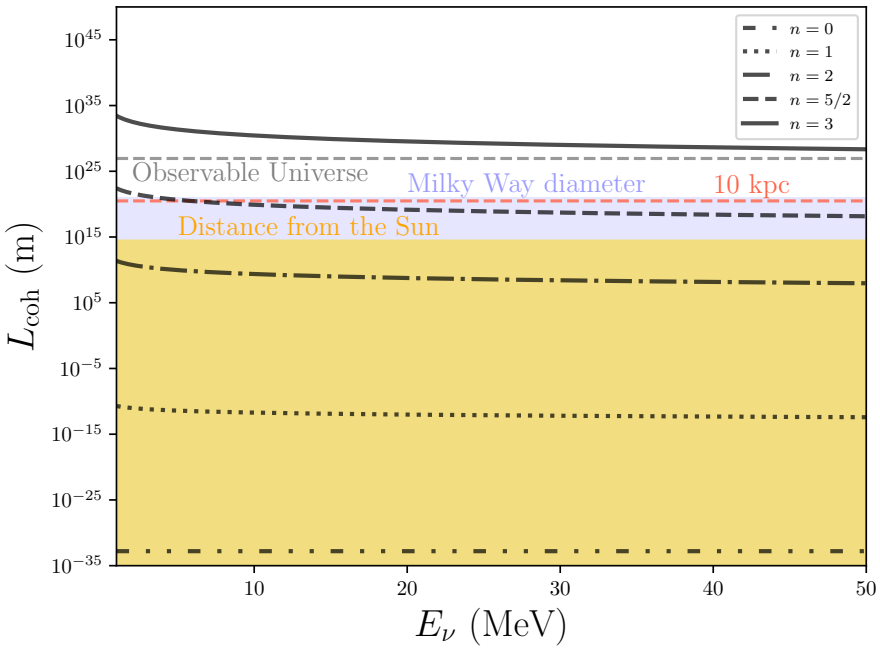

Figure 26 – Coherence length ($L_{\rm coh} = 1/\gamma$) for values of n in a power law of decoherence coefficients $\gamma = \gamma_0(E/E_0)^n$ for a "natural" scale of quantum gravity, with $\xi_{\rm Planck} = 1$. The region in yellow corresponds to the solar system edge, while the region in blue is the Milky Way diameter, and the dashed grey line is to respect the observable universe.

As discussed before, in works such as [105, 99] it is shown that quantum decoherence can give rise to two disentangled effects when the evolution occurs in vacuum: the pure decoherence, where a coherent state becomes incoherent along propagation; and the relaxation effect, responsible to lead the ensemble to a maximal mixing. As coherence on SN neutrinos is suppressed due to matter effects on the mixing angle and long propagation lengths[2], we do not expect pure decoherence effects to play any role in the propagation, being only (possibly) affected by relaxation.

Up to this date, and to the author's best knowledge, there is no consistent theory in which we can get the parameters of $D_{\mu\nu}$ from quantum gravity, or even if the parameters are constant. Different works [80, 106, 89, 104] suggested the possibility of a dependency on energy as $\gamma_i = \gamma_{0_i}(E/E_0)^n$ motivated by quantum space-time phenomenology, where E_0 is an arbitrary energy scale. In this work, we chose $E_0 = 10$ MeV to match the energy scale of supernova neutrinos. As for the energy dependence, we explore the scenarios with $n = 0$ and $n = 2$, given that most of the works check this power law exponents for γ_i, which enables us to compare SN limits to other sources (and works), and $n = 5/2$, well-motivated

[2] If neutrinos are only affected by MSW effect, it is possible for ν_μ and ν_τ oscillate to each other. It generally does not affect the analysis of flavor conversion, once they are indistinguishable in the detection, and therefore generally denoted as ν_x. However, as we will see in Section 7.2, their creation in coherent states changes one of the tested QD models here.

by the natural Planck scale for the SN energy range of $0 - 100$ MeV. By natural scale, we refer to $\gamma_{0_i} = \xi_{\rm Planck}/M^{n-1}_{\rm Planck}$ with $\xi_{\rm Planck} \sim 1$ [107, 104], making $\gamma_{0i} = \xi_{\rm Planck} M^{1}_{\rm Planck}$, $\xi_{\rm Planck} M^{-1}_{\rm Planck}$, and $\xi_{\rm Planck} M^{-3/2}_{\rm Planck}$ for our choices of $n = 0, 2$ and $5/2$.

With dimensional analysis (which can be further justified when solving the evolution equation), we expect that the effects of decoherence would show up for distances larger than a *coherence length*, defined by $L_{\rm coh} = 1/\gamma$. In Figure 26 we show the expected coherence length for these values of n. We see that if this "natural" scale holds, $n = 0$ and 2 would be possibly ruled out by terrestrial and solar experiments, whereas for $n = 3$, $L_{\rm coh}$ is out of the observable universe for the expected SN-ν energy scale. For the mentioned values of n, we analyze the following models:

Mass State Coupling (MSC): The neutrino mass basis is coupled to the environment and the relaxation effect leads to maximal mixing. In 3-ν mixing, it means a 1/3 (equal) probability of detecting any state. In this model, we test two possible scenarios related to energy conservation in the neutrino subsystem:

i) MSC$^{\not\epsilon}$ ($[H, V_p] = 0$): Here, the neutrino energy is conserved for any non-standard mixing process in vacuum[3]. It means that $V_p = \mathbf{v}_3\lambda_3 + \mathbf{v}_8\lambda_8$, where λ_μ are Gell-Mann matrices and $\mathbf{v}_\mu = \sum_{p=1}^{8} v_{p_\mu}$, with μ ranging from 0 to 8 in the SU(3) expansion of V_p. To simplify the analysis, we choose a diagonal version of the dissipation term in (6.22) with a single parameter Γ. Additionally, using complete positivity relations [88], we can find the special case of $D_{\mu\nu} = {\rm diag}(0, \Gamma, \Gamma, 0, \Gamma/4, \Gamma/4, \Gamma/4, \Gamma/4, 0)$, with $\Gamma = \Gamma_0(E/E_0)^n$. The transition probabilities amongst mass states in vacuum are null in this case. However, if we look at the propagation inside the supernova layers, in a diagonalized basis of the mass state in matter $P^{m({\rm SN})}_{ij}$, this probability could be non-null for $i \neq j$, i.e. transitions between ν_{im} and ν_{jm} are allowed and would change proportionally to $e^{-\Gamma}$. Therefore, the coherence length to be investigated is the SN radius, and the matter effects in addition to quantum decoherence would induce a maximal mixing inside the SN. In Figure 27 we show the transition probabilities of mass state in matter basis calculated using the slab approach with a simulated SN density profile from Garching group [40, 41], corresponding to a progenitor of 40 $M_\odot$, already shown in Figure 15. More details about our solution are in Appendix D. When the neutrino is released to vacuum, it is no longer affected by quantum decoherence until detection. Since the length traveled inside the Earth by the neutrino is much smaller than $L^{\rm SN}_{\rm coh}$, we do not take the quantum decoherence in Earth matter into account in this specific case, albeit standard non-adiabatic MSW effect could play a role. Note that this regime essentially depends on ν matter effects in the SN.

[3] In our notation, the superscript symbol $\not\epsilon$ accounts to no exchange of energy with the environment, while ϵ has the opposite meaning.

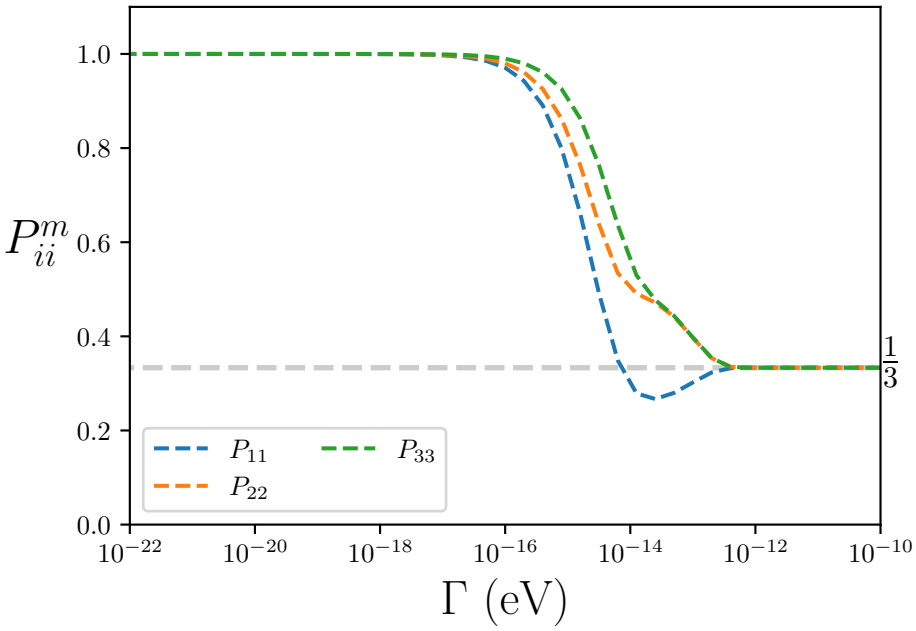

Figure 27 – Survival probabilities of mass state in matter basis inside the SN for the MSC$^{\not\epsilon}$ model (no exchange of energy from neutrinos and environment in vacuum) and $n = 0$ (and then $\Gamma = \Gamma_0$). The SN matter density profile used is from a Garching simulation of a 40 $M_\odot$ (LS180-s40.0) progenitor [40, 41], shown in Figure 15. The procedure to find these solutions is in Appendix D.

ii) MSC$^{\epsilon}$ ($[H, V_p] \neq 0$): In this model, we relax the above assumption, allowing some exchange of ν energy with the "non-standard" environment. We choose the most general diagonal version of the dissipation term from (6.22):

$$D_{\mu\nu} = \text{diag}(0, \gamma_1, \gamma_2, \gamma_3, \gamma_4, \gamma_5, \gamma_6, \gamma_7, \gamma_8) \ . \tag{7.1}$$

In [104], this choice of $D_{\mu\nu}$ is intrinsically related to *mass state selected* scenario to be impacted by quantum gravitational effects. To quantify the effects of this model, we solve (6.3) analytically to get the probabilities of interest in the mass basis in vacuum[4]:

$$\begin{aligned} P_{11} &= \frac{1}{3} + \frac{1}{2}e^{-\gamma_3 x} + \frac{1}{6}e^{-\gamma_8 x} \\ P_{12} &= \frac{1}{3} - \frac{1}{2}e^{-\gamma_3 x} + \frac{1}{6}e^{-\gamma_8 x} \\ P_{13} &= \frac{1}{3} - \frac{1}{3}e^{-\gamma_8 x} \\ P_{33} &= \frac{1}{3} + \frac{2}{3}e^{-\gamma_8 x} \end{aligned} \qquad \begin{aligned} P_{22} &= P_{11} \\ P_{23} &= P_{13} \end{aligned} \ , \tag{7.2}$$

[4] The expected (adiabatic MSW) solution for the probabilities is a Kronecker delta, i.e. $P_{ij} = \delta_{ij}$.

with x as the propagated distance. For other possible probabilities on this basis, we use $P_{ij} = P_{ji}$. It should be noted that on this basis the probabilities depend only on γ_3 and γ_8. The reason is that when solving the set of differential equations $\dot{\boldsymbol{\rho}} = -2\mathcal{L}\boldsymbol{\rho}$, the ones corresponding to γ_3 and γ_8, i.e. $\mathcal{L}_{3\nu}$ and $\mathcal{L}_{8\nu}$ are the only decoupled ones, independent of Hamiltonian terms.

If we look at γ_i parameters in terms of $\mathbf{v}_\mu$ coefficients of the SU(3) expanded V_p we find

$$\begin{aligned} \gamma_3 &= \mathbf{v}_1^2 + \mathbf{v}_2^2 + \frac{\mathbf{v}_4^2}{4} + \frac{\mathbf{v}_5^2}{4} + \frac{\mathbf{v}_6^2}{4} + \frac{\mathbf{v}_7^2}{4} \\ \gamma_8 &= \frac{3\mathbf{v}_4^2}{4} + \frac{3\mathbf{v}_5^2}{4} + \frac{3\mathbf{v}_6^2}{4} + \frac{3\mathbf{v}_7^2}{4} \end{aligned} \quad . \tag{7.3}$$

Equation (7.3) shows that γ_3 and γ_8 are not independent. In order to compare our results to solar neutrinos [99], we can use the same notation to define:

$$\begin{aligned} \Gamma_3 &= \mathbf{v}_1^2 + \mathbf{v}_2^2 \\ \Gamma_8 &= \frac{3\mathbf{v}_4^2}{4} + \frac{3\mathbf{v}_5^2}{4} + \frac{3\mathbf{v}_6^2}{4} + \frac{3\mathbf{v}_7^2}{4} \end{aligned} \quad , \tag{7.4}$$

leading to $\gamma_3 = \Gamma_3 + \Gamma_8/3$ and $\gamma_8 = \Gamma_8$, resulting in pure (independent) relaxation Γ_i parameters, that will be the ones effectively inducing the maximal admixture in this scenario. The energy dependence is explicitly written as $\Gamma_i = \Gamma_{0i}(E/E_0)^n$ with $i = \{3, 8\}$. Note that the effective distance of this particular case is the total neutrino propagation, i.e. vacuum propagation is also affected and it can be split into the regime in the SN and outside its surface until Earth, or $L = L^{\rm SN} + L^{\rm Vac}$. Similarly as in i), we solve the probabilities associated with possible transitions in supernova layers only numerically. However, as we discuss in Section 7.2.1, given that $L^{\rm Vac} \gg L^{\rm SN}$, the approximation of $L \sim L^{\rm Vac}$ is assumed in our calculations.

Neutrino Loss: As mentioned in [104], it is possible to have a scenario with neutrino loss, where neutrinos are captured by effects of quantum gravity during propagation, and re-emitted to a different direction, never reaching the detector at Earth. In this picture, the authors made a choice of $D_{00} \neq 0$. Looking at the most general form of $\mathcal{D}(\rho)$, it is possible to say that this choice is completely out of open quantum systems formalism, i.e. naturally $\mathcal{D}(\rho)_{0\mu} = 0$ when the master equation (6.3) is assumed to describe the evolution of the reduced quantum system, with trace-preserving all times. Even though, to explore such an interesting physical situation, we test this non-unitary case that matches the choice $\gamma_i = \gamma$ with i from 1 to 8, then $D_{\mu\nu} = \mathrm{diag}(\gamma, \gamma, \gamma, \gamma, \gamma, \gamma, \gamma, \gamma, \gamma)$, with $\gamma = \gamma_0(E/E_0)^n$. The solution of (6.3) gives:

$$\begin{aligned} P_{ii} &= e^{-\gamma x} \\ P_{ij} &= 0 \end{aligned} \tag{7.5}$$

for any i, j from 1 to 3 with $i \neq j$. Note that in this result, in contradiction to conventional unitary models, one state does not go to another, i.e. $\sum_i P_{ij} \neq 1$, once neutrinos are lost along the way.

In the solutions of the equation of motion shown above, we absorbed a factor of 2 in the quantum decoherence parameters, i.e. $2\gamma_i \to \gamma_i$, with no loss of generality, since what matters in our results is the intensity of a deviation from a standard scenario.

It is important to mention that we tested a non-diagonal version of $D_{\mu\nu}$ using complete positivity relations and the asymptotic results were also the maximal mixing, with behavior similar to that presented here. We report this non-diagonal model in Appendix C.

7.2 Methodology and simulation

To test the QD models discussed in the context of a future SN detection, we use the neutrino flux coming from supernovae simulations from the Garching group [40]. For MSC$^{\not\epsilon}$ described in item *i*) of MSC in Section 7.1, we exploit a 40 $M_\odot$ progenitor simulation (LS180-s40.0) [41], since it has detailed matter density profiles, essential to explore such scenario. For all other cases investigated (MSC$^{\epsilon}$ and ν-loss), we use simulations with 27 $M_\odot$ (LS220s27.0c) and 11.2 $M_\odot$ (LS220s11.2c) progenitor stars, detailed in [39].

To avoid the large uncertainties of collective effects, we only use the flux from the neutronization burst phase (first 30 ms) in our analysis, in which effects induced by $\nu - \nu$ interaction are expected to not play a significant role. In Figure 28 we show the luminosity of all flavors along the time window of this phase.

Next, we explain in more detail how to include non-standard physics of eqs. (7.2) and (7.5) in SN neutrino evolution and our methods to use a future SN detection to impose limits on QD parameters.

7.2.1 Factorization of the dynamics

This analysis only takes into account the MSW effect in the neutronization burst through the standard matter effect on ν mixing in addition to quantum decoherence effects. To combine QD effects and MSW along the ν generation, propagation, crossing through

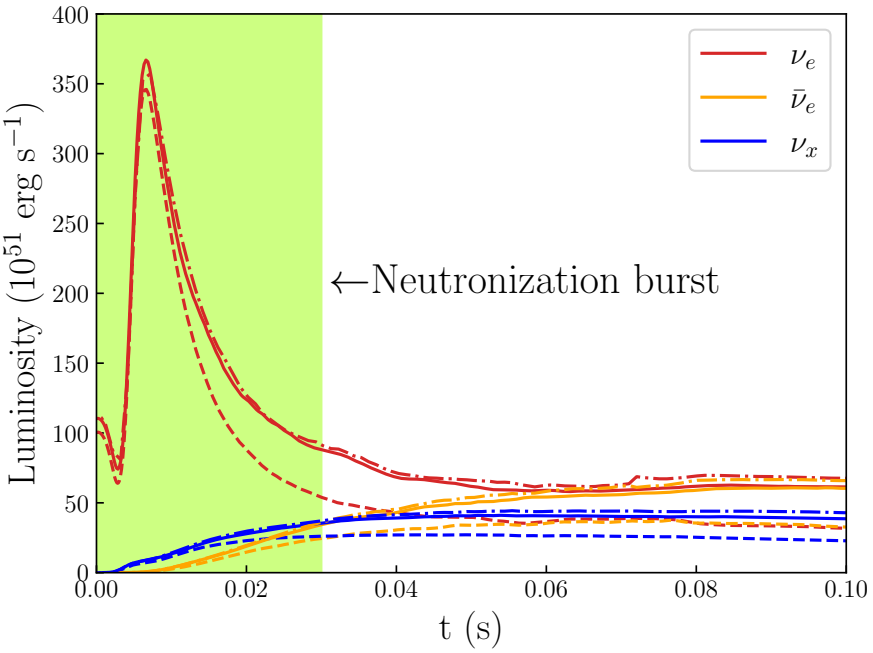

Figure 28 – Simulated ν luminosity for neutronization burst phase of the emission models of 27 $M_\odot$ (solid) and 11.2 $M_\odot$ (dashed) progenitor stars from Garching group [40, 39].

Earth, and detection, it is possible to factorize the flavor probabilities as

$$P_{\alpha\beta} = \sum_{i,j,k=1}^{3} P_{\alpha i}^{m(\mathrm{SN})} P_{ij}^{m(\mathrm{SN})} P_{jk} P_{k\beta}^{m(\mathrm{Earth})} \qquad \bar{P}_{\alpha\beta} = \sum_{i,j,k=1}^{3} \bar{P}_{\alpha i}^{m(\mathrm{SN})} \bar{P}_{ij}^{m(\mathrm{SN})} \bar{P}_{jk} \bar{P}_{k\beta}^{m(\mathrm{Earth})} \,, \tag{7.6}$$

where $P_{\alpha\beta}$ and $\bar{P}_{\alpha\beta}$ are the transition probabilities from flavor α to β for neutrinos and antineutrinos. The meaning of each term in (7.6) can be summarized as: $P_{\alpha i}^{m(\mathrm{SN})}$ is the probability of creating a ν_α as a i state in matter ν_{im}; $P_{ij}^{m(\mathrm{SN})}$ is the probability of converting $\nu_{im} \to \nu_{jm}$ inside supernova layers; P_{jk} the probability of converting $\nu_j \to \nu_k$ during propagation in vacuum until Earth; and by the end, $P_{k\beta}^{m(\mathrm{Earth})}$ is the probability of detecting a ν_β given a ν_k state considering (or not) Earth matter effects. Where, again, the index m regards that the creation or propagation is in matter. It is worth remembering that ν_e and $\bar{\nu}_e$ are created as a single mass eigenstate in matter. In this scenario, the sum over i vanishes, since we have $P_{ei}^{m(\mathrm{SN})} = \delta_{i3}$ and $\bar{P}_{ei}^{m(\mathrm{SN})} = \delta_{i1}$ for NH, and $P_{ei}^{m(\mathrm{SN})} = \delta_{i2}$ and $\bar{P}_{ei}^{m(\mathrm{SN})} = \delta_{i3}$ for IH. As for ν_x, although it is created in a coherent superposition of the other two mass eigenstates, the interference phase would be averaged out, and therefore eq. (7.6) is valid. In the context of a SN flux conservation, the simplest flavor conversion scheme could be described by just P_{ee} and $\bar{P}_{ee}$, and in standard neutrino mixing, the factorized probabilities in (7.6) become $P_{ij}^{m(\mathrm{SN})} = \delta_{ij}$, $P_{jk} = \delta_{jk}$ and $\bar{P}_{ij}^{m(\mathrm{SN})} = \delta_{ij}$, $\bar{P}_{jk} = \delta_{jk}$ for adiabatic evolution. Such a scenario can be changed by quantum decoherence, allowing

for the conversion among mass eigenstates in vacuum and matter. The explicit solutions for the equation (7.6) in NH and IH can be written as:

$$\begin{aligned} P_{ee}^{\rm NH} &= \frac{1}{3} + e^{-\Gamma_8 t}\left(s_{13}^2 - \frac{1}{3}\right) \\ P_{ee}^{\rm IH} &= \frac{1}{3} + \frac{c_{12}^2 c_{13}^2}{2}\left[\frac{e^{-\Gamma_8 t}}{3} - e^{(\Gamma_3+\Gamma_8/3)t}\right] + \frac{c_{13}^2 s_{12}^2}{2}\left[\frac{e^{-\Gamma_8 t}}{3} + e^{(\Gamma_3+\Gamma_8/3)t}\right] - \frac{s_{13}^2}{3}e^{-\Gamma_8 t} \end{aligned} \tag{7.7}$$

and

$$\begin{aligned} \bar{P}_{ee}^{\rm NH} &= \frac{1}{3} + \frac{c_{12}^2 c_{13}^2}{2}\left[\frac{e^{-\Gamma_8 t}}{3} + e^{(\Gamma_3+\Gamma_8/3)t}\right] + \frac{c_{13}^2 s_{12}^2}{2}\left[\frac{e^{-\Gamma_8 t}}{3} - e^{(\Gamma_3+\Gamma_8/3)t}\right] - \frac{s_{13}^2}{3}e^{-\Gamma_8 t} \\ \bar{P}_{ee}^{\rm IH} &= \frac{1}{3} + e^{-\Gamma_8 t}\left(s_{13}^2 - \frac{1}{3}\right) \ . \end{aligned} \tag{7.8}$$

One can also note in (7.2), (7.3), (7.4) and (7.6) that for the MSC$^{\epsilon}$ model, P_{ee} is a function of Γ_3 and Γ_8 in IH but only of Γ_8 for NH. The $\bar{P}_{ee}$ has the opposite dependency and we can write:

$$\begin{aligned} P_{ee}^{\rm IH} &= P_{ee}^{\rm IH}(\Gamma_3, \Gamma_8) \qquad & P_{ee}^{\rm NH} &= P_{ee}^{\rm NH}(\Gamma_8) \\ \bar{P}_{ee}^{\rm IH} &= \bar{P}_{ee}^{\rm IH}(\Gamma_3) \qquad & \bar{P}_{ee}^{\rm NH} &= \bar{P}_{ee}^{\rm NH}(\Gamma_3, \Gamma_8). \end{aligned}$$

These remarks on the survival probabilities of ν_e and $\bar{\nu}_e$ are essential in our results, once the flavor conversion of MSC can be described using uniquely P_{ee} and $\bar{P}_{ee}$.

Particularly for the MSC$^{\not\epsilon}$ case, considering the propagation along supernova layers, $P_{ij}^{m(\rm SN)}$ and $\bar{P}_{ij}^{m(\rm SN)}$ will be affected by QD, nevertheless $P_{jk} = \delta_{jk}$ and $\bar{P}_{jk} = \delta_{jk}$, since with no exchange of energy to the environment, quantum decoherence would not play any role in the vacuum propagation. On the other hand, for MSC$^{\epsilon}$, both SN matter and vacuum would affect the neutrino mixing. However, as shown in Figure 48 in the Appendix D, it would be needed a $\Gamma_{3,8} \gtrsim 10^{-18}$ eV or even beyond to have significant changes over $P_{ij}^{m(\rm SN)}$. As it will be clear in Section 7.3, this value is much higher than the possible sensitivity of a future SN detection with only vacuum effects (given the large coherence length between the SN and Earth), then we take $P_{ij}^{m(\rm SN)}$ and $\bar{P}_{ij}^{m(\rm SN)}$ as δ_{ij} for MSC$^{\epsilon}$ from now on.

In order to put bounds on QD effects, we statistically analyze it in two scenarios: without Earth matter effects in neutrino (antineutrino) propagation, or $P_{ke}^{m(\rm Earth)} = P_{ke}$ ($\bar{P}_{ke}^{m(\rm Earth)} = \bar{P}_{ke}$) in (7.6); and then we check how Earth matter effects would impact our results.

Figure 29 shows both scenarios of P_{ee} and $\bar{P}_{ee}$ as a function of quantum decoherence parameters for neutrinos and antineutrinos, where neutrino hierarchy plays a relevant role in the considered scenarios. It is possible to see that Earth regeneration could enhance or decrease the sensitivity of standard physics on QD parameters for very specific energies

and zenith angles θ_z. However, as we will see later, regeneration becomes more relevant for higher energies, generally at the end of the SN-ν simulated spectrum, limiting its impact on SN flavor conversion.

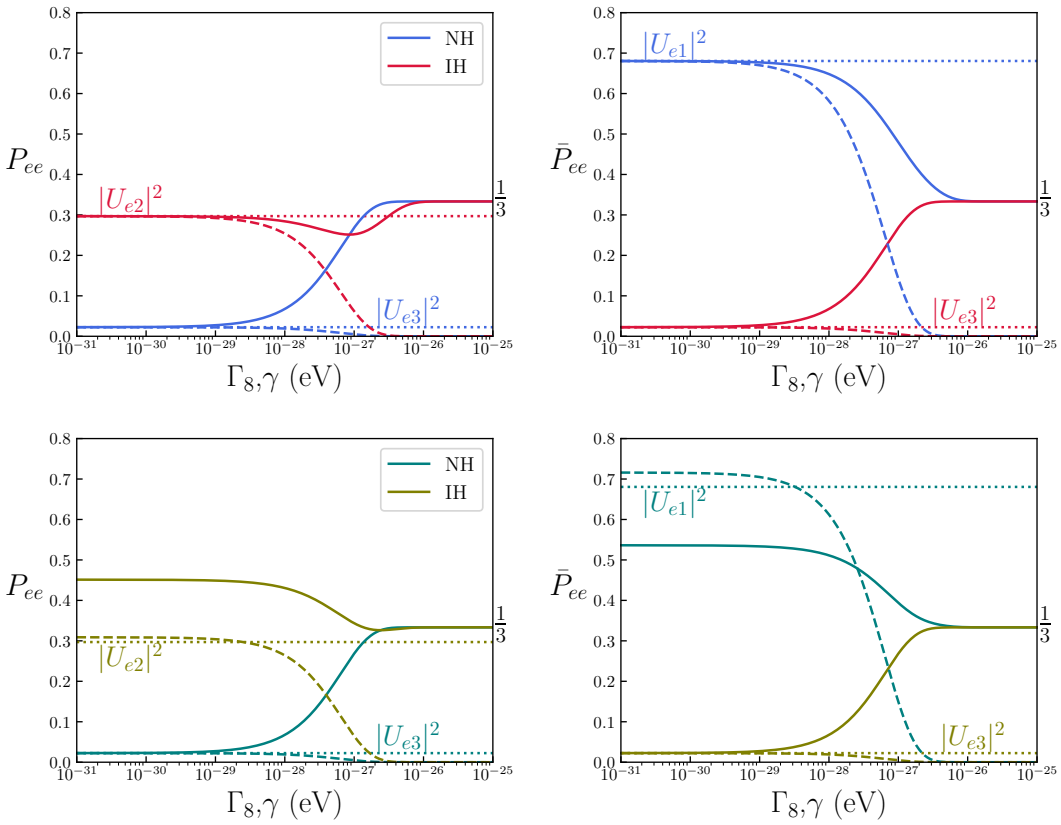

Figure 29 – Survival probability for electron neutrinos (left) and antineutrinos (right) as a function of decoherence parameters for $n = 0$ (energy independent) and a 10 kpc propagation, without (upper plots) and with (down plots) Earth matter effects. Solid lines represent MSC$^{\epsilon}$ scenario (Γ_8) with $\Gamma_3 = 10^{-27}$ eV and the dashed, the neutrino loss (γ). For the upper plots, quantum decoherence is taken into account only in vacuum in between SN surface until detection at Earth, with no regeneration considered. In the down ones, we set the zenith angle of $\theta_z = 180^o$ and $E_\nu = 30$ MeV.

It is worth mentioning that for the MSC model, asymptotically we expect more sensitivity on P_{ee} in NH than IH, since for IH the standard probability is about the maximal admixture (1/3). In contrast, for $\bar{P}_{ee}$, both hierarchy scenarios are almost equally sensitive to a maximal admixture scenario. In the case of ν-loss we see the opposite picture for P_{ee}, i.e. IH would be more impacted by an asymptotically null probability, and for $\bar{P}_{ee}$ NH would be highly affected, with low impact on IH.

As we will see later, the most general scheme of SN-ν fluxes at Earth can not be parameterized with just P_{ee} and $\bar{P}_{ee}$ for the ν-loss scenario, given no conservation of total flux. Therefore it is needed to work out $P_{\alpha\beta}$ also for $\alpha, \beta = \mu, \tau$ (not shown in Figures 29 for simplicity). We clarify it in the next section.

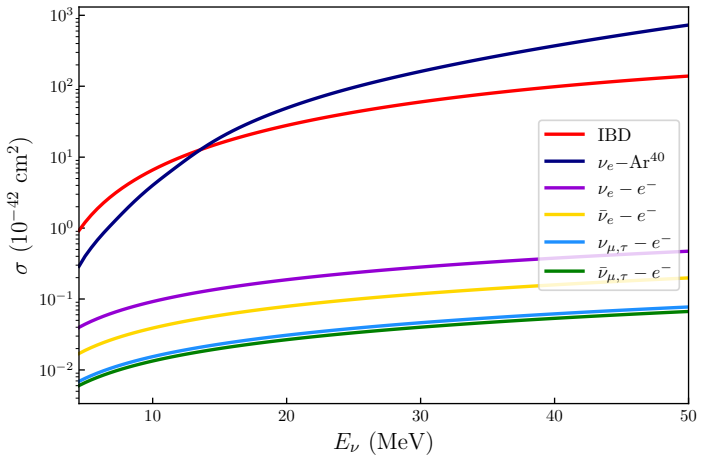

Figure 30 – ν total cross-sections for inverse beta decay (IBD) [55], ν_e–Ar charge current interaction (from SNOwGLoBES) [108] and elastic $\nu - e^-$ interaction [109].

7.2.2 Exploring a future SN-ν detection

Since the detection of SN1987A through neutrinos, a galactic SN is expected by the community as a powerful natural ν laboratory, and the next generation of neutrino detectors promises a precise measurement of a galactic SN, highly increasing our knowledge of SN-ν flavor conversion, with different detector technologies and capabilities. Here, we show the sensitivity of DUNE, HK, and JUNO on QD. These detectors have the following properties:

a) DUNE will be a 40 kt Liquid-Argon TPC in the USA. We consider only the most promising detection channel $\nu_e + \mathrm{Ar} \rightarrow e^- + K^+$ [110] in our analysis, being sensitive to electron neutrinos and consequently to most neutronization burst flux[5]. We set an energy threshold to $E_{\mathrm{th}} = 4.5$ MeV and use the most conservative reconstruction efficiency reported in [110].

b) Hyper-Kamiokande will be a water Cherenkov detector in Japan with a fiducial mass of ~ 374 kt with main detector channel as the inverse beta decay (IBD), sensible to electron antineutrinos: $\bar{\nu}_e + p \rightarrow e^+ + n$. It is also expected hundreds of events from elastic scattering with electrons, with the advantage of sensitivity to all flavors: $\nu + e^- \rightarrow \nu + e^-$. We consider both channels in our analysis. We set a 60% overall detector efficiency and $E_{\mathrm{th}} = 3$ MeV.

c) JUNO will be a liquid scintillator detector with a fiducial mass of 17 kt situated in China [17]. Despite the interesting multi-channel detection technology reported by the collaboration, we take into account only IBD events. We set an overall efficiency of 50% and $E_{\mathrm{th}} = 3$ MeV in our analysis.

[5] Actually, it depends on the neutrino mass hierarchy, once for MSW-NH the ν_e flux is highly suppressed.

In order to compare the examined scenarios, we will consider only the energy information, calculating the number of events in the j-th energy bin as

$$N_j = n_d^c \int_0^\infty dt \int_0^\infty dE_\nu \frac{d^2\phi_\nu}{dt dE_\nu} \eta(E_\nu) \int_{E_i}^{E_f} dE_{\rm det} R_j(E_{\rm det}, E_\nu) \sigma(E_\nu) \ , \tag{7.9}$$

where n_d^c is the number of targets for each detector d, with c accounting for each specific channel, ϕ_ν is the neutrino flux, $\eta(E_\nu)$ is the efficiency that can eventually depend on ν energy, σ is the neutrino cross-section (with each channel shown in Figure 30), R_j is the detector resolution, as a function of the true (E_ν) and detected ($E_{\rm det}$) particle energies. We analyze the ν energy from the threshold of each detector up to 60 MeV. The ν mixing is encoded in the flux ϕ_{ν_β}, that can be parameterized as (4.13), that we recall here:

$$\begin{aligned}
\phi_{\nu_e} &= \phi^0_{\nu_e} P_{ee} + \phi^0_{\nu_x}(1 - P_{ee}) \\
\phi_{\bar{\nu}_e} &= \phi^0_{\bar{\nu}_e} \bar{P}_{ee} + \phi^0_{\nu_x}(1 - \bar{P}_{ee}) \\
\phi_{\nu_x} &= \phi^0_{\nu_e}(1 - P_{ee}) + \phi^0_{\nu_x}(2 + P_{ee} + \bar{P}_{ee}) + \phi^0_{\bar{\nu}_e}(1 - \bar{P}_{ee})
\end{aligned}$$

for the standard MSW (widely found in literature, see Chapter 4 or [111, 39] for a review), where $\phi^0_{\nu_\beta}$ refers to initial SN neutrino fluxes and non-standard QD effects are hidden in P_{ee} and $\bar{P}_{ee}$. In the case of modern simulations, the fluxes are given by a specific parameterization proposed in [112]:

$$\phi^0_{\nu_\beta}(t, E_\nu) = \left[\frac{E_\nu}{\langle E_\nu \rangle(t)}\right]^{\alpha(t)} e^{-[\alpha(t)+1]E_\nu/\langle E_\nu\rangle(t)} \ , \tag{7.10}$$

where $\langle E_\nu \rangle(t)$ is the neutrino mean energy and $\alpha(t)$ is denoted as a pinching parameter and enables the distribution to fit better the high-energy tail of the distribution than a conventional Fermi-Dirac spectrum [39]. Both parameters change with the time evolution of the SN. Note that one should not confuse the pinching α with the index used in flavor probabilities in previous equations. This pinching parameter is given by [112, 39]:

$$\frac{\langle E_\nu^2 \rangle(t)}{\langle E_\nu \rangle^2(t)} = \frac{2 + \alpha(t)}{1 + \alpha(t)} \ , \tag{7.11}$$

where $\langle E_\nu \rangle(t)$ and $\langle E_\nu^2 \rangle(t)$ are outputs of used simulations. Although the time dependency of simulated parameters, in our analysis, we use only the time-integrated flux for simplicity, i.e. we do not bin the spectrum of events in time as shown in equation (7.9). Note that in contrast to Chapter 5, we propose a different flux to this analysis, and it is justified by our purpose in this chapter: we are based on SN simulations, and the flux in (7.10) reproduce better neutrinos from simulated SN explosions as well as represents a more general parameterization as discussed in [39]. In Figure 31 it is shown the initial fluxes $\phi^0_{\nu_\beta}$ (before flavor conversion) as a function of energy and time.

Using the fluxes described above as well as equation (7.9) the expected number of events for the three detectors are calculated in the energy spectrum of simulated

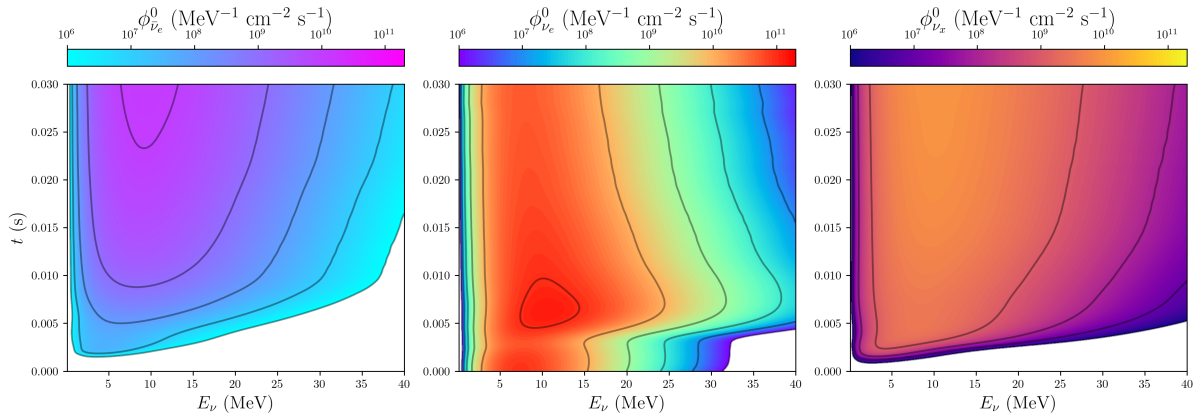

Figure 31 – Initial time-energy dependent flux for the simulation of the SN with 27 $M_\odot$ progenitor for $\bar{\nu}_e$ (left), ν_e (middle), and ν_x (right), considering only the neutronization burst phase. Level curves correspond to values that appear in the color bars.

progenitors (11.2 $M_\odot$ and 27 $M_\odot$) for both hierarchies and are compared to MSC$^\epsilon$ model, and are reported in Figure 32. The results translate what is shown in Figure 29, weighted by detector capabilities. Expected changes in the spectrum look more prominent when NH is assumed as a standard solution for DUNE, with an increase of ν_e events for both hierarchies. On the other hand, for HK and JUNO the MSC$^\epsilon$ effect results in a decrease of events in IH and an increase in NH and it is not so clear which hierarchy would be more sensible to the MSC$^\epsilon$ effect since the number of QD parameters for each one is different for both P_{ee} and $\bar{P}_{ee}$. For instance, for $\bar{P}^{\rm NH}_{ee}$, fixing Γ_3, an increase in Γ_8 is weighted by the factor 1/3 in the exponential terms, while $\bar{P}^{\rm IH}_{ee}$ is more sensible to Γ_8, since the same change is multiplied by a factor 1, but it is also independent of Γ_3.

Note that eq. (4.13) is valid for a conserved total flux, which does not remain in the ν-loss scenario. To get around this issue we propose a more generalized form of (4.13)

$$\begin{aligned}
\phi_{\nu_e} &= \phi^0_{\nu_e} P_{ee} + \phi^0_{\nu_x}(P_{\mu e} + P_{\tau e}) \\
\phi_{\bar{\nu}_e} &= \phi^0_{\bar{\nu}_e} \bar{P}_{ee} + \phi^0_{\nu_x}(\bar{P}_{\mu e} + \bar{P}_{\tau e}) \\
\phi'_{\nu_x} &= \phi^0_{\nu_e}(P_{e\mu} + P_{e\tau}) + \phi^0_{\nu_x}(P_{\mu\mu} + P_{\mu\tau} + P_{\tau\tau} + P_{\tau\mu}) \ , \\
\phi'_{\bar{\nu}_x} &= \phi^0_{\bar{\nu}_e}(\bar{P}_{e\mu} + \bar{P}_{e\tau}) + \phi^0_{\bar{\nu}_x}(\bar{P}_{\mu\mu} + \bar{P}_{\mu\tau} + \bar{P}_{\tau\tau} + \bar{P}_{\tau\mu}) \\
\phi_{\nu_x} &= \phi'_{\nu_x} + \phi'_{\bar{\nu}_x}
\end{aligned} \tag{7.12}$$

where each probability can be factorized as described in (7.6). For the ones where $\alpha = \mu, \tau$, since these flavors are generated in a superposition of mass states in matter, the $\nu_\mu - \nu_\tau$ mixing should be taken into account, where $P^{m\rm SN}_{\alpha i}$ and $\bar{P}^{m\rm SN}_{\alpha i}$ would correspond to the proper square module of elements from $U_{\mu\tau}$ mixing matrix[6]. In Figure 33 we show each

[6] In the $\mu - \tau$ sector, such probability is associated to θ_{23} mixing, being a sub-matrix of U_{23} in the conventional PMNS decomposition. We also assume in this formula that any oscillation term is averaged out.

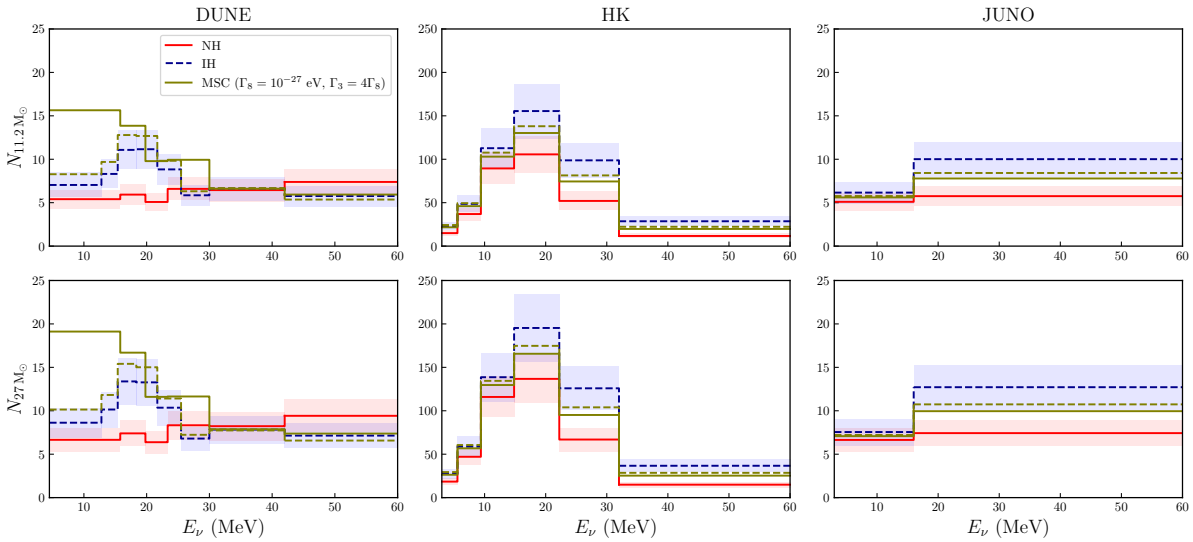

Figure 32 – Our calculated spectrum of events for DUNE, HK and JUNO for NH (solid lines) and IH (dashed), with $n = 0$ for a 10 kpc SN with 11.2 $M_\odot$ and 27 $M_\odot$ progenitor mass simulations. Each column concerns a detector, while the rows are related to progenitor masses. The size of bins is at least twice the resolution at the specific energy and given a minimum threshold in the number of events per bin established in our analysis. The bands are to respect the 40% of the uncertainty of the flux over standard NH and IH, with details in the text. For the QD parameters, we used the values $\Gamma_8 = 10^{-27}$ eV and $\Gamma_3 = 4\Gamma_8$.

probability $P_{\alpha\beta}$ for a 10 kpc SN for the ν-loss scenario. In Figure 34 we show the expected spectrum of events for the ν-loss model.

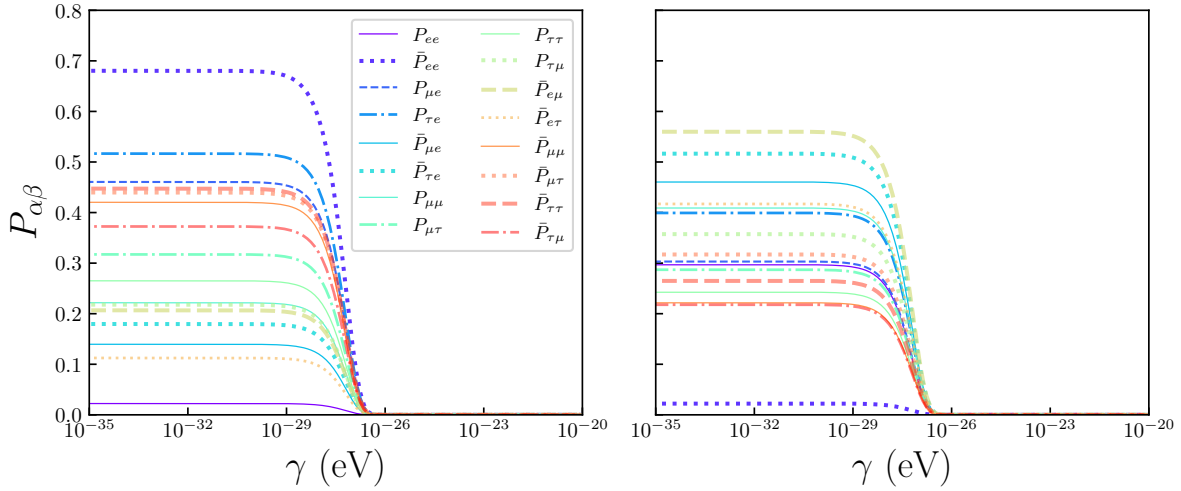

Figure 33 – Probabilities with the impact of ν-loss with $n = 0$ considering a 10 kpc SN for NH (left) and IH (right).

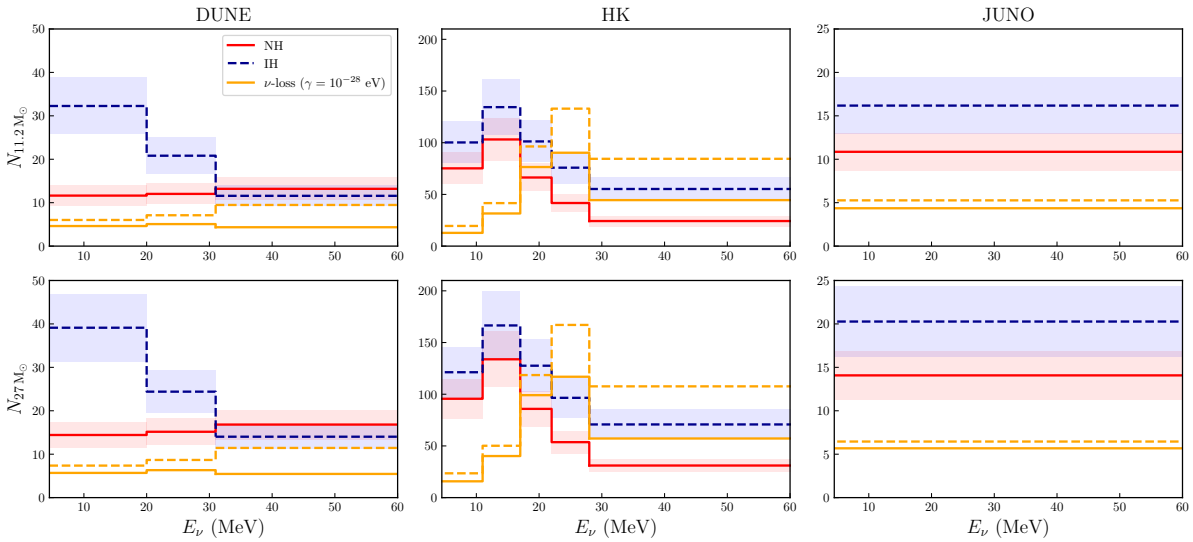

Figure 34 – Spectrum of events for DUNE, HK and JUNO for NH (solid lines) and IH (dashed) compared to ν-loss model, with $n = 0$ for a 10 kpc SN with 11.2 $M_\odot$ and 27 $M_\odot$ progenitor mass simulations. For ν-loss we use different bin sizes in order to achieve the requirement of a minimum number of events per bin of ~ 5. Given the lack of events in this scenario, we decided to use a single bin for JUNO.

7.2.3 Role of Earth matter effects

Since a galactic SN detection can be impacted by Earth matter effects, we also calculate P_{ee} and $\bar{P}_{ee}$ to each detector given the position of the SN in the sky. However, as shown in Section 3.3, regeneration would start to be important beyond $E_\nu \gtrsim 50$ MeV or even higher energies, which is close to the end of the expected spectrum for SN neutrinos.

In Figure 35 we see the QD effects (MSC$^\epsilon$ with $n = 0$) combined with Earth matter effects for a specific energy (similarly as shown in Figure 29, but for a wide range of θ_z and the QD parameter). The asymptotic maximal mixing suppresses regeneration effects beyond $\Gamma_8 \sim 10^{-27}$ eV for a 10 kpc SN, being a leading effect. Since regeneration is a second-order effect, we impose bounds on QD in the next section without considering Earth matter effects, and by the end of Section 7.3.2, we show its impact on results.

7.3 Future limits on quantum decoherence

In order to impose bounds on QD using simulated data, we perform a binned χ^2 through pull method [113] over QD parameters for MSC and ν-loss scenarios:

$$\chi^2 = \sum_d \sum_{j=1}^{m} \frac{(N_{j,d}^{\text{true}} - (1+a)N_{j,d}^{\text{th}})^2}{N_{j,d}^{\text{th}}} + \frac{a^2}{\sigma_a^2} \,, \tag{7.13}$$

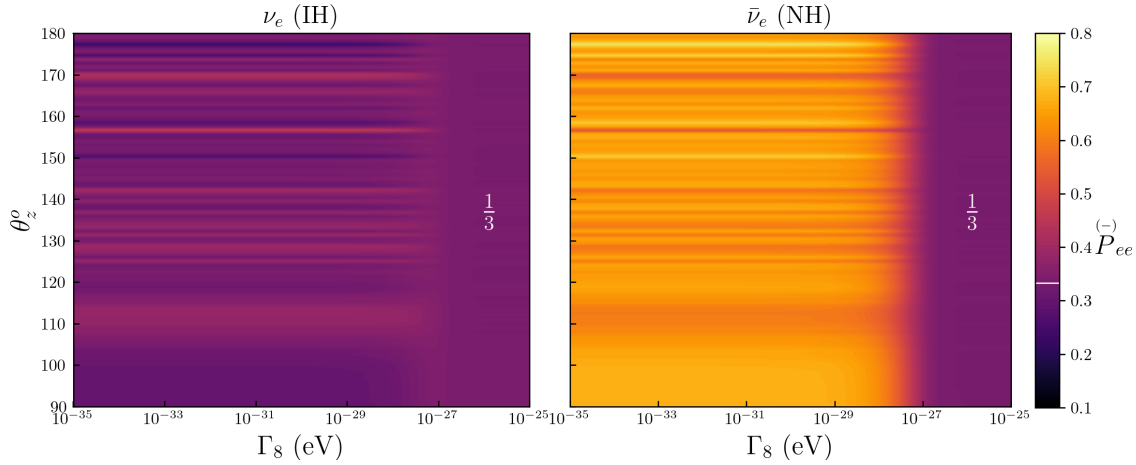

Figure 35 – P_{ee} in IH (left) and $\bar{P}_{ee}$ in NH (right) under Earth matter effects as a function of QD parameter for $E_\nu = 30$ MeV, considering a SN 10 kpc away from Earth and $n = 0$. It is possible to see that QD suppresses regeneration effects for $\Gamma_8 \gtrsim 10^{-27}$ eV, where $\Gamma_3 = 10^{-32}$ eV was set. The white line on the color bar represents maximal mixing.

where m indicates the number of energy bins, d represents each detector, $N_{j,d}^{\text{true}}$ represents events predicted by the MSW solution, and $N_{j,d}^{\text{th}}$ accounts the theoretical number of events of the marginalized model in our analysis, i.e. MSW + quantum decoherence respectively and the second term on the right-hand side takes our estimation in the flux uncertainties of 40% into account [2].

We can note in Figure 33 that since all probabilities vanish for high values of γ, $N \to 0$ for ν-loss. However in order to avoid a bias in our analysis, we marginalize over γ only in a range where the requirement of at least ~ 5 events per bin is achieved (we use the same rule for MSC). We also take the size of the bins to be twice the detector energy resolution. Using these requirements, JUNO allows a single bin for ν-loss, being a counting experiment for this analysis. The bins scheme for DUNE and HK are also changed for ν-loss compared to MSC in order to match the established minimum number of events per bin in the tested range of γ.

Before imposing limits on MSC and ν-loss with eq. (7.13), we can treat P_{ee} and $\bar{P}_{ee}$ as free parameters, which is a reasonable approximation to an adiabatic propagation at the SN, since these probabilities are energy independent (see Section 5.2 or [53] for a more detailed discussion in the context of SN1987A), we perform a marginalization with $\chi^2(P_{ee}, \bar{P}_{ee})$ in eq. (7.13) to understand how far asymptotically QD scenarios are from the standard ν mixing and also see how sensible a combined measurement (DUNE+HK+JUNO) could be, using uniquely the neutronization burst. Figure 36 shows how a 10 kpc SN can impose limits to P_{ee} and $\bar{P}_{ee}$, with NH and IH concerning the true MSW model. The black dot represents maximal mixing or the asymptotic limit of MSC, which is closer to

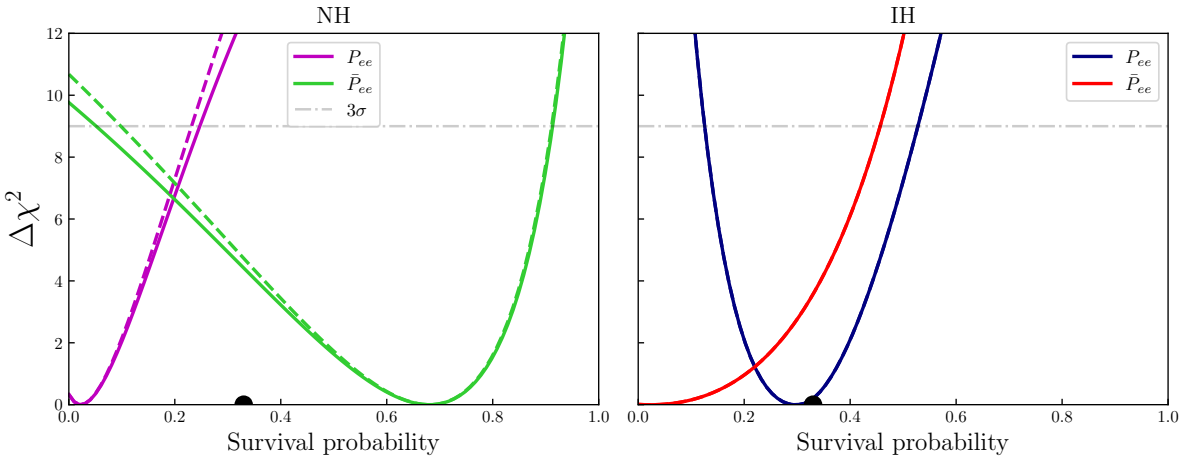

Figure 36 – Limits on P_{ee} and $\bar{P}_{ee}$ for the 27 $M_\odot$ (solid) and 11.2 $M_\odot$ (dashed) progenitor stars from simulations, considering only the neutronization burst. No quantum decoherence effects are taken into account in this Figure. The distance from Earth considered was 10 kpc. The probability is assumed to be a free parameter as recently proposed in [53]. The assumption of a standard adiabatic MSW conversion at the SN is taken into account (as all along the manuscript), getting rid of the energy dependency on P_{ee} and $\bar{P}_{ee}$. The black dot is the maximal mixing scenario (1/3). Note that the 11.2 $M_\odot$ line for IH matches to the 27 $M_\odot$, showing that the sensitivity for simulated progenitors tested is similar.

the IH solution (given by the corresponding best-fit value) than NH for P_{ee}, but in an intermediary point of hierarchies with respect to $\bar{P}_{ee}$. In the ν-loss scenario it is not so clear from Figure 36 which hierarchy would lead to stronger constraints, given the presence of other probabilities, such as the ones in Figure 33.

Using eq. (7.13) and the procedures described in Sections 7.1 and 7.2, we treat QD parameters as free and perform a χ^2 analysis in order to impose statistical bounds in this effect using a future SN detection. Since nowadays the neutrino mass hierarchy is not established, we include both scenarios in our analysis.

We test both MSW-NH versus the marginalized MSW-NH + QD and also the MSW-IH versus the marginalized MSW-IH + QD in order to understand how restrictive future detectors will be. The results will show that if QD plays any role in SN neutrinos, both possible ν hierarchies could be affected.

7.3.1 MSC$^{\not\ell}$

For the MSC$^{\not\ell}$ model, we calculate the $\sqrt{\Delta\chi^2}$ bounds over the parameter Γ, where $\Delta\chi^2 = \chi^2 - \chi^2_{\text{min}}$ (since we are not including statistical and systematic uncertainties when producing the "true" data, we always have $\chi^2_{\text{min}} = 0$). The results for the 3 experiments

are summarized in Figure 37, where the true scenario is NH and we marginalize over NH+QD. Note that bounds reach different significant limits for each SN distance, with lower distances being more restrictive.

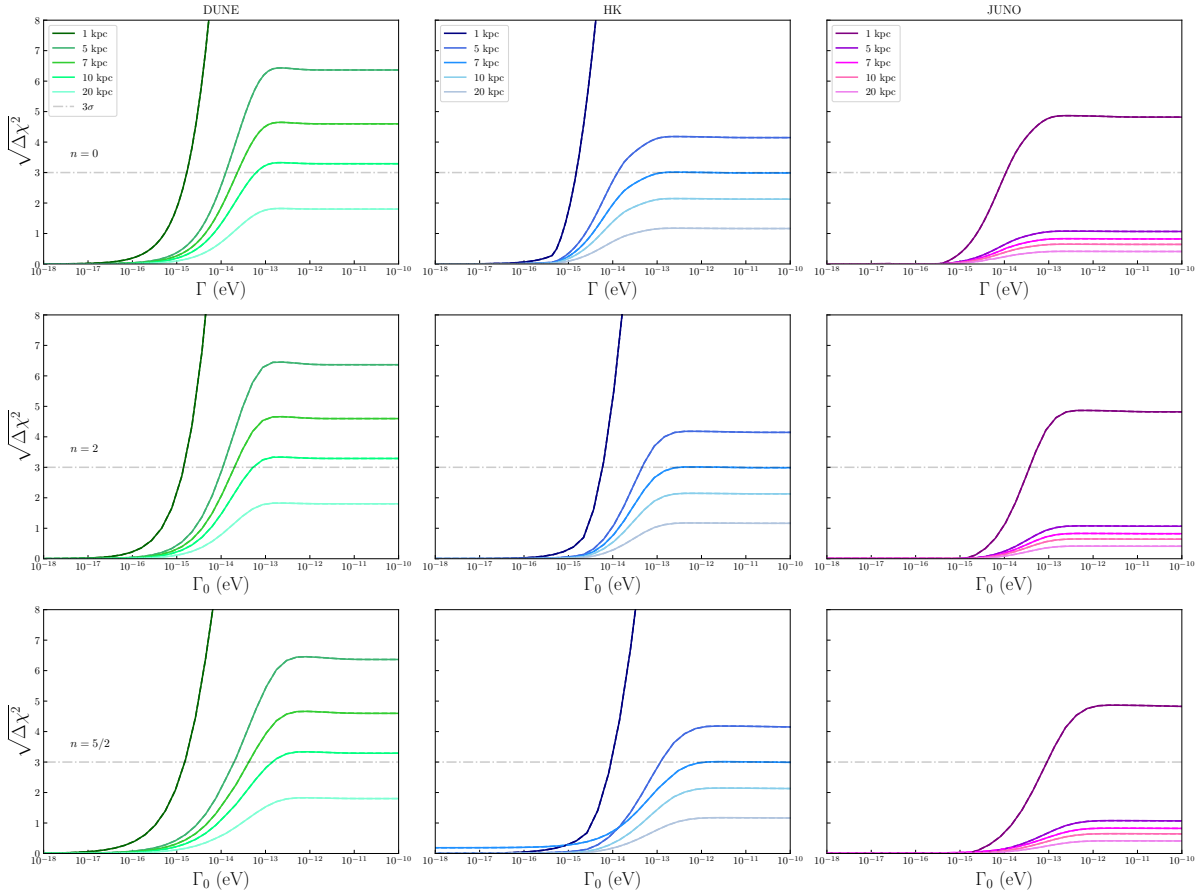

Figure 37 – Limits on Γ for various SN distances from Earth for DUNE (left), HK (middle), and JUNO (right) for the 40 $M_\odot$ progenitor star simulation. The true scenario taken into account was NH, and we marginalize the parameters over the theoretical NH+QD (MSC$^\ell$). No Earth matter effect was considered. Each row means a different value of n in the parameterization $\Gamma = \Gamma_0(E/E_0)^n$.

Since the traveled distance is a fixed feature, the only aspect that the SN distance from Earth contributes is the number of events detected. Following Figure 37, the best performance in NH is for DUNE, with possible 3σ limits for a 10 kpc SN away from Earth of:

$$\Gamma_0 \leqslant \begin{cases} 6.2 \times 10^{-14}\ \text{eV} & (n = 0) \\ 5.2 \times 10^{-14}\ \text{eV} & (n = 2) \\ 1.4 \times 10^{-13}\ \text{eV} & (n = 5/2) \end{cases} \tag{7.14}$$

For a SN at a distance of 1 kpc, limits of $\mathcal{O}(10^{-16})$ eV can be reached. HK has also a good performance and achieves 2σ bounds for a 10 kpc SN. JUNO is not capable of

individually achieving reasonable bounds on QD for SN distances $\gtrsim 1$ kpc, but would also have a strong signal for a galactic SN as close as 1 kpc away from Earth, which can be attributed to the small fiducial mass compared to HK and a single IBD channel considered in this work (with a significantly lower cross-section than ν_e-Ar for energies above ~ 15 MeV). Other channels, such as ν-p elastic scattering could possibly improve the results, but given the detection challenges associated, it was decided to not include them here.

The same analysis was also performed using IH as the true theory and marginalizing over IH+QD. The results are shown in Figure 38. The best performance is clearly for HK with 2σ bound of:

$$\Gamma_0 \leqslant \begin{cases} 3.6 \times 10^{-14}\ \text{eV} & (n=0) \\ 8.0 \times 10^{-14}\ \text{eV} & (n=2) \\ 2.4 \times 10^{-13}\ \text{eV} & (n=5/2) \end{cases} \tag{7.15}$$

for a 10 kpc SN from Earth. DUNE is not capable to impose strong bounds in an IH scenario. JUNO performance is improved for distances $\lesssim 1$ kpc compared to NH. Results are summarized in Table 2 in Appendix E.

A 20 kpc SN could not impose strong bounds for individual experiments. Distances as far as 50 kpc (as Large Magellanic Cloud) were not investigated in this work, given the lack of events per bin, in which a more refined unbinned statistical analysis would be required, which is not strongly motivated by the fact that expected limits are below 2σ.

The bounds and sensitivity of each detector in a given hierarchy shown above could be associated with the sensitivity to P_{ee} and $\bar{P}_{ee}$ shown in Figure 36. In NH (left plot), limits over P_{ee} are more restrictive than $\bar{P}_{ee}$ with respect to maximal mixing represented by the black dot. For IH (right plot), we have an opposite sensitivity, since $P_{ee} \sim 1/3$, while for $\bar{P}_{ee}$ there is a gap between the best fit and 1/3 probability, allowing limits with certain significance to be imposed. Since DUNE is most sensitive to ν_e, via ν_e-Ar interaction, it will be more sensitive to P_{ee} and then more relevant in the NH scenario. As for HK and JUNO, they are more sensitive to $\bar{\nu}_e$ and therefore to $\bar{P}_{ee}$, which reflects a better performance in the IH scenario. In our calculations, the elastic scattering considered in HK does not contribute much to the total χ^2.

7.3.2 MSC$^{\epsilon}$

The same procedure described in the section above was performed on the MSC$^{\epsilon}$ model, with bounds over the parameter Γ_8 (and free Γ_3). Results are summarized in Figure 39 for NH vs NH+QD. SN distance also plays an important role in this scenario and results and their aspects are similar to MSC$^{\not\epsilon}$ described in the last section. DUNE

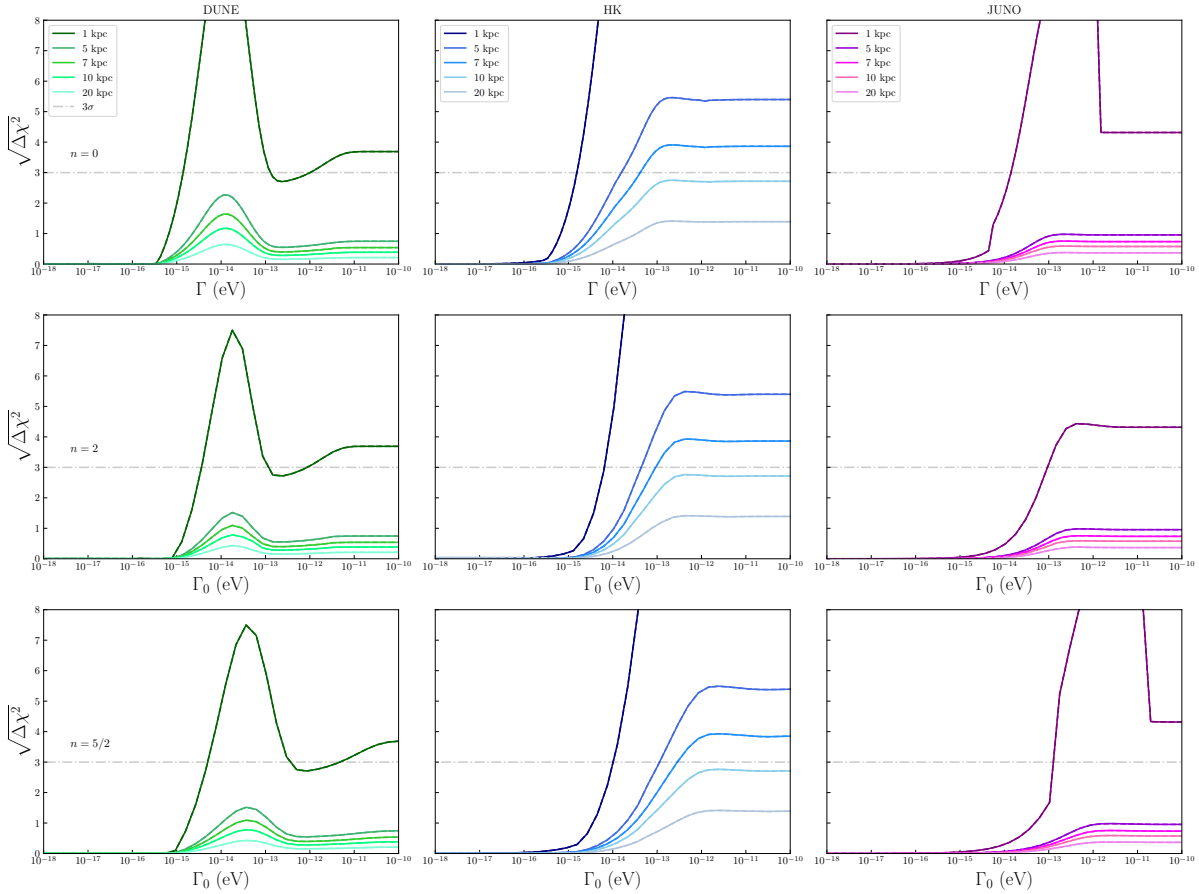

Figure 38 – Same as Figure 37 but with IH as the true theory, marginalized over the parameters of the IH+QD model.

has the best performance for the tested SN distances and even for a 10 kpc SN, bounds with 3σ could be achieved for $n = 0, 2$ and $5/2$. Despite the stronger effects caused by MSC for larger distances, the number of events decrease with L^2, and stronger limits can be imposed for a SN happening at shorter distances, reflecting that the larger number of neutrinos arriving at the detector is a crucial aspect.

From Figure 39, taking the result of a 10 kpc SN ($27\ M_\odot$), DUNE would potentially impose $\Gamma_8 \leqslant 4.2 \times 10^{-28}$ eV for 2σ and $\Gamma_8 \leqslant 1.7 \times 10^{-27}$ eV for 3σ with $n = 0$, whereas the HK bound is $\Gamma_8 \leqslant 4.2 \times 10^{-27}$ eV for 2σ. Looking at limits from various works [80, 90, 91, 92, 93, 94, 88, 95, 98, 89, 99, 96], to the best knowledge of the author, this is an unprecedented level of sensitivity for testing quantum decoherence, orders of magnitude more restrictive than any other work in the subject. Figure 40 shows bounds from works with different sources and place the limits from this work for both hierarchy scenarios.

Note that for $n = 2$ and $5/2$ the bounds are over Γ_{08} in $\Gamma_8 = \Gamma_{08}(E/E_0)^n$. For a 10 kpc SN ($27 M_\odot$), DUNE 3σ bounds reach:

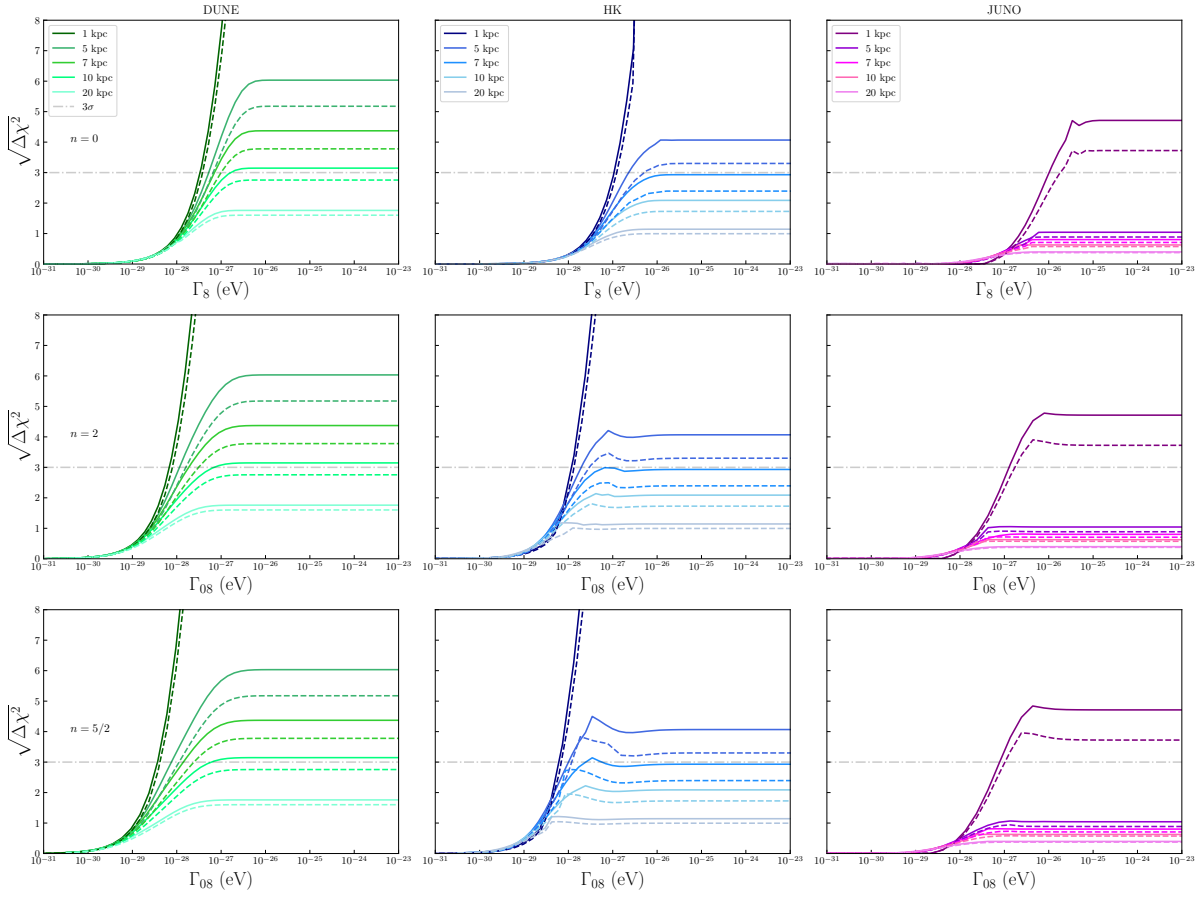

Figure 39 – Same as 37 but for MSC$^{\epsilon}$ with simulations of the 27 $M_{\odot}$ (solid) and 11.2 $M_{\odot}$ (dashed) progenitor masses. The bounds are orders of magnitude more restrictive than for MSC$^{\not\epsilon}$.

$$\Gamma_{08} \leqslant \begin{cases} 7.0 \times 10^{-28}\ \text{eV} & (n = 2) \\ 6.2 \times 10^{-28}\ \text{eV} & (n = 5/2) \end{cases} . \tag{7.16}$$

HK is able to achieve 2σ bounds as restrictive as $\Gamma_{08} \leqslant 2.7 \times 10^{-28}$ eV and $\Gamma_{08} \leqslant 1.2 \times 10^{-28}$ eV for $n = 2$ and $5/2$ respectively. All mentioned results are summarized in Table 3 in the Appendix E.

We also performed a combined fit for the three detectors using the same ν hierarchy scheme shown in Figure 41, where a 3σ limit for a 10 kpc SN would reach:

$$\Gamma_{08} \leqslant \begin{cases} 6.2 \times 10^{-28}\ \text{eV} & (n = 0) \\ 1.2 \times 10^{-28}\ \text{eV} & (n = 2) \\ 0.72 \times 10^{-28}\ \text{eV} & (n = 5/2) \end{cases} . \tag{7.17}$$

Even a 4σ of maximal mixing is possible to be achieved for all values of n, but such significance is achieved only by the 27 $M_{\odot}$ simulated progenitor. Although a combined analysis reaches high significance, it should be taken with a grain of salt, since it is not possible to be sure that experiments would be simultaneously in operation.

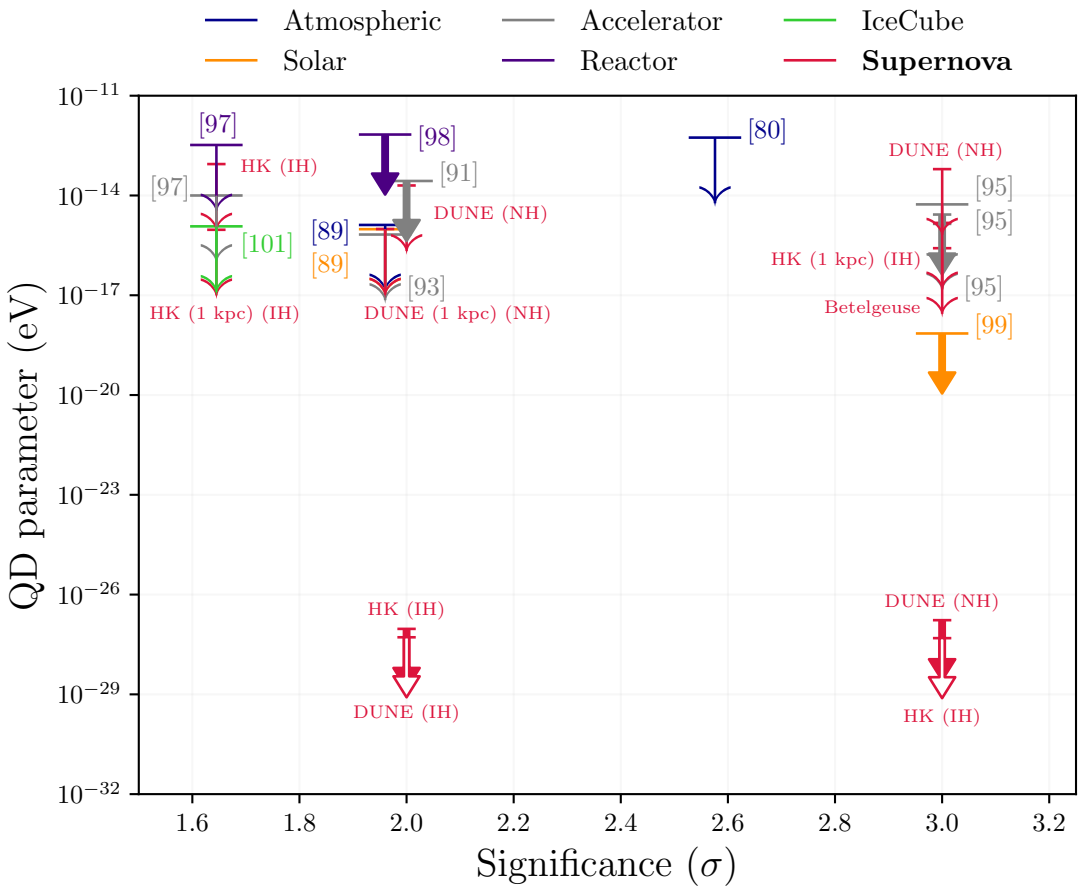

Figure 40 – Current bounds on quantum decoherence for a number of works from many neutrino sources and also the SN limits presented here ($n = 0$). Arrows with longer horizontal bases correspond to current experimental bounds, whereas minor bases are to respect to possible future limits. Numbers in the arrows indicate the reference in which the limits were obtained. Thin arrows indicate bounds equivalent to MSC$^{\ell}$, while thick-filled ones are the MSC$^{\epsilon}$. White-filled thick arrows correspond to ν-loss bounds. Supernova limits described in this work are in red, and are to respect to a distance of 10 kpc from Earth unless distance is indicated, with more restrictive bounds being possible for closer SNs.

Using the same procedure as done in NH, we make the analysis assuming IH as the true mixing and marginalizing over IH+QD. The results are shown in Figure 42. HK has the strongest bounds on this scenario but does not reach 3σ for a 10 kpc SN, even though the potential limits for 2σ are:

$$\Gamma_{08} \lesssim \begin{cases} 1.3 \times 10^{-27}\ \text{eV} & (n = 0) \\ 1.4 \times 10^{-28}\ \text{eV} & (n = 2) \\ 4.9 \times 10^{-28}\ \text{eV} & (n = 5/2) \end{cases} . \tag{7.18}$$

DUNE has a very poor performance in this scenario for any distance $\gtrsim 1$ kpc. JUNO sensitivity is similar to NH marginalization discussed above. In a combined fit in IH, shown

in Figure 43, the following 3σ limits can be obtained:

$$\Gamma_{08} \lesssim \begin{cases} 5.4 \times 10^{-27}\ \text{eV} & (n = 0) \\ 3.5 \times 10^{-27}\ \text{eV} & (n = 2) \\ 3.3 \times 10^{-27}\ \text{eV} & (n = 5/2) \end{cases} . \tag{7.19}$$

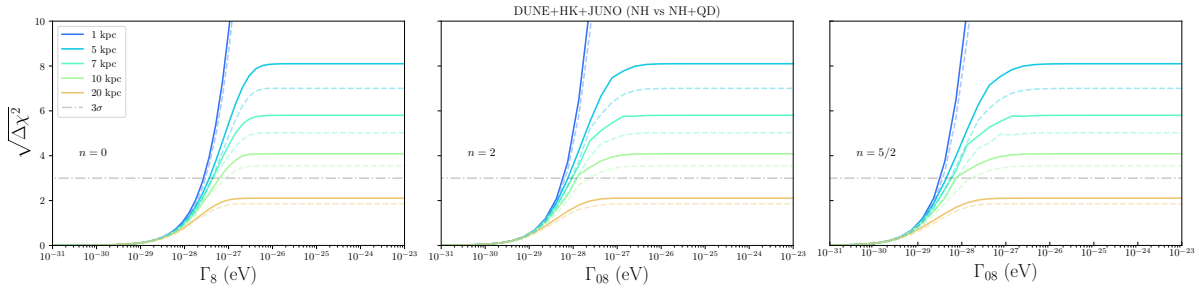

Figure 41 – Combined fit for the true MSW-NH marginalizing over MSW-NH with QD (MSC$^{\epsilon}$) effects.

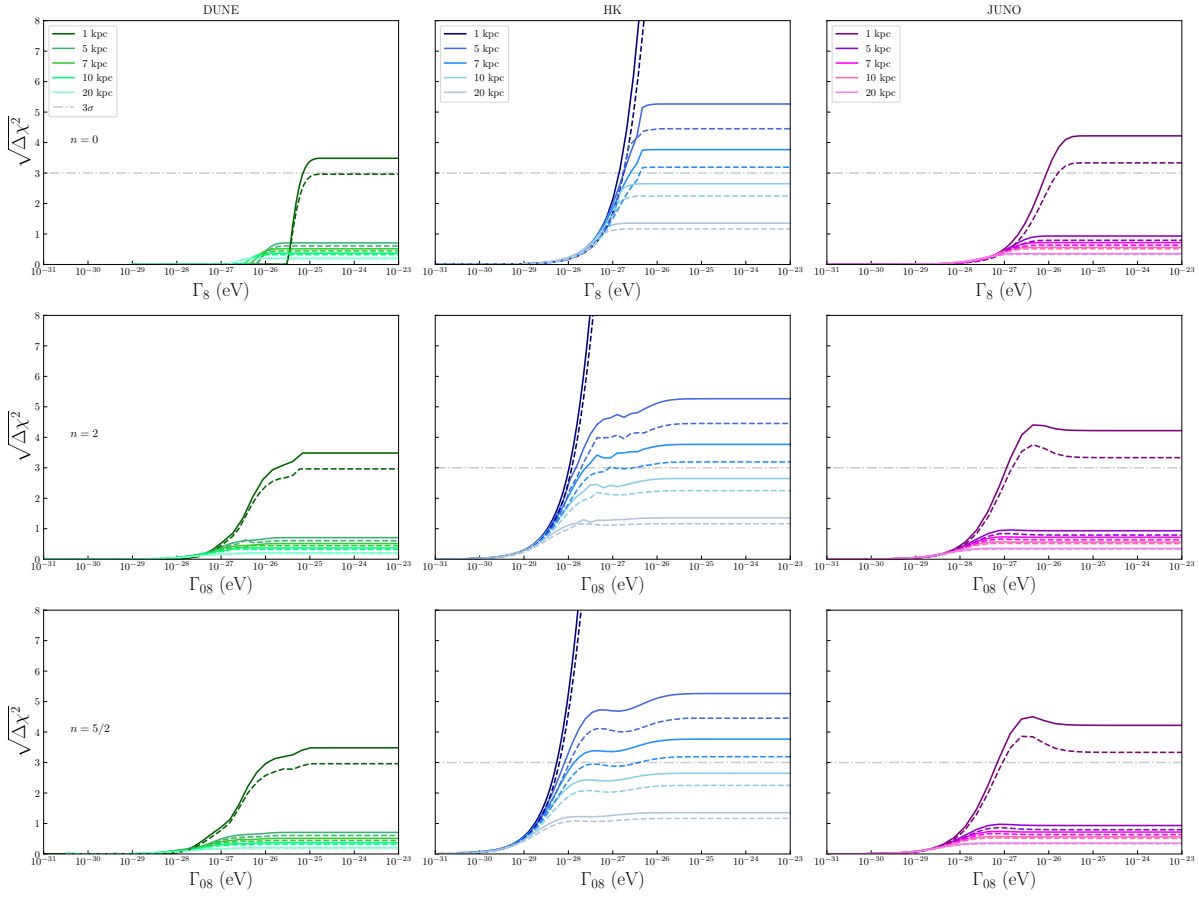

Figure 42 – Same as Figure 39 but for IH versus IH + QD.

To check the impact of regeneration on the above results, we calculated the bounds of a combined detection of DUNE, HK, and JUNO including this effect. We test different

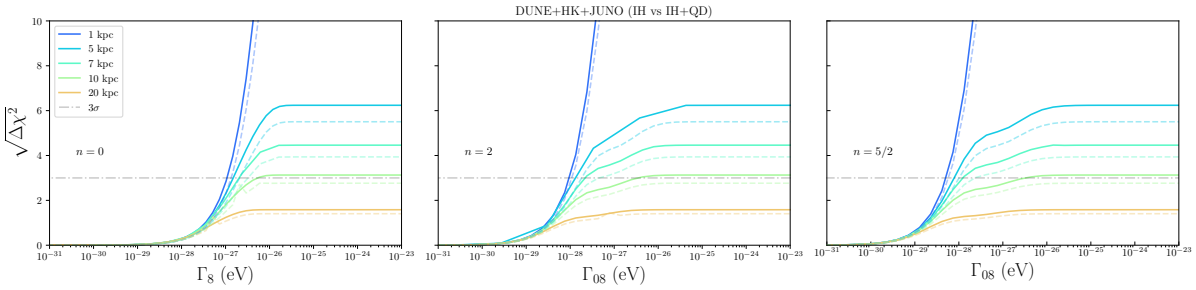

Figure 43 – Same as Figure 41 but now accounting the IH scenario.

θ_z, the zenith with respect to DUNE, with the assumption that the SN flux comes from DUNE longitude. The results are in Figure 44. We can note in the left plot that the impact of the Earth matter effect is small but enhances QD bounds for a 10 kpc detection and limits could be stressed beyond 4σ. The right plot shows the situation where the IH scenario is assumed to be true and NH+QD is marginalized. We will discuss such a scenario in Section 7.4, but we also see that regeneration will not change significantly the results.

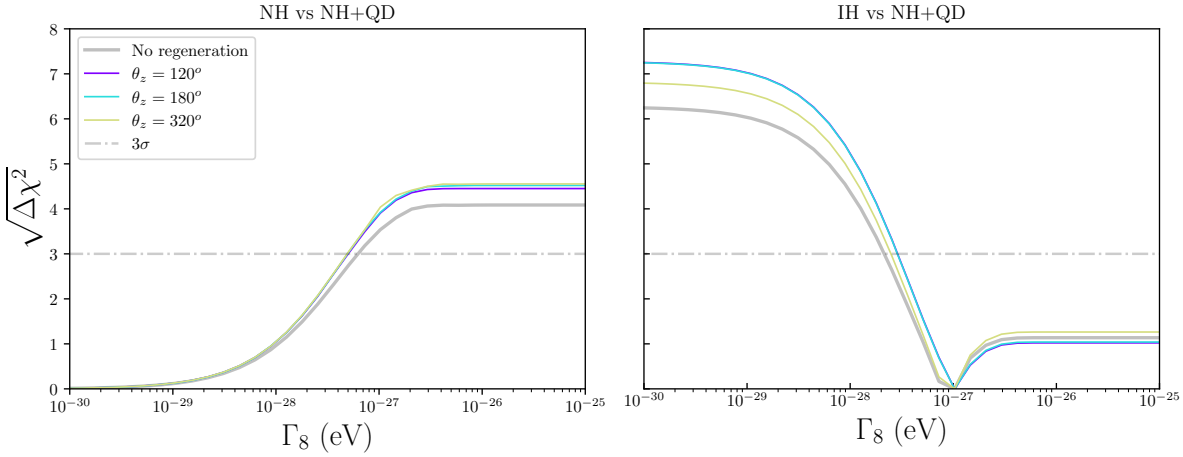

Figure 44 – Limits on MSC$^\epsilon$ with the impact of Earth matter effects for a SN 10 kpc from Earth and the 27 $M_\odot$ simulation for different zenith angles θ_z ($n = 0$). The limits correspond to a combined detection of DUNE, HK, and JUNO, but θ_z is to respect to DUNE, with SN beam in the direction of DUNE longitude. The $\theta_z = 320^o$ means that regeneration effects at HK and JUNO are expected, even if the SN beam does not cross Earth to reach DUNE.

7.3.3 Neutrino loss

Since in ν-loss the spectrum of events decreases asymptotically to zero, the bounds on this scenario are expected to be as significant or even more than MSC for all experiments. Since the calculated number of events for NH is low (mainly for DUNE and JUNO) and

ν-loss would decrease it, not fulfilling our requirement of $\gtrsim 5$ events per bin, we perform here only the IH (true) versus IH+QD. Figure 45 shows the $\sqrt{\Delta\chi^2}$ for each individual detector. We see that high values of γ are strongly bounded, even for JUNO. For a SN from 10 kpc away from Earth, DUNE, HK and JUNO are capable of imposing $\gamma \leqslant 5.2 \times 10^{-28}$ eV, $\gamma \leqslant 4.9 \times 10^{-28}$ eV and $\gamma \leqslant 5.9 \times 10^{-28}$ eV respectively with 3σ of significance ($n = 0$). Note that beyond 10 kpc the number of events per bin would be significantly small for a ν-loss scenario and we do not consider it in this analysis.

HK is capable to achieve the best (3σ) bounds with $\gamma_0 \leqslant 2.1 \times 10^{-29}$ eV and $\gamma_0 \leqslant 1.2 \times 10^{-29}$ eV for $n = 2$ and 5/2 respectively, with a 10 kpc SN. Although not shown in the plots, it is worth mentioning that HK would impose bounds on γ even for NH, given the high statistics associated with this experiment, being the most sensitive one for the ν-loss model. We detail the bounds and all mentioned results here in Table 4.

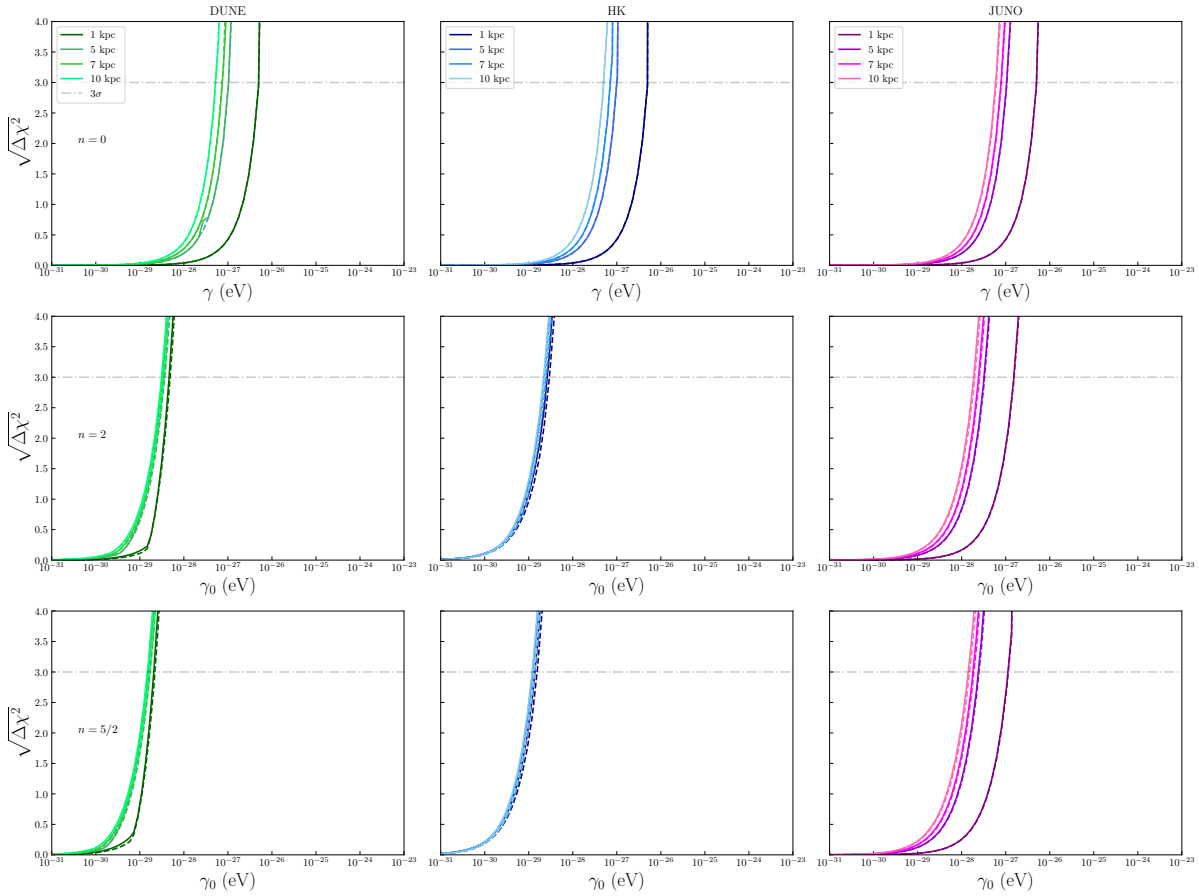

Figure 45 – Limits on γ for various SN distances from Earth for all detectors in the ν-loss scenario with true IH marginalized over the parameters of the IH+QD model.

7.4 Neutrino mass hierarchy measurement

In a future supernova detection, the neutronization burst arises as a robust test of neutrino mass hierarchy, with ν-Ar in DUNE capable to determine the correct scenario with relatively high confidence. However, although the possible strong bounds are to be imposed on quantum decoherence, if QD plays a significant role in ν mixing, the IH could be mimicked by a NH with the impact of QD (particularly, in the MSC models). A similar analysis was performed in the context of ν-decay in [2]. Therefore, the question that arises is how much NH and IH are distinguishable if we compare both hierarchies superposing the standard NH to QD. Figure 46 shows the statistical bounds of the scenario where IH is taken as the true theory and NH+QD is marginalized in a combined detection for $n = 0, 2, 5/2$. The results show that the significance of hierarchy determination significantly weakens for the tested SN distances and even a combined detection could not disentangle the hierarchies if MSC plays an important role.

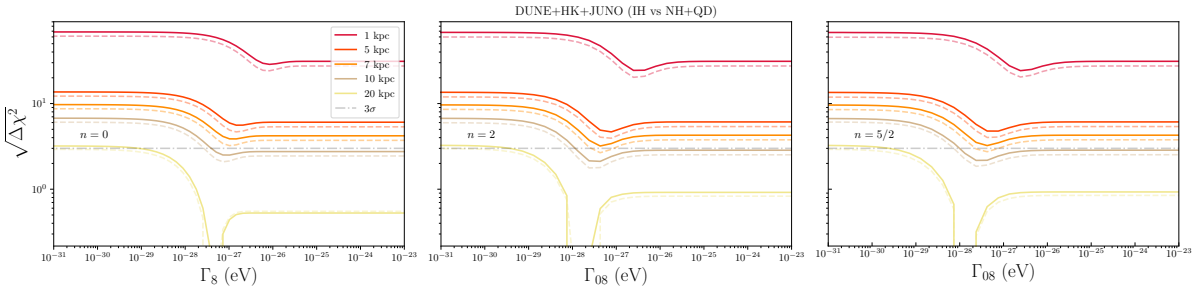

Figure 46 – Statistically comparing the inverted hierarchy (IH) to normal hierarchy (NH) with the impact of quantum decoherence for a combined detection using the 11.2 $M_\odot$ (dashed) and 27 $M_\odot$ (solid) simulations. No regeneration effects were taken into account.

To check this statement we can compare the values of $\sqrt{\Delta\chi^2}$ for $\Gamma_8 \to 0$ and $\Gamma_8 \to \infty$ in Figure 46. We can assume that $\sqrt{\Delta\chi^2}|_{\Gamma_8\to 0}$ corresponds to the distinguishability of hierarchies in a standard scenario since Γ_8 is small enough to neglect QD effects. The plateau in the limit of $\sqrt{\Delta\chi^2}|_{\Gamma_8\to\infty}$ shows how NH+QD would differ from IH in a future combined detection, in which has lower values of $\sqrt{\Delta\chi^2}$, resulting in a less significant hierarchy discrimination. Taking as a reference a SN distance of 10 kpc for the 27 $M_\odot$ simulation, with a combined detection of DUNE, HK and JUNO, we have a $\sqrt{\Delta\chi^2}|_{\Gamma_8\to 0} = 6.89$ going to $\sqrt{\Delta\chi^2}|_{\Gamma_8\to\infty} = 3.13$. For an individual detection with the same SN distance, DUNE would change from $\sqrt{\Delta\chi^2}|_{\Gamma_8\to 0} = 5.70$, which is statistically significant to determine the hierarchy, to a mere $\sqrt{\Delta\chi^2}|_{\Gamma_8\to\infty} = 0.37$. HK also could be affect with a $\sqrt{\Delta\chi^2}|_{\Gamma_8\to 0} = 3.36$ going to $\sqrt{\Delta\chi^2}|_{\Gamma_8\to\infty} = 2.65$. JUNO can not distinguish the neutrino hierarchies significantly at 10 kpc. It is important to mention that for 1 kpc and 5 kpc DUNE could be highly affected by this hierarchy misidentification, but HK still would provide a distinction of

$\gtrsim 5\sigma$ even with QD effects. For SN distances > 5 kpc, the neutrino hierarchies would be hardly disentangled by the tested experiments if QD effects are significant. As far as we tested, the ν-loss model did not lead to the same potential hierarchy misidentification found in the MSC.

Conclusions

In this thesis, we explored some prospects in supernova-neutrino mixing. It was shown that SN1987A provided an empiric and important starting point in our limited understanding of supernova neutrino emission. After more than 30 years of this astronomical event, many works are still based on its data. We showed that even with an analysis with low statistics, some information concerning the neutrino emission model could be extracted with proper statistical tools in Chapter 5, resulting in the publication [52] and the instructive animations are found here. Beyond that, neutrino mixing is also bounded by this data, and we see that the IH scenario is unfavorable, which resulted in the paper [53]. However, this limit should be taken carefully given the low statistics associated with our analysis, and future accelerator experiments or SN detection will address this question in the next decades. We also provided a detailed repository with the complete analysis found here.

The issue of pure quantum states spontaneously becoming mixed given exotic physics, or more specifically, quantum gravity, was also a topic investigated in this thesis, and in the author's opinion, where the main findings of this thesis were achieved. It was shown that even an incoherent state could be affected by quantum decoherence (QD) through relaxation.

We also have explored the capability of a future SN neutrino detection in imposing limits in quantum decoherence scenarios. We limit ourselves to scenarios where the decoherence matrix $D_{\mu\nu}$ is diagonal in the neutrino vacuum mass basis. Among the possible models to be investigated, we consider the ones we denoted as Mass State Coupling (MSC), leading to maximal mixing of states, and the neutrino loss (ν-loss), associated with the loss of neutrino flux along propagation. We also explored a possible dependency of quantum decoherence parameters with energy in the form of $\gamma = \gamma_0(E/E_0)^n$. Therefore, we explore the limits on the decoherence parameters for different n values. The analysis considered DUNE, HK, and JUNO as possible detectors. For the neutrino flux data, three progenitor stars were considered: a 40 $M_\odot$ (LS180-s40.0), 27 $M_\odot$ (LS220s27.0c) and 11.2 $M_\odot$ (LS220s11.2c), using the SN simulation data from the Garching group [40, 41, 39]. Only the neutronization burst was considered to get around the unsolved problem of collective effects since they are expected not to play a significant role in this

emission phase.

When considering the neutrino propagation inside the supernova, the relaxation effect could affect the neutrino flavor conversion, even with the assumption of no exchange of neutrino energy to the environment, or $[H, V_p] = 0$ (MSC$^{\not\epsilon}$). We show that in this regime, it is possible to get competitive limits to QD parameters. However, the required values for the decoherence parameters need to be much larger than the ones in the scenario where $[H, V_p] \neq 0$ (MSC$^{\epsilon}$) (see Appendix D), which would provide the most restrictive bounds on QD to date. For MSC$^{\epsilon}$, we only consider the relaxation acting on neutrino propagation in the vacuum from the SN up to the detectors at Earth, for which the propagation length is orders of magnitude larger than the SN size and, therefore, more sensible to the relaxation effects. We also explore the possible effects of Earth regeneration due to the neutrino propagation inside the Earth, which has minor effects on the bounds for the relaxation parameters, being the vacuum propagation the most relevant coherence length.

With all considerations, we show that the detectors used in the analysis are capable of imposing the limits listed in Tables 2 and 3 for the MSC scenario, depending on the distance being considered and the neutrino mass hierarchy. For the NH, the DUNE detector is the most promising, while HK is the most sensible in the case of IH. The possible limits on the decoherence parameters are orders of magnitude stronger than the ones imposed by current terrestrial and solar experiments, as shown in Figure 40. For the ν-loss scenario, the limits are shown in Table 4. Finally, we explored the possible degeneracy between the standard scenarios of unknown mass hierarchy (NH and IH) without and with QD effects. As we saw, the IH scenario could be easily mimicked by NH combined with QD-MSC effects.

The findings associated with quantum decoherence resulted in the paper [103]. After an invitation, some of our results were also implemented in the Python module SNEWPY, developed by SNEWS collaboration.

Bibliography

1 GONZALEZ-GARCIA, M. C.; MALTONI, M.; SCHWETZ, T. Nufit: three-flavour global analyses of neutrino oscillation experiments. *Universe*, MDPI, v. 7, n. 12, p. 459, 2021. Citado 2 vezes nas páginas 12 and 18.

2 GOUVÊA, A. D.; MARTINEZ-SOLER, I.; SEN, M. Impact of neutrino decays on the supernova neutronization-burst flux. *Physical Review D*, APS, v. 101, n. 4, p. 043013, 2020. Citado 3 vezes nas páginas 15, 87, and 97.

3 HAWKING, S. W. The unpredictability of quantum gravity. *Communications in Mathematical Physics*, Springer, v. 87, p. 395–415, 1982. Citado 2 vezes nas páginas 15 and 62.

4 NG, Y. J. Quantum foam. In: WORLD SCIENTIFIC. *The Tenth Marcel Grossmann Meeting: On Recent Developments in Theoretical and Experimental General Relativity, Gravitation and Relativistic Field Theories (In 3 Volumes)*. [S.l.], 2005. p. 2150–2164. Citado na página 15.

5 PDG. Review of particle physics. *Progress of Theoretical and Experimental Physics*, Oxford University Press, v. 2020, n. 8, p. 1–2093, 2020. Citado 2 vezes nas páginas 17 and 25.

6 GIUNTI, C.; KIM, C. W. *Fundamentals of neutrino physics and astrophysics*. [S.l.]: Oxford university press, 2007. Citado 2 vezes nas páginas 17 and 21.

7 DOLINSKI, M. J.; POON, A. W.; RODEJOHANN, W. Neutrinoless double-beta decay: status and prospects. *Annual Review of Nuclear and Particle Science*, Annual Reviews, v. 69, p. 219–251, 2019. Citado na página 18.

8 GOUVÊA, A. D. Neutrino mass models. *Annual Review of Nuclear and Particle Science*, Annual Reviews, v. 66, p. 197–217, 2016. Citado na página 18.

9 DIRECT neutrino-mass measurement with sub-electronvolt sensitivity. *Nature Physics*, Nature Publishing Group UK London, v. 18, n. 2, p. 160–166, 2022. Citado na página 18.

10 SHIRAI, J.; COLLABORATION, K.-Z. et al. Results and future plans for the kamland-zen experiment. In: IOP PUBLISHING. *Journal of Physics: Conference Series*. [S.l.], 2017. v. 888, n. 1, p. 012031. Citado na página 18.

11 ZHANG, C. et al. Recent results from the daya bay experiment. In: AIP PUBLISHING. *AIP Conference Proceedings*. [S.l.], 2015. v. 1666, n. 1. Citado na página 18.

12 SUZUKI, Y. The super-kamiokande experiment. *The European Physical Journal C*, Springer, v. 79, p. 1–18, 2019. Citado na página 18.

13 HIMMEL, A. *New oscillation results from the NOvA experiment.* [S.l.], 2020. Citado na página 18.

14 IWAMOTO, K.; COLLABORATION, T. et al. Recent results from t2k and future prospects. In: SISSA MEDIALAB. *38th International Conference on High Energy Physics.* [S.l.], 2017. v. 282, p. 517. Citado na página 18.

15 ABE, K.; ABE, K.; AIHARA, H.; AIMI, A.; AKUTSU, R.; ANDREOPOULOS, C.; ANGHEL, I.; ANTHONY, L.; ANTONOVA, M.; ASHIDA, Y. et al. Hyper-kamiokande design report. *arXiv preprint arXiv:1805.04163*, 2018. Citado na página 18.

16 COLLABORATION, D. et al. Deep underground neutrino experiment (dune): Far detector technical design report. volume i. introduction to dune. *Journal of Instrumentation*, IOP Publishing, v. 15, n. 8, 2020. Citado na página 18.

17 COLLABORATION, J. et al. JUNO physics and detector. *Progress in Particle and Nuclear Physics*, Elsevier, v. 123, p. 103927, 2022. Citado 2 vezes nas páginas 18 and 82.

18 VITAGLIANO, E.; TAMBORRA, I.; RAFFELT, G. Grand unified neutrino spectrum at earth: Sources and spectral components. *Reviews of Modern Physics*, APS, v. 92, n. 4, p. 045006, 2020. Citado na página 19.

19 XU, X.-J.; WANG, Z.; CHEN, S. Solar neutrino physics. *Progress in Particle and Nuclear Physics*, Elsevier, p. 104043, 2023. Citado na página 18.

20 DECOWSKI, M.; COLLABORATION, K. et al. Kamland's precision neutrino oscillation measurements. *Nuclear Physics B*, Elsevier, v. 908, p. 52–61, 2016. Citado na página 19.

21 QIAN, X.; PENG, J.-C. Physics with reactor neutrinos. *Reports on Progress in Physics*, IOP Publishing, v. 82, n. 3, p. 036201, 2019. Citado na página 19.

22 GAISSER, T. K. Atmospheric neutrinos. *arXiv preprint arXiv:1910.08851*, 2019. Citado na página 19.

23 WOLFENSTEIN, L. Neutrino oscillations in matter. *Phys. Rev.*, D17, p. 2369, 1978. Citado 2 vezes nas páginas 33 and 36.

24 MIKHEEV, S. P.; SMIRNOV, A. Y. Resonance enhancement of oscillations in matter and solar neutrino spectroscopy. *Sov. J. Nucl. Phys.*, v. 42, p. 913–917, 1985. Citado na página 33.

25 _____. Resonant amplification of neutrino oscillations in matter and solar neutrino spectroscopy. *Nuovo Cim.*, C9, p. 17–26, 1986. Citado 2 vezes nas páginas 33 and 36.

26 LINDER, J. *Derivation of neutrino matter potentials induced by earth.* [S.l.], 2005. Citado na página 33.

27 BLENNOW, M.; SMIRNOV, A. Y. Neutrino propagation in matter. *Adv.High Energy Phys.*, v. 2013, p. 972485, 2013. Citado na página 33.

28 BAHCALL, J. N.; SERENELLI, A. M.; BASU, S. New solar opacities, abundances, helioseismology, and neutrino fluxes. *The Astrophysical Journal*, IOP Publishing, v. 621, n. 1, p. L85, 2005. Citado 2 vezes nas páginas 35 and 37.

29 LANDAU, L. On the theory of transfer of energy at collisions ii. *Phys. Z. Sowjetunion*, v. 2, n. 46, p. 118, 1932. Citado na página 36.

30 ZENER, C. Non-adiabatic crossing of energy levels. *Proceedings of the Royal Society of London. Series A, Containing Papers of a Mathematical and Physical Character*, The Royal Society London, v. 137, n. 833, p. 696–702, 1932. Citado 2 vezes nas páginas 36 and 45.

31 MIKHEYEV, S.; SMIRNOV, A. Y. 3ν oscillations in matter and solar neutrino data. *Physics Letters B*, Elsevier, v. 200, n. 4, p. 560–564, 1988. Citado 2 vezes nas páginas 36 and 45.

32 SMIRNOV, A. Y. The msw effect and matter effects in neutrino oscillations. *Physica Scripta*, IOP Publishing, v. 2005, n. T121, p. 57, 2005. Citado na página 36.

33 ANDERSON, D. Theory of the Earth. Blackwell Scientific Publications. *Boston, MA*, 1989. Citado na página 38.

34 ROZWADOWSKA, K.; VISSANI, F.; CAPPELLARO, E. On the rate of core collapse supernovae in the milky way. *New Astronomy*, Elsevier, v. 83, p. 101498, 2021. Citado na página 41.

35 JANKA, H.-T. Neutrino emission from supernovae. In: _____. *Handbook of Supernovae*. Cham: Springer International Publishing, 2017. p. 1575–1604. ISBN 978-3-319-21846-5. Disponível em: <https://doi.org/10.1007/978-3-319-21846-5_4>. Citado na página 41.

36 DIGHE, A. S.; SMIRNOV, A. Y. Identifying the neutrino mass spectrum from a supernova neutrino burst. *Physical Review D*, APS, v. 62, n. 3, p. 033007, 2000. Citado 2 vezes nas páginas 43 and 46.

37 PARKE, S. J. Nonadiabatic level crossing in resonant neutrino oscillations. *Physical Review Letters*, APS, v. 57, n. 10, p. 1275, 1986. Citado na página 45.

38 BRUGGEN, M.; HAXTON, W.; QIAN, Y.-Z. Landau-zener treatments of solar neutrino oscillations. *Physical Review D*, APS, v. 51, n. 8, p. 4028, 1995. Citado na página 45.

39 MIRIZZI, A.; TAMBORRA, I.; JANKA, H.-T.; SAVIANO, N.; SCHOLBERG, K.; BOLLIG, R.; HÜDEPOHL, L.; CHAKRABORTY, S. Supernova neutrinos: production, oscillations and detection. *La Rivista del Nuovo Cimento*, Springer, v. 39, p. 1–112, 2016. Citado 7 vezes nas páginas 45, 46, 48, 78, 79, 83, and 99.

40 Garching group. *A variety of sophisticated Supernovae simulations from 1D to 3D is done by Garching group and access to specific results can be asked in <https://wwwmpa.mpa-garching.mpg.de/ccsnarchive/>*. [S.l.], 2023. Citado 8 vezes nas páginas 45, 46, 48, 75, 76, 78, 79, and 99.

41 SERPICO, P. D.; CHAKRABORTY, S.; FISCHER, T.; HÜDEPOHL, L.; JANKA, H.-T.; MIRIZZI, A. Probing the neutrino mass hierarchy with the rise time of a supernova burst. *Physical Review D*, APS, v. 85, n. 8, p. 085031, 2012. Citado 5 vezes nas páginas 46, 75, 76, 78, and 99.

42 LUND, T.; KNELLER, J. P. Combining collective, msw, and turbulence effects in supernova neutrino flavor evolution. *Physical Review D*, APS, v. 88, n. 2, p. 023008, 2013. Citado 2 vezes nas páginas 47 and 48.

43 PATTON, K. M.; KNELLER, J. P.; MCLAUGHLIN, G. C. Stimulated neutrino transformation through turbulence. *Physical Review D*, APS, v. 89, n. 7, p. 073022, 2014. Citado na página 47.

44 BURROWS, A.; VARTANYAN, D. Core-collapse supernova explosion theory. *Nature*, Nature Publishing Group UK London, v. 589, n. 7840, p. 29–39, 2021. Citado na página 48.

45 TAMBORRA, I.; SHALGAR, S. New developments in flavor evolution of a dense neutrino gas. *Annual Review of Nuclear and Particle Science*, Annual Reviews, v. 71, p. 165–188, 2021. Citado 2 vezes nas páginas 48 and 49.

46 NETO, P. D.; KEMP, E. Neutrino–(anti) neutrino forward scattering potential for massive neutrinos at low energies. *Modern Physics Letters A*, World Scientific, v. 37, n. 08, p. 2250048, 2022. Citado na página 48.

47 HIRATA, K. et al. Observation of a Neutrino Burst from the Supernova SN 1987a. *Phys. Rev. Lett.*, v. 58, p. 1490–1493, 1987. Citado na página 51.

48 HIRATA, K.; KAJITA, T.; KOSHIBA, M.; NAKAHATA, M.; OYAMA, Y.; SATO, N.; SUZUKI, A.; TAKITA, M.; TOTSUKA, Y.; KIFUNE, T. et al. Observation in the kamiokande-ii detector of the neutrino burst from supernova sn1987a. *Physical Review D*, APS, v. 38, n. 2, p. 448, 1988. Citado na página 51.

49 BIONTA, R. M. et al. Observation of a Neutrino Burst in Coincidence with Supernova SN 1987a in the Large Magellanic Cloud. *Phys. Rev. Lett.*, v. 58, p. 1494, 1987. Citado na página 51.

50 HAINES, T. et al. Neutrinos From SN1987A in the Imb Detector. *Nucl. Instrum. Meth. A*, v. 264, p. 28–31, 1988. Citado na página 51.

51 ALEKSEEV, E. N.; ALEKSEEVA, L. N.; KRIVOSHEINA, I. V.; VOLCHENKO, V. I. Detection of the Neutrino Signal From SN1987A in the LMC Using the Inr Baksan Underground Scintillation Telescope. *Phys. Lett. B*, v. 205, p. 209–214, 1988. Citado 2 vezes nas páginas 51 and 53.

52 SANTOS, M. V. dos; HOLANDA, P. C. de. Understanding and visualizing the statistical analysis of sn1987a neutrino data. *The European Physical Journal C*, Springer, v. 82, n. 2, p. 145, 2022. Citado 3 vezes nas páginas 51, 52, and 99.

53 NETO, P. D.; SANTOS, M. V. dos; HOLANDA, P. C. de; KEMP, E. Sn1987a neutrino burst: limits on flavor conversion. *The European Physical Journal C*, Springer, v. 83, n. 6, p. 459, 2023. Citado 6 vezes nas páginas 51, 59, 61, 87, 88, and 99.

54 PAGLIAROLI, G.; VISSANI, F.; COSTANTINI, M.; IANNI, A. Improved analysis of sn1987a antineutrino events. *Astroparticle Physics*, Elsevier, v. 31, n. 3, p. 163–176, 2009. Citado 4 vezes nas páginas 53, 55, 56, and 60.

55 VOGEL, P.; BEACOM, J. F. Angular distribution of neutron inverse beta decay, ν e+ p$\rightarrow$ e++ n. *Physical Review D*, APS, v. 60, n. 5, p. 053003, 1999. Citado 2 vezes nas páginas 53 and 82.

56 IANNI, A.; PAGLIAROLI, G.; STRUMIA, A.; TORRES, F.; VILLANTE, F.; VISSANI, F. Likelihood for supernova neutrino analyses. *Physical Review D*, APS, v. 80, n. 4, p. 043007, 2009. Citado na página 53.

57 JEGERLEHNER, B.; NEUBIG, F.; RAFFELT, G. Neutrino oscillations and the supernova 1987a signal. *Physical Review D*, APS, v. 54, n. 1, p. 1194, 1996. Citado na página 53.

58 COSTANTINI, M. L.; IANNI, A.; VISSANI, F. Sn1987a and the properties of the neutrino burst. *Physical Review D*, APS, v. 70, n. 4, p. 043006, 2004. Citado na página 53.

59 VISSANI, F.; PAGLIAROLI, G. Features of kamiokande-ii, imb, and baksan observations and their interpretation in a two-component model for the signal. *Astronomy letters*, Springer, v. 35, p. 1–6, 2009. Citado na página 53.

60 MIRIZZI, A.; RAFFELT, G. G. Analysis of the sn 1987a neutrinos with a flexible spectral shape. *Physical Review D*, APS, v. 72, n. 6, p. 063001, 2005. Citado na página 53.

61 COSTANTINI, M. L.; IANNI, A.; PAGLIAROLI, G.; VISSANI, F. Is there a problem with low energy sn1987a neutrinos? *Journal of Cosmology and Astroparticle Physics*, IOP Publishing, v. 2007, n. 05, p. 014, 2007. Citado na página 55.

62 YÜKSEL, H.; BEACOM, J. F. Neutrino spectrum from sn 1987a and from cosmic supernovae. *Physical Review D*, APS, v. 76, n. 8, p. 083007, 2007. Citado na página 55.

63 VISSANI, F. Comparative analysis of sn1987a antineutrino fluence. *Journal of Physics G: Nuclear and Particle Physics*, IOP Publishing, v. 42, n. 1, p. 013001, 2014. Citado na página 55.

64 LOREDO, T. J.; LAMB, D. Q. Bayesian analysis of neutrinos observed from supernova sn 1987a. *Physical Review D*, APS, v. 65, n. 6, p. 063002, 2002. Citado 3 vezes nas páginas 58, 59, and 60.

65 PAGLIAROLI, G.; ROSSI-TORRES, F.; VISSANI, F. Neutrino mass bound in the standard scenario for supernova electronic antineutrino emission. *Astroparticle Physics*, Elsevier, v. 33, n. 5-6, p. 287–291, 2010. Citado 2 vezes nas páginas 58 and 59.

66 HAWKING, S. The conservation of matter in general relativity. *Communications in Mathematical Physics*, Springer, v. 18, p. 301–306, 1970. Citado na página 62.

67 HAWKING, S. W. Particle creation by black holes. *Communications in mathematical physics*, Springer, v. 43, n. 3, p. 199–220, 1975. Citado na página 62.

68 _____. Breakdown of predictability in gravitational collapse. *Physical Review D*, APS, v. 14, n. 10, p. 2460, 1976. Citado na página 62.

69 ELLIS, J.; HAGELIN, J. S.; NANOPOULOS, D. V.; SREDNICKI, M. Search for violations of quantum mechanics. *Nuclear Physics B*, Elsevier, v. 241, n. 2, p. 381–405, 1984. Citado na página 62.

70 BANKS, T.; SUSSKIND, L.; PESKIN, M. E. Difficulties for the evolution of pure states into mixed states. *Nuclear Physics B*, Elsevier, v. 244, n. 1, p. 125–134, 1984. Citado 2 vezes nas páginas 62 and 64.

71 LIU, J. Evolution of pure states into mixed states. *arXiv preprint hep-th/9301082*, 1993. Citado 2 vezes nas páginas 62 and 64.

72 SREDNICKI, M. Is purity eternal? *Nuclear Physics B*, Elsevier, v. 410, n. 1, p. 143–154, 1993. Citado na página 62.

73 UNRUH, W. G.; WALD, R. M. Evolution laws taking pure states to mixed states in quantum field theory. *Physical Review D*, APS, v. 52, n. 4, p. 2176, 1995. Citado na página 62.

74 MARINOV, M. A quantum theory with possible leakage of information. *Nuclear Physics B*, Elsevier, v. 253, p. 609–620, 1985. Citado na página 62.

75 FORD, L. Gravitons and light cone fluctuations. *Physical Review D*, APS, v. 51, n. 4, p. 1692, 1995. Citado na página 62.

76 GORINI, V.; KOSSAKOWSKI, A.; SUDARSHAN, E. C. G. Completely positive dynamical semigroups of n-level systems. *Journal of Mathematical Physics*, American Institute of Physics, v. 17, n. 5, p. 821–825, 1976. Citado 3 vezes nas páginas 62, 63, and 115.

77 LINDBLAD, G. On the generators of quantum dynamical semigroups. *Communications in Mathematical Physics*, Springer, v. 48, p. 119–130, 1976. Citado 3 vezes nas páginas 62, 63, and 115.

78 BENATTI, F.; FLOREANINI, R. Completely positive dynamical maps and the neutral kaon system. *Nuclear physics B*, Elsevier, v. 488, n. 1-2, p. 335–363, 1997. Citado na página 62.

79 MAVROMATOS, N. E. Cpt violation and decoherence in quantum gravity. In: *Planck Scale Effects in Astrophysics and Cosmology*. [S.l.]: Springer, 2005. p. 245–320. Citado na página 62.

80 LISI, E.; MARRONE, A.; MONTANINO, D. Probing possible decoherence effects in atmospheric neutrino oscillations. *Physical Review Letters*, APS, v. 85, n. 6, p. 1166, 2000. Citado 4 vezes nas páginas 62, 73, 74, and 91.

81 BENATTI, F.; FLOREANINI, R. Open system approach to neutrino oscillations. *Journal of High Energy Physics*, IOP Publishing, v. 2000, n. 02, p. 032, 2000. Citado 3 vezes nas páginas 62, 66, and 68.

82 BREUER, H.-P.; PETRUCCIONE, F. *The theory of open quantum systems*. [S.l.]: Oxford University Press, USA, 2002. Citado 3 vezes nas páginas 63, 110, and 111.

83 BENATTI, F.; NARNHOFER, H. Entropy behaviour under completely positive maps. *letters in mathematical physics*, Springer, v. 15, p. 325–334, 1988. Citado na página 64.

84 GYAMFI, J. A. Fundamentals of quantum mechanics in liouville space. *European Journal of Physics*, IOP Publishing, v. 41, n. 6, p. 063002, 2020. Citado 2 vezes nas páginas 65 and 111.

85 KOTHE, S.; KIRTON, P. Liouville space neural network representation of density matrices. *arXiv preprint arXiv:2305.13992*, 2023. Citado na página 65.

86 OLIVEIRA, R. L. N. de. *Dissipaçao quântica em oscilaçoes de neutrinos*. Tese (Doutorado) — [sn], 2012. Citado na página 68.

87 GUZZO, M. M.; HOLANDA, P. C. de; OLIVEIRA, R. L. Quantum dissipation in a neutrino system propagating in vacuum and in matter. *Nuclear Physics B*, Elsevier, v. 908, p. 408–422, 2016. Citado na página 68.

88 CARRASCO, J.; DÍAZ, F.; GAGO, A. Probing CPT breaking induced by quantum decoherence at DUNE. *Physical Review D*, APS, v. 99, n. 7, p. 075022, 2019. Citado 4 vezes nas páginas 69, 73, 75, and 91.

89 COLOMA, P.; LOPEZ-PAVON, J.; MARTINEZ-SOLER, I.; NUNOKAWA, H. Decoherence in neutrino propagation through matter, and bounds from IceCube/DeepCore. *The European Physical Journal C*, Springer, v. 78, n. 8, p. 1–18, 2018. Citado 4 vezes nas páginas 73, 74, 91, and 120.

90 FARZAN, Y.; SCHWETZ, T.; SMIRNOV, A. Y. Reconciling results of LSND, MiniBooNE and other experiments with soft decoherence. *Journal of High Energy Physics*, IOP Publishing, v. 2008, n. 07, p. 067, 2008. Citado 2 vezes nas páginas 73 and 91.

91 OLIVEIRA, R.; GUZZO, M.; HOLANDA, P. de. Quantum dissipation and CP violation in MINOS. *Physical Review D*, APS, v. 89, n. 5, p. 053002, 2014. Citado 2 vezes nas páginas 73 and 91.

92 OLIVEIRA, R. L. Dissipative effect in long baseline neutrino experiments. *The European Physical Journal C*, Springer, v. 76, n. 7, p. 1–12, 2016. Citado 2 vezes nas páginas 73 and 91.

93 COELHO, J. A.; MANN, W. A.; BASHAR, S. S. Nonmaximal θ_{23} mixing at NOvA from neutrino decoherence. *Physical Review Letters*, APS, v. 118, n. 22, p. 221801, 2017. Citado 2 vezes nas páginas 73 and 91.

94 COELHO, J. A.; MANN, W. A. Decoherence, matter effect, and neutrino hierarchy signature in long baseline experiments. *Physical Review D*, APS, v. 96, n. 9, p. 093009, 2017. Citado 2 vezes nas páginas 73 and 91.

95 CARPIO, J.; MASSONI, E.; GAGO, A. Testing quantum decoherence at DUNE. *Physical Review D*, APS, v. 100, n. 1, p. 015035, 2019. Citado 2 vezes nas páginas 73 and 91.

96 GOMES, G. B.; FORERO, D.; GUZZO, M.; HOLANDA, P. D.; OLIVEIRA, R. Quantum decoherence effects in neutrino oscillations at DUNE. *Physical Review D*, APS, v. 100, n. 5, p. 055023, 2019. Citado 2 vezes nas páginas 73 and 91.

97 ROMERI, V. D.; GIUNTI, C.; STUTTARD, T.; TERNES, C. A. Neutrino oscillation bounds on quantum decoherence. *arXiv preprint arXiv:2306.14699*, 2023. Citado na página 73.

98 GOMES, G. B.; GUZZO, M.; HOLANDA, P. D.; OLIVEIRA, R. Parameter limits for neutrino oscillation with decoherence in KamLAND. *Physical Review D*, APS, v. 95, n. 11, p. 113005, 2017. Citado 2 vezes nas páginas 73 and 91.

99 HOLANDA, P. C. de. Solar neutrino limits on decoherence. *Journal of Cosmology and Astroparticle Physics*, IOP Publishing, v. 2020, n. 03, p. 012, 2020. Citado 4 vezes nas páginas 73, 74, 77, and 91.

100 FARZAN, Y.; SCHWETZ, T. A decoherence explanation of the gallium neutrino anomaly. *arXiv preprint arXiv:2306.09422*, 2023. Citado na página 73.

101 ABBASI, R.; ACKERMANN, M.; ADAMS, J.; AGARWALLA, S.; AGUILAR, J.; AHLERS, M.; ALAMEDDINE, J.; AMIN, N.; ANDEEN, K.; ANTON, G. et al. Searching for decoherence from quantum gravity at the icecube south pole neutrino observatory. *arXiv preprint arXiv:2308.00105*, 2023. Citado na página 73.

102 KELSO, C.; HOOPER, D. Probing exotic physics with supernova neutrinos. *arXiv preprint arXiv:1009.5996*, 2010. Citado na página 73.

103 SANTOS, M. V. dos; HOLANDA, P. C. de; NETO, P. D.; KEMP, E. On the effects of quantum decoherence in a future supernova neutrino detection. *arXiv e-prints*, p. arXiv–2306, 2023. Citado 2 vezes nas páginas 73 and 100.

104 STUTTARD, T.; JENSEN, M. Neutrino decoherence from quantum gravitational stochastic perturbations. *Physical Review D*, APS, v. 102, n. 11, p. 115003, 2020. Citado 5 vezes nas páginas 73, 74, 75, 76, and 77.

105 OLIVEIRA, R.; GUZZO, M. Quantum dissipation in vacuum neutrino oscillation. *The European Physical Journal C*, Springer, v. 69, n. 3, p. 493–502, 2010. Citado na página 74.

106 AMELINO-CAMELIA, G. Quantum-spacetime phenomenology. *Living Reviews in Relativity*, Springer, v. 16, n. 1, p. 1–137, 2013. Citado na página 74.

107 ANCHORDOQUI, L. A.; GOLDBERG, H.; GONZALEZ-GARCIA, M. C.; HALZEN, F.; HOOPER, D.; SARKAR, S.; WEILER, T. J. Probing Planck scale physics with IceCube. *Physical Review D*, APS, v. 72, n. 6, p. 065019, 2005. Citado na página 75.

108 SCHOLBERG, K.; ALBERT, J. B.; VASEL, J. SNOwGLoBES: SuperNova Observatories with GLoBES. *Astrophysics Source Code Library*, p. ascl–2109, 2021. Citado na página 82.

109 GOUVÊA, A. D.; MACHADO, P. A.; PEREZ-GONZALEZ, Y. F.; TABRIZI, Z. Measuring the Weak Mixing Angle in the DUNE Near-Detector Complex. *Physical review letters*, APS, v. 125, n. 5, p. 051803, 2020. Citado na página 82.

110 ABI, B.; ACCIARRI, R.; ACERO, M. A.; ADAMOV, G.; ADAMS, D.; ADINOLFI, M.; AHMAD, Z.; AHMED, J.; ALION, T.; MONSALVE, S. A. et al. Supernova neutrino burst detection with the Deep Underground Neutrino Experiment. *The European Physical Journal C*, Springer, v. 81, n. 5, p. 1–26, 2021. Citado na página 82.

111 DIGHE, A. S.; SMIRNOV, A. Yu. Identifying the neutrino mass spectrum from the neutrino burst from a supernova. *Phys. Rev.*, D62, p. 033007, 2000. Citado na página 83.

112 KEIL, M. T.; RAFFELT, G. G.; JANKA, H.-T. Monte carlo study of supernova neutrino spectra formation. *The Astrophysical Journal*, IOP Publishing, v. 590, n. 2, p. 971, 2003. Citado na página 83.

113 FOGLI, G.; LISI, E.; MARRONE, A.; MONTANINO, D.; PALAZZO, A. Getting the most from the statistical analysis of solar neutrino oscillations. *Physical Review D*, APS, v. 66, n. 5, p. 053010, 2002. Citado na página 86.

114 CHRUŚCIŃSKI, D.; PASCAZIO, S. A brief history of the gkls equation. *arXiv preprint arXiv:1710.05993*, 2017. Citado na página 110.

115 BENATTI, F.; FLOREANINI, R. Dissipative neutrino oscillations in randomly fluctuating matter. *Physical Review D*, APS, v. 71, n. 1, p. 013003, 2005. Citado na página 120.

Appendix A

Derivation of GKSL equation

We derive here the equation of motion for open quantum systems, the already mentioned GKSL equation. Most of the general ideas of this detailed derivation are in [82]. The consistent equation of motion in an open quantum system formalism has the fundamental assumption of no correlations between neutrino subsystem S and environment E in the initial time, then

$$\rho = \rho_S \otimes \rho_E. \tag{A.1}$$

Thus, the Hilbert space of the combined system is $\mathcal{H}_{S+E} = \mathcal{H}_S \otimes \mathcal{H}_E$ and the total Hamiltonian

$$H(t) = H_S \otimes \mathbb{1}_E + \mathbb{1}_S \otimes H_E + H_I(t), \tag{A.2}$$

where the $H_I(t)$ is the Hamiltonian that describes the interaction neutrino-environment. The reduced density matrix of the neutrino could be obtained by tracing over the environment

$$\rho_S(t) = \mathrm{Tr}_E[\rho(t)] = \mathrm{Tr}_E[U(t)\rho_S \otimes \rho_E U^\dagger(t)] \tag{A.3}$$

with $t_0 = 0$.

Considering the time evolution of $\rho_S(t)$, we are interested in the transformation from a density matrix into a density matrix by the action of some operator, such as

$$\rho_S(t) = \Lambda_t \rho_S \ , \tag{A.4}$$

that could be considered a snapshot of a particular time t, justifying the lower index (note that in the main text, we defined this operator as $\Lambda(t)$ in (6.1) to simplify the ideas to the reader). In order to get consistent properties of ρ_S, Λ_t should have hermiticity, trace-preserving, and complete positivity, and is characterized as a dynamical map [82, 114]. In other words, to establish a general form of Λ_t we can write $\rho_E = \sum_\sigma w_\sigma \left|\psi_\sigma\right\rangle\!\left\langle\psi_\sigma\right|$ in (A.3)

$$\rho_S(t) = \sum_\alpha \left\langle\psi_\alpha\right| U(t) \sum_\beta \left|\psi_\beta\right\rangle\!\left\langle\psi_\beta\right| \rho_S \otimes \sum_\sigma w_\sigma \left|\psi_\sigma\right\rangle\!\left\langle\psi_\sigma\right| U^\dagger(t) \left|\psi_\alpha\right\rangle \tag{A.5}$$

$$= \sum_{\alpha\beta\sigma} w_\sigma \delta_{\beta\sigma} \langle\psi_\alpha| U(t) |\psi_\beta\rangle \rho_S \langle\psi_\sigma| U^\dagger(t) |\psi_\alpha\rangle$$
$$= \sum_{\alpha\beta} w_\beta \langle\psi_\alpha| U(t) |\psi_\beta\rangle \rho_S \langle\psi_\beta| U^\dagger(t) |\psi_\alpha\rangle \ ,$$

where we used the definition of partial trace and completeness on the E basis. This leads to a definition of

$$W_{\alpha\beta}(t) = \sum_{\alpha\beta} \sqrt{w_\beta} \langle\psi_\alpha| U(t) |\psi_\beta\rangle \tag{A.6}$$

in which

$$\rho_S(t) = \sum_{\alpha\beta} W_{\alpha\beta}(t) \rho_S W^\dagger_{\alpha\beta}(t) \tag{A.7}$$

and

$$\sum_{\alpha\beta} W^\dagger_{\alpha\beta}(t) W_{\alpha\beta}(t) = \sum_{\alpha\beta} w_\beta \langle\psi_\beta| U^\dagger(t) |\psi_\alpha\rangle\langle\psi_\alpha| U(t) |\psi_\beta\rangle$$
$$= \sum_{\beta} w_\beta \langle\psi_\beta| U^\dagger(t) U(t) |\psi_\beta\rangle = \mathbb{1}_S,$$

which is a significant result, because

$$\mathrm{Tr}_S[\Lambda_t \rho_S] = \mathrm{Tr}_S \left[\sum_{\alpha\beta} W_{\alpha\beta}(t) \rho_S W^\dagger_{\alpha\beta}(t) \right] = \mathrm{Tr}_S \left[\sum_{\alpha\beta} W^\dagger_{\alpha\beta}(t) W_{\alpha\beta}(t) \rho_S \right] = \mathrm{Tr}_S \left[\rho_S\right] = 1, \tag{A.8}$$

once the trace one was preserved.

Our solution concern a fixed time, then one needs a family $\{\Lambda_t, t \geqslant 0\}$, that generates a quantum dynamical semigroup[1], with Λ_0 being the identity and the semigroup property is given by [82]

$$\Lambda_t \Lambda_u = \Lambda_{t+u}, \quad s, u \geqslant 0. \tag{A.9}$$

Once memory effects are not considered, it is possible to approximate the Markovian evolution. Considering a linear map $\mathcal{L}$ to be the generator of the semigroup, with dynamics

$$\frac{d\rho_S(t)}{dt} = \mathcal{L}\rho_S(t) \tag{A.10}$$

and solution $\rho_S(t) = \rho_S e^{\mathcal{L}t}$, which enables to write the dynamical map as $\Lambda_t = e^{\mathcal{L}t}$.

It is possible to find the most general form of $\mathcal{L}$ introducing an operator in the Liouville space F_i (see details of quantum mechanics in Liouville space in [84]), with $i = 1, 2, ..., N^2$ for a correspondent finite Hilbert space with dim $\mathcal{H}_S = N$. An orthonormal basis $\{B_i\}$ in this space satisfies orthogonality $(B_i, B_j) = \delta_{ij}$ and completeness $A = \sum_i B_i (B_i, A)$ conditions, where (A, B) means scalar product. So

[1] The inverse of the dynamical maps are not completely positive, thus they do not form a group.

$$(F_i, F_j) = \delta_{ij} \ , \tag{A.11}$$

and there is a conventional choice of an element to be proportional to the identity operator

$$F_{N^2} = \frac{1}{\sqrt{N}} \mathbb{1}_S \ , \tag{A.12}$$

that allow us to use traceless operators in the basis $\mathrm{Tr}_S\, F_i = 0,\ i = 1, 2, ..., N^2 - 1$. Therefore, considering the completeness relation for the Liouville space with the operator defined in (A.6)

$$W_{\alpha\beta}(t) = \sum_{i=1}^{N^2} F_i (F_i, W_{\alpha\beta}(t)) \tag{A.13}$$

and

$$W^{\dagger}_{\alpha\beta}(t) = \sum_{j=1}^{N^2} (F_j, W_{\alpha\beta}(t))^{\dagger} F_j^{\dagger} \tag{A.14}$$

enabling to rewrite equation (A.7) as

$$\rho_S(t) = \Lambda_t \rho_S = \sum_{\alpha\beta} \sum_{i=1}^{N^2} F_i (F_i, W_{\alpha\beta}(t)) \rho_S \sum_{j=1}^{N^2} (F_j, W_{\alpha\beta}(t))^{\dagger} F_j^{\dagger} \tag{A.15}$$

or in a more compact way:

$$\rho_S(t) = \sum_{i,j=1}^{N^2} c_{ij}(t) F_i \rho_S F_j^{\dagger} \tag{A.16}$$

where $c_{ij}(t) = (F_i, W_{\alpha\beta}(t))(F_j, W_{\alpha\beta}(t))^{\dagger}$ is a coefficient (matrix) positive and Hermitian. Considering equation (A.10) to be written as the definition of derivative:

$$\mathcal{L}\rho_S(t) = \lim_{t \to 0} \left[\frac{\Lambda_t \rho_S - \rho_S}{t} \right] \tag{A.17}$$

and applying (A.16) in (A.17), we have

$$\mathcal{L}\rho_S(t) = \lim_{t \to 0} \left[\frac{\sum_{i,j=1}^{N^2} c_{ij}(t) F_i \rho_S F_j^{\dagger} - \rho_S}{t} \right]. \tag{A.18}$$

The sum in (A.18) can be rewritten splitting the contributions of the identity element for the i and j indices

$$\sum_{i,j=1}^{N^2} c_{ij}(t)F_i\rho_S F_j^\dagger = c_{N^2N^2}(t)F_{N^2}\rho_S F_{N^2}^\dagger + \sum_{i=1}^{N^2-1} c_{iN^2}(t)F_i\rho_S F_{N^2}^\dagger + \sum_{j=1}^{N^2-1} c_{N^2j}(t)F_{N^2}\rho_S F_j^\dagger + \sum_{i,j=1}^{N^2-1} c_{ij}(t)F_i\rho_S F_j^\dagger$$

that can be simplified using (A.12):

$$\sum_{i,j=1}^{N^2} c_{ij}(t)F_i\rho_S F_j^\dagger = \frac{1}{N}c_{N^2N^2}(t)\rho_S + \frac{1}{\sqrt{N}}\sum_{i=1}^{N^2-1} c_{iN^2}(t)F_i\rho_S + \frac{1}{\sqrt{N}}\sum_{j=1}^{N^2-1} c_{N^2j}(t)\rho_S F_j^\dagger + \sum_{i,j=1}^{N^2-1} c_{ij}(t)F_i\rho_S F_j^\dagger.$$

Replacing this result in (A.18) gives

$$\mathcal{L}\rho_S(t) = \lim_{t\to 0}\left[\frac{1}{N}\frac{c_{N^2N^2}(t)\rho_S - N\rho_S}{t} + \frac{1}{\sqrt{N}}\sum_{i=1}^{N^2-1}\frac{c_{iN^2}(t)F_i\rho_S}{t} + \frac{1}{\sqrt{N}}\sum_{j=1}^{N^2-1}\frac{c_{N^2j}(t)\rho_S F_j^\dagger}{t} + \sum_{i,j=1}^{N^2-1}\frac{c_{ij}(t)F_i\rho_S F_j^\dagger}{t}\right] \tag{A.19}$$

that can be rewritten as

$$\mathcal{L}\rho_S(t) = \frac{1}{N}a_{N^2N^2}(t)\rho_S + \frac{1}{\sqrt{N}}\sum_{i=1}^{N^2-1} a_{iN^2}(t)F_i\rho_S + \frac{1}{\sqrt{N}}\sum_{j=1}^{N^2-1} a_{N^2j}(t)\rho_S F_j^\dagger + \sum_{i,j=1}^{N^2-1} a_{ij}(t)F_i\rho_S F_j^\dagger \tag{A.20}$$

where

$$\begin{aligned} a_{N^2N^2}(t) &= \lim_{t\to 0}\frac{c_{N^2N^2}(t) - N}{t} \\ a_{iN^2}(t) &= \lim_{t\to 0}\frac{c_{iN^2}(t)}{t} \\ a_{N^2j}(t) &= \lim_{t\to 0}\frac{c_{N^2j}(t)}{t} \\ a_{ij}(t) &= \lim_{t\to 0}\frac{c_{ij}(t)}{t}. \end{aligned} \tag{A.21}$$

Another usual simplification with this formalism is introducing the quantity

$$F = \frac{1}{\sqrt{N}}\sum_{i=1}^{N^2-1} a_{iN^2}F_i \tag{A.22}$$

$$\mathcal{L}\rho_S(t) = \frac{1}{N}a_{N^2N^2}(t)\rho_S + F\rho_S + \rho_S F^\dagger + \sum_{i,j=1}^{N^2-1} a_{ij}(t)F_i\rho_S F_j^\dagger. \tag{A.23}$$

Summing and subtracting $F^\dagger\rho_S$ and $\rho_S F$ will change (A.23) to

$$\begin{aligned}\mathcal{L}\rho_S(t) = \frac{1}{2}\Bigg\{ &\left[\frac{1}{N}a_{N^2N^2}(t) + F + F^\dagger\right]\rho_S + \rho_S\left[\frac{1}{N}a_{N^2N^2}(t) + F + F^\dagger\right] \\ &+ \left(F - F^\dagger\right)\rho_S + \rho_S\left(F^\dagger - F\right)\Bigg\} + \sum_{i,j=1}^{N^2-1} a_{ij}(t)F_i\rho_S F_j^\dagger\end{aligned} \tag{A.24}$$

where some terms were splitted into two parts (i.e $F\rho_S = \frac{1}{2}F\rho_S + \frac{1}{2}F\rho_S$). It is possible to introduce other two quantities in order to simplify (A.24)

$$\begin{aligned}A &= \frac{1}{2N}a_{N^2N^2}(t) + F + F^\dagger \\ H &= \frac{-i}{2}(F - F^\dagger)\end{aligned}, \tag{A.25}$$

leading to

$$\begin{aligned}\mathcal{L}\rho_S(t) &= A\rho_S + \rho_S A - iH\rho_S + i\rho_S H + \sum_{i,j=1}^{N^2-1} a_{ij}(t)F_i\rho_S F_j^\dagger \\ &= \{A, \rho_S\} - i[H, \rho_S] + \sum_{i,j=1}^{N^2-1} a_{ij}(t)F_i\rho_S F_j^\dagger.\end{aligned} \tag{A.26}$$

Once it is expected that the trace is not changing in time, or in other words, the time evolution of the density operator is trace-preserving, therefore

$$\mathrm{Tr}_S[\mathcal{L}\rho_S(t)] = 0$$

which leads to the right-hand side of (A.26) becomes

$$\begin{aligned}&\mathrm{Tr}_S(A\rho_S + \rho_S A) - i\,\mathrm{Tr}_S(H\rho_S - \rho_S H) + \mathrm{Tr}_S\left[\sum_{i,j=1}^{N^2-1} a_{ij}(t)F_i\rho_S F_j^\dagger\right] = \\ &= \mathrm{Tr}_S(A\rho_S) + \mathrm{Tr}_S(A\rho_S) - i\,\mathrm{Tr}_S(H\rho_S) - \mathrm{Tr}_S(H\rho_S) + \mathrm{Tr}_S\left[\sum_{i,j=1}^{N^2-1} a_{ij}(t)F_j^\dagger F_i\rho_S\right] = \\ &= 2\,\mathrm{Tr}_S(A\rho_S) + \mathrm{Tr}_S\left[\sum_{i,j=1}^{N^2-1} a_{ij}(t)F_j^\dagger F_i\rho_S\right] = \mathrm{Tr}_S\left\{\left[2A + \sum_{i,j=1}^{N^2-1} a_{ij}(t)F_j^\dagger F_i\right]\rho_S\right\} = 0\ ,\end{aligned}$$

$$\mathrm{Tr}_S\left\{\left[2A+\sum_{i,j=1}^{N^2-1}a_{ij}(t)F_j^\dagger F_i\right]\rho_S\right\}=\left[2A+\sum_{i,j=1}^{N^2-1}a_{ij}(t)F_j^\dagger F_i\right]\mathrm{Tr}_S(\rho_S)=0$$

where it was used the cyclic property of traces. This result makes it possible to write

$$A=-\frac{1}{2}\sum_{i,j=1}^{N^2-1}a_{ij}(t)F_j^\dagger F_i \tag{A.27}$$

then replacing (A.27) in (A.26)

$$\frac{d\rho_S(t)}{dt}=-i[H,\rho_S]+\sum_{i,j=1}^{N^2-1}a_{ij}(t)\left(F_i\rho_S F_j^\dagger-\frac{1}{2}\{F_j^\dagger F_i,\rho_S\}\right) \tag{A.28}$$

which is the most general form of evolution equation for $\rho_S(t)$ proposed by Gorini, Kossakowski and Sudarshan in 1976 [76]. Almost simultaneously, Lindblab proposed another version of the equation [77], where the $a_{ij}(t)$ could be diagonalized by a unitary transformation given by an operator u, such that $uau^\dagger=\mathrm{diag}(\gamma_1,\gamma_2,...,\gamma_{N^2-1})$. Then, the F_i operators could be written in a linear combination

$$F_i=\sum_{p=1}^{N^2-1}u_{pi}V_p \tag{A.29}$$

and replaced in (A.28), resulting

$$\frac{d\rho_S(t)}{dt}=-i[H,\rho_S]+\sum_{p=1}^{N^2-1}\gamma_p(t)\left(V_p\rho_S V_p^\dagger-\frac{1}{2}V_p^\dagger V_p\rho_S-\frac{1}{2}\rho_S V_p^\dagger V_p\right) \tag{A.30}$$

or

$$\frac{d\rho_S(t)}{dt}=-i[H,\rho_S]+\sum_{p=1}^{N^2-1}\gamma_p(t)\left(V_p\rho_S V_p^\dagger-\frac{1}{2}\{V_p^\dagger V_p,\rho_S\}\right) \tag{A.31}$$

that could be rewritten as

$$\frac{d\rho_S(t)}{dt}=-i[H,\rho_S]+\mathcal{D}(\rho_S), \tag{A.32}$$

and we can embed the $\gamma_p(t)$ terms in V_p operators to rewrite the dissipation part $\mathcal{D}(\rho_S)$ as

$$\mathcal{D}(\rho_S)=\frac{1}{2}\sum_{p=1}^{N^2-1}\left([V_p,\rho_S V_p^\dagger]+[V_p\rho_S,V_p^\dagger]\right)\ . \tag{A.33}$$

Appendix B

Parameters from $D_{\mu\nu}$ in terms of V_p coefficients for 3 neutrinos

The γ_i (diagonal) parameters of $D_{\mu\nu}$ in terms of $\mathbf{v}_\mu = \sum_{p=1}^{8} v_{p_\mu}$ of the $V_p = v_{p\mu}\lambda_\mu$ expansion can be defined as

$$
\begin{aligned}
\gamma_1 &= -\mathbf{v}_2^2 - \mathbf{v}_3^2 - \frac{\mathbf{v}_4^2}{4} - \frac{\mathbf{v}_5^2}{4} - \frac{\mathbf{v}_6^2}{4} - \frac{\mathbf{v}_7^2}{4} \\
\gamma_2 &= -\mathbf{v}_1^2 - \mathbf{v}_3^2 - \frac{\mathbf{v}_4^2}{4} - \frac{\mathbf{v}_5^2}{4} - \frac{\mathbf{v}_6^2}{4} - \frac{\mathbf{v}_7^2}{4} \\
\gamma_3 &= -\mathbf{v}_1^2 - \mathbf{v}_2^2 - \frac{\mathbf{v}_4^2}{4} - \frac{\mathbf{v}_5^2}{4} - \frac{\mathbf{v}_6^2}{4} - \frac{\mathbf{v}_7^2}{4} \\
\gamma_4 &= -\frac{\mathbf{v}_1^2}{4} - \frac{\mathbf{v}_2^2}{4} - \frac{\mathbf{v}_3^2}{4} - \frac{\sqrt{3}\mathbf{v}_3\mathbf{v}_8}{2} - \mathbf{v}_5^2 - \frac{\mathbf{v}_6^2}{4} - \frac{\mathbf{v}_7^2}{4} - \frac{3\mathbf{v}_8^2}{4} \\
\gamma_5 &= -\frac{\mathbf{v}_1^2}{4} - \frac{\mathbf{v}_2^2}{4} - \frac{\mathbf{v}_3^2}{4} - \frac{\sqrt{3}\mathbf{v}_3\mathbf{v}_8}{2} - \mathbf{v}_4^2 - \frac{\mathbf{v}_6^2}{4} - \frac{\mathbf{v}_7^2}{4} - \frac{3\mathbf{v}_8^2}{4} \\
\gamma_6 &= -\frac{\mathbf{v}_1^2}{4} - \frac{\mathbf{v}_2^2}{4} - \frac{\mathbf{v}_3^2}{4} + \frac{\sqrt{3}\mathbf{v}_3\mathbf{v}_8}{2} - \frac{\mathbf{v}_4^2}{4} - \frac{\mathbf{v}_5^2}{4} - \mathbf{v}_7^2 - \frac{3\mathbf{v}_8^2}{4} \\
\gamma_7 &= -\frac{\mathbf{v}_1^2}{4} - \frac{\mathbf{v}_2^2}{4} - \frac{\mathbf{v}_3^2}{4} + \frac{\sqrt{3}\mathbf{v}_3\mathbf{v}_8}{2} - \frac{\mathbf{v}_4^2}{4} - \frac{\mathbf{v}_5^2}{4} - \mathbf{v}_6^2 - \frac{3\mathbf{v}_8^2}{4} \\
\gamma_8 &= -\frac{3\mathbf{v}_4^2}{4} - \frac{3\mathbf{v}_5^2}{4} - \frac{3\mathbf{v}_6^2}{4} - \frac{3\mathbf{v}_7^2}{4}
\end{aligned}
\tag{B.1}
$$

and β_{ij} (non-diagonal) terms reads

$$
\begin{aligned}
\beta_{12} =& \mathbf{v}_1\mathbf{v}_2 \\
\beta_{13} =& \mathbf{v}_1\mathbf{v}_3 \\
\beta_{14} =& \frac{\mathbf{v}_1\mathbf{v}_4}{4} - \frac{3\mathbf{v}_2\mathbf{v}_5}{4} + \frac{3\mathbf{v}_3\mathbf{v}_6}{4} + \frac{\sqrt{3}\mathbf{v}_6\mathbf{v}_8}{4} \\
\beta_{15} =& \frac{\mathbf{v}_1\mathbf{v}_5}{4} + \frac{3\mathbf{v}_2\mathbf{v}_4}{4} + \frac{3\mathbf{v}_3\mathbf{v}_7}{4} + \frac{\sqrt{3}\mathbf{v}_7\mathbf{v}_8}{4} \\
\beta_{16} =& \frac{\mathbf{v}_1\mathbf{v}_6}{4} + \frac{3\mathbf{v}_2\mathbf{v}_7}{4} - \frac{3\mathbf{v}_3\mathbf{v}_4}{4} + \frac{\sqrt{3}\mathbf{v}_4\mathbf{v}_8}{4} \\
\beta_{17} =& \frac{\mathbf{v}_1\mathbf{v}_7}{4} - \frac{3\mathbf{v}_2\mathbf{v}_6}{4} - \frac{3\mathbf{v}_3\mathbf{v}_5}{4} + \frac{\sqrt{3}\mathbf{v}_5\mathbf{v}_8}{4} \\
\beta_{18} =& -\frac{\sqrt{3}\left(\mathbf{v}_4\mathbf{v}_6 + \mathbf{v}_5\mathbf{v}_7\right)}{2} \\
\beta_{23} =& \mathbf{v}_2\mathbf{v}_3 \\
\beta_{24} =& \frac{3\mathbf{v}_1\mathbf{v}_5}{4} + \frac{\mathbf{v}_2\mathbf{v}_4}{4} - \frac{3\mathbf{v}_3\mathbf{v}_7}{4} - \frac{\sqrt{3}\mathbf{v}_7\mathbf{v}_8}{4} \\
\beta_{25} =& -\frac{3\mathbf{v}_1\mathbf{v}_4}{4} + \frac{\mathbf{v}_2\mathbf{v}_5}{4} + \frac{3\mathbf{v}_3\mathbf{v}_6}{4} + \frac{\sqrt{3}\mathbf{v}_6\mathbf{v}_8}{4} \\
\beta_{26} =& -\frac{3\mathbf{v}_1\mathbf{v}_7}{4} + \frac{\mathbf{v}_2\mathbf{v}_6}{4} - \frac{3\mathbf{v}_3\mathbf{v}_5}{4} + \frac{\sqrt{3}\mathbf{v}_5\mathbf{v}_8}{4} \\
\beta_{27} =& \frac{3\mathbf{v}_1\mathbf{v}_6}{4} + \frac{\mathbf{v}_2\mathbf{v}_7}{4} + \frac{3\mathbf{v}_3\mathbf{v}_4}{4} - \frac{\sqrt{3}\mathbf{v}_4\mathbf{v}_8}{4} \\
\beta_{28} =& -\frac{\sqrt{3}\left(-\mathbf{v}_4\mathbf{v}_7 + \mathbf{v}_5\mathbf{v}_6\right)}{2} \\
\beta_{34} =& -\frac{3\mathbf{v}_1\mathbf{v}_6}{4} + \frac{3\mathbf{v}_2\mathbf{v}_7}{4} + \frac{\mathbf{v}_3\mathbf{v}_4}{4} + \frac{\sqrt{3}\mathbf{v}_4\mathbf{v}_8}{4} \\
\beta_{35} =& -\frac{3\mathbf{v}_1\mathbf{v}_7}{4} - \frac{3\mathbf{v}_2\mathbf{v}_6}{4} + \frac{\mathbf{v}_3\mathbf{v}_5}{4} + \frac{\sqrt{3}\mathbf{v}_5\mathbf{v}_8}{4} \\
\beta_{36} =& \frac{3\mathbf{v}_1\mathbf{v}_4}{4} + \frac{3\mathbf{v}_2\mathbf{v}_5}{4} + \frac{\mathbf{v}_3\mathbf{v}_6}{4} - \frac{\sqrt{3}\mathbf{v}_6\mathbf{v}_8}{4} \\
\beta_{37} =& \frac{3\mathbf{v}_1\mathbf{v}_5}{4} - \frac{3\mathbf{v}_2\mathbf{v}_4}{4} + \frac{\mathbf{v}_3\mathbf{v}_7}{4} - \frac{\sqrt{3}\mathbf{v}_7\mathbf{v}_8}{4} \\
\beta_{38} =& -\frac{\sqrt{3}\left(\mathbf{v}_4^2 + \mathbf{v}_5^2 - \mathbf{v}_6^2 - \mathbf{v}_7^2\right)}{4} \\
\beta_{45} =& \mathbf{v}_4\mathbf{v}_5 \\
\beta_{46} =& -\frac{\sqrt{3}\mathbf{v}_1\mathbf{v}_8}{2} + \frac{\mathbf{v}_4\mathbf{v}_6}{4} - \frac{3\mathbf{v}_5\mathbf{v}_7}{4} \\
\beta_{47} =& \frac{\sqrt{3}\mathbf{v}_2\mathbf{v}_8}{2} + \frac{\mathbf{v}_4\mathbf{v}_7}{4} + \frac{3\mathbf{v}_5\mathbf{v}_6}{4} \\
\beta_{48} =& \frac{\sqrt{3}\mathbf{v}_1\mathbf{v}_6}{4} - \frac{\sqrt{3}\mathbf{v}_2\mathbf{v}_7}{4} + \frac{\sqrt{3}\mathbf{v}_3\mathbf{v}_4}{4} + \frac{3\mathbf{v}_4\mathbf{v}_8}{4} \\
\beta_{56} =& -\frac{\sqrt{3}\mathbf{v}_2\mathbf{v}_8}{2} + \frac{3\mathbf{v}_4\mathbf{v}_7}{4} + \frac{\mathbf{v}_5\mathbf{v}_6}{4} \\
\beta_{57} =& -\frac{\sqrt{3}\mathbf{v}_1\mathbf{v}_8}{2} - \frac{3\mathbf{v}_4\mathbf{v}_6}{4} + \frac{\mathbf{v}_5\mathbf{v}_7}{4} \\
\beta_{58} =& \frac{\sqrt{3}\mathbf{v}_1\mathbf{v}_7}{4} + \frac{\sqrt{3}\mathbf{v}_2\mathbf{v}_6}{4} + \frac{\sqrt{3}\mathbf{v}_3\mathbf{v}_5}{4} + \frac{3\mathbf{v}_5\mathbf{v}_8}{4} \\
\beta_{67} =& \mathbf{v}_6\mathbf{v}_7 \\
\beta_{68} =& \frac{\sqrt{3}\mathbf{v}_1\mathbf{v}_4}{4} + \frac{\sqrt{3}\mathbf{v}_2\mathbf{v}_5}{4} - \frac{\sqrt{3}\mathbf{v}_3\mathbf{v}_6}{4} + \frac{3\mathbf{v}_6\mathbf{v}_8}{4} \\
\beta_{78} =& \frac{\sqrt{3}\mathbf{v}_1\mathbf{v}_5}{4} - \frac{\sqrt{3}\mathbf{v}_2\mathbf{v}_4}{4} - \frac{\sqrt{3}\mathbf{v}_3\mathbf{v}_7}{4} + \frac{3\mathbf{v}_7\mathbf{v}_8}{4}
\end{aligned}
\tag{B.2}
$$

Note that $\beta_{ij} = \beta_{ji}$, since $D_{\mu\nu}$ is a symmetric matrix.

Appendix C

Results from a non-diagonal model of $D_{\mu\nu}$

In order to check how non-diagonal terms affect the conversion probabilities of mass basis we propose a simplified model with two parameters Γ and β_{38}:

$$D_{\mu\nu} = -\begin{pmatrix} 0 & 0 & 0 & 0 & 0 & 0 & 0 & 0 & 0 \\ 0 & \Gamma & 0 & 0 & 0 & 0 & 0 & 0 & 0 \\ 0 & 0 & \Gamma & 0 & 0 & 0 & 0 & 0 & 0 \\ 0 & 0 & 0 & \Gamma & 0 & 0 & 0 & 0 & -\beta_{38} \\ 0 & 0 & 0 & 0 & \Gamma & 0 & 0 & 0 & 0 \\ 0 & 0 & 0 & 0 & 0 & \Gamma & 0 & 0 & 0 \\ 0 & 0 & 0 & 0 & 0 & 0 & \Gamma & 0 & 0 \\ 0 & 0 & 0 & 0 & 0 & 0 & 0 & \Gamma & 0 \\ 0 & 0 & 0 & -\beta_{38} & 0 & 0 & 0 & 0 & \Gamma \end{pmatrix}. \tag{C.1}$$

The probabilities resulting from such a dissipation matrix are:

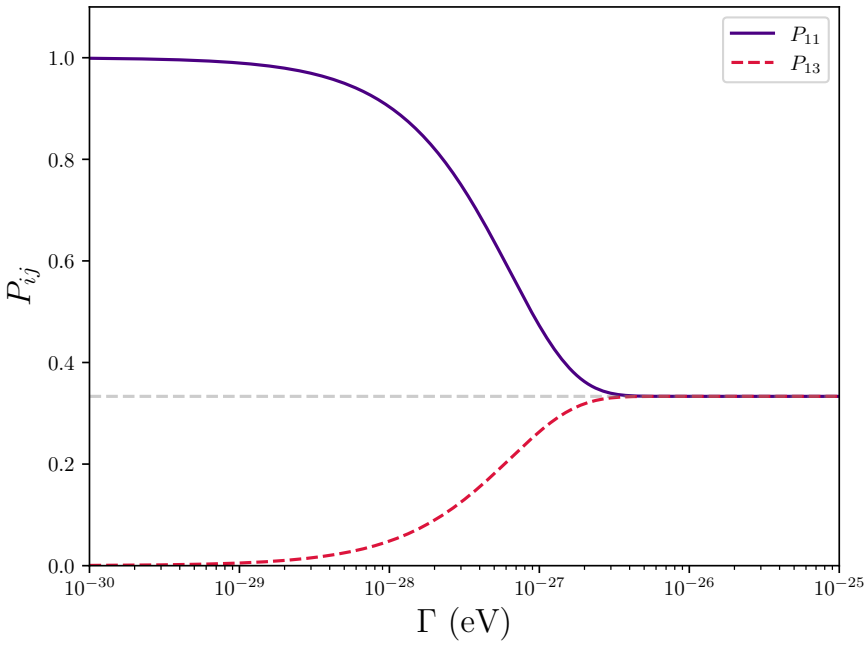

Figure 47 – Probabilities for the mass state basis with the model of $D_{\mu\nu}$ in eq. (C.1). We set $\beta_{38} = 10^{-33}$ eV for a 10 MeV energy and $n = 0$ for the parameters used. Other probabilities in eq.(C.2) have very similar behaviour as shown here.

$$
\begin{aligned}
P_{11} &= \frac{\left(2e^{\Gamma t} + \sqrt{3}e^{\beta_{38}t} + 2e^{\beta_{38}t} - \sqrt{3}e^{-\beta_{38}t} + 2e^{-\beta_{38}t}\right)e^{-\Gamma t}}{6} \\
P_{12} &= \frac{\left(2e^{\Gamma t} - e^{\beta_{38}t} - e^{-\beta_{38}t}\right)e^{-\Gamma t}}{6} \\
P_{13} &= \frac{\left(2e^{\Gamma t} - \sqrt{3}e^{\beta_{38}t} - e^{\beta_{38}t} - e^{-\beta_{38}t} + \sqrt{3}e^{-\beta_{38}t}\right)e^{-\Gamma t}}{6} \\
P_{21} &= \frac{\left(2e^{\Gamma t} - e^{\beta_{38}t} - e^{-\beta_{38}t}\right)e^{-\Gamma t}}{6} \\
P_{22} &= \frac{\left(2e^{\Gamma t} - \sqrt{3}e^{\beta_{38}t} + 2e^{\beta_{38}t} + \sqrt{3}e^{-\beta_{38}t} + 2e^{-\beta_{38}t}\right)e^{-\Gamma t}}{6} \\
P_{23} &= \frac{\left(2e^{\Gamma t} - e^{\beta_{38}t} + \sqrt{3}e^{\beta_{38}t} - \sqrt{3}e^{-\beta_{38}t} - e^{-\beta_{38}t}\right)e^{-\Gamma t}}{6} \\
P_{31} &= \frac{\left(2e^{\Gamma t} - \sqrt{3}e^{\beta_{38}t} - e^{\beta_{38}t} - e^{-\beta_{38}t} + \sqrt{3}e^{-\beta_{38}t}\right)e^{-\Gamma t}}{6} \\
P_{32} &= \frac{\left(2e^{\Gamma t} - e^{\beta_{38}t} + \sqrt{3}e^{\beta_{38}t} - \sqrt{3}e^{-\beta_{38}t} - e^{-\beta_{38}t}\right)e^{-\Gamma t}}{6} \\
P_{33} &= \frac{\left(e^{\Gamma t} + e^{\beta_{38}t} + e^{-\beta_{38}t}\right)e^{-\Gamma t}}{3}
\end{aligned}
\quad . \tag{C.2}
$$

and P_{11} and P_{13} are shown in Figure 47. We see that the behaviour of probabilities in a non-diagonal form of the dissipation matrix is very similar to diagonal versions, with an asymptotic maximal mixing.

Appendix D

Decoherence inside the SN and matter effects

The neutrino Hamiltonian in flavor basis affected by the charged current potential V_W, i.e. $H_f = H_f^{\text{vac}} + V_W$, can be diagonalized to H_m by a unitary transformation provided by U_m as

$$\rho_f = U_m \rho_m U_m^\dagger \qquad H_f = U_m H_m U_m^\dagger, \tag{D.1}$$

getting the most general form of (6.2) in the effective neutrino mass basis in matter

$$\frac{d\rho_m}{dt} = -i[H_m, \rho_m] - [U_m^\dagger \dot{U}_m, \rho_m] + \sum_p^{N^2-1} (V_{pm}\rho_m V_{pm} - \frac{1}{2}\{V_{pm}^2, \rho_m\}) \tag{D.2}$$

or following the notation in (6.9)

$$|\dot{\rho}_m\rangle = -2\mathcal{L}_m(t)\,|\rho_m\rangle \tag{D.3}$$

For all purposes of this work, the propagation is adiabatic, or $\dot{U}_m = 0$ in (D.2).

We are interested in solving equation (D.3) in a variable matter density in order to get transition probabilities $P_{ij}^{m(\text{SN})}$ and $\bar{P}_{ij}^{m(\text{SN})}$. It is straightforward to obtain $|\rho\rangle$ in (6.9) , but in the case of $|\rho_m\rangle$, V_{pm} and H_m are time-dependent and the solution is a time-ordered exponential:

$$\mathcal{T}\left\{e^{-2\int_{t_0}^{t} dt' \mathcal{L}_m(t')}\right\} = 1 + (-2)\int_{t_0}^{t} dt_1 \mathcal{L}_m(t_1) + (-2)^2 \int_{t_0}^{t} dt_1 \int_{t_0}^{t_1} dt_2 \mathcal{L}_m(t_1)\mathcal{L}_m(t_2) + \cdots . \tag{D.4}$$

Analytical solutions for specific cases in a variable matter density can be found in [115, 89]. However, instead of using a cumbersome approximated approach, we analyze the neutrino evolution into the SN making the limits in the integrals in (D.4) $\Delta t = t_n - t_{n-1} \to 0$,

allowing to solve (D.4) numerically through slab approach, i.e. we divided the SN matter density profile into small parts, in which the neutrino Hamiltonian is approximately constant, then we make the time evolution from each step to another until the neutrino reach the vacuum. We use the simulated density profile in Figure 15 to perform this calculation.

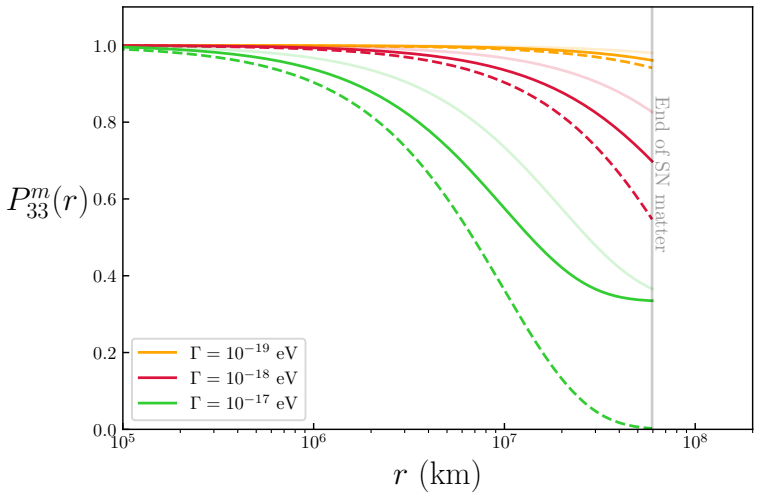

Figure 48 – Solution for a survival probability of ν_3 along a SN radius for the MSC$^\epsilon$ (solid opaque line) and neutrino loss (dashed). The transparent line shows the same probability but in vacuum. More details about these models are in the text. As it will be clear in our results, even with enhancement of the conversion in matter, values of $\Gamma \sim 10^{-19}$ eV are far higher than the sensitivity of a future SN detection compared to coherence length in vacuum used in the MSC$^\epsilon$ model.

In Figure 48 we compare the $P_{33}^{m(\mathrm{SN})}$ to the same probability in mass basis in vacuum, which is shown as an enhancement of the deviation from the standard expectation of $P_{33}^{m(\mathrm{SN})} = 1$. In Figure 27 we show the numerical probabilities of MSC$^\ell$ for the mass state in matter solved as described above.

Appendix E

Quantum decoherence bounds

Table 2 – Constraints for each detector for MSC$^{\not\epsilon}$ scenario with 90% (2σ) C.L. in units of $\Gamma \times 10^{-15}$ (eV). For $n \neq 0$ a representative energy of $E_0 = 10$ MeV was chosen and QD parameters are in eV scale. Values are corresponding to the simulated progenitor of 40 $M_\odot$.

		NH			IH		
Detector	SN distance	$n = 0$	$n = 2$	$n = 5/2$	$n = 0$	$n = 2$	$n = 5/2$
DUNE	1 kpc	0.89(1.1)	0.76(0.89)	0.65(0.87)	0.88(1.0)	2.5(8.8)	3.2(15)
	5 kpc	5.4(7.0)	4.4(5.9)	6.3(8.7)			
	7 kpc	8.3(11)	7.0(9.4)	11(16)			
	10 kpc	14(20)	12(17)	22(35)			
HK	1 kpc	0.96(1.1)	3.7(4.1)	5.0(5.8)	0.93(1.1)	3.9(4.3)	5.3(6.5)
	5 kpc	4.3(5.7)	16(21)	33(47)	4.9(6.6)	18(23)	38(49)
	7 kpc	7.1(11)	27(38)	53(87)	8.5(13)	28(38)	67(99)
	10 kpc	16(51)	65(120)	150(400)	20(36)	52(80)	140(240)
JUNO	1 kpc	4.2(5.4)	15(19)	30(41)	7.2(8.9)	38(51)	100(180)

Table 3 – Same as Table 2 but for MSC$^{\epsilon}$ scenario with $2\sigma(3\sigma)$ C.L. in units of $\Gamma_8 \times 10^{-28}$ (eV). The representative energy of $E_0 = 10$ MeV was taken for $n \neq 0$ and QD parameters are in eV scale. Values are corresponding to the simulated progenitor of 27 $M_{\odot}$.

		NH			IH		
Detector	SN distance	$n = 0$	$n = 2$	$n = 5/2$	$n = 0$	$n = 2$	$n = 5/2$
DUNE	1 kpc	2.1(3.3)	0.43(0.67)	0.24(0.37)	490(700)	50(180)	33(110)
	5 kpc	2.8(5.2)	0.58(1.1)	0.34(0.75)			
	7 kpc	3.2(7.1)	0.71(1.9)	0.46(1.4)			
	10 kpc	4.2(17)	1.1(7.0)	0.80(6.1)			
HK	1 kpc	6.8(11)	0.81(1.1)	0.43(0.58)	9.2(14)	0.68(1.0)	0.36(0.54)
	5 kpc	9.6(23)	0.92(1.9)	0.48(1.0)	10(18)	0.80(1.5)	0.44(0.82)
	7 kpc	13	1.2	0.61(2.6)	11(25)	0.94(2.5)	0.51(1.4)
	10 kpc	42	2.7	1.2	13	1.4	4.9
JUNO	1 kpc	51(100)	6.4(13)	4.0(7.8)	47(89)	5.6(11)	3.5(6.9)

Table 4 – Same as Tables 2 and 3 but for ν-loss scenario, with 3σ bounds over $\gamma \times 10^{-29}$ (eV).

		IH		
Detector	SN distance	$n = 0$	$n = 2$	$n = 5/2$
DUNE	1 kpc	500	4.6	2.1
	5 kpc	100	3.3	1.6
	7 kpc	74	3.2	1.5
	10 kpc	52	3.1	1.5
HK	1 kpc	500	2.6	1.4
	5 kpc	100	2.3	1.2
	7 kpc	70	2.2	1.2
	10 kpc	49	2.1	1.2
JUNO	1 kpc	500	150	110
	5 kpc	100	32	24
	7 kpc	78	24	18
	10 kpc	59	19	14